

Research



Cite this article: Varandas AJC, Rocha CMR. 2018 $C_n(n = 2 - 4)$: current status. *Phil. Trans. R. Soc. A* **376**: 20170145. <http://dx.doi.org/10.1098/rsta.2017.0145>

Accepted: 27 October 2017

One contribution of 14 to a theme issue
'Modern theoretical chemistry'.

Subject Areas:

astrochemistry, interstellar medium,
computational chemistry, physical chemistry

Keywords:

carbon clusters, C_2 , C_3 , C_4 , many-body
expansion, double many-body expansion,
potential energy surfaces

Author for correspondence:

A. J. C. Varandas
e-mail: varandas@uc.pt

Electronic supplementary material is available
online at <https://doi.org/10.6084/m9.figshare.5747079.v1>

$C_n(n = 2 - 4)$: current status

A. J. C. Varandas and C. M. R. Rocha

Department of Chemistry and Coimbra Chemistry Center, University of Coimbra 3004-535 Coimbra, Portugal

ID AJCV, 0000-0003-1501-3317

The major aspects of the C_2 , C_3 and C_4 elemental carbon clusters are surveyed. For C_2 , a brief analysis of its current status is presented. Regarding C_3 , the most recent results obtained in our group are reviewed with emphasis on modelling its potential energy surface which is particularly complicated due to the presence of multiple conical intersections. As for C_4 , the most stable isomeric forms of both triplet and singlet spin states and their possible interconversion pathways are examined afresh by means of accurate *ab initio* calculations. The main strategies for modelling the ground triplet C_4 potential are also discussed. Starting from a truncated cluster expansion and a previously reported DMBE form for C_3 , an approximate four-body term is calibrated from the *ab initio* energies. The final six-dimensional global DMBE form so obtained reproduces all known topographical aspects while providing an accurate description of the C_4 linear-rhombic isomerization pathway. It is therefore commended for both spectroscopic and reaction dynamics studies.

This article is part of the theme issue 'Modern theoretical chemistry'.

1. Introduction and historical remarks

The study of pure carbon chains has fascinated chemists and physicists over the years [1,2]. They were first identified more than a century ago [3] in astrophysical objects but still are a topic of increasing interest. Small C_n clusters play a major role in the chemistry of carbon stars [4,5], comets [3,6] and interstellar molecular clouds [7,8], while acting as building blocks for formation of complex carbon-containing compounds [9,10]. Besides such an astrophysical significance, C_n chains can be chief intermediates in chemical vapour deposition systems for production of carbon-rich thin films [11], and be predominant species in terrestrial sooting flames [1,2]. Their fascinating physicochemical properties find justification on the exceptional bonding flexibility of

carbon as demonstrated by its unique ability to form single, double and triple (even quadruple were suggested for $C_2(X^1\Sigma_g^+)$) bonds.

The richness of the carbon chemistry is clearly evinced by the structural diversity of carbon allotropes, which include [20] diamond, graphite, fullerenes [21], nanotubes [22], graphenes [23] and other elusive periodic scaffolds [24], all with outstanding electronic, material or biological properties. Elucidation of possible mechanisms for formation of such aggregates (i.e. their evolution from linear to monocyclic/polycyclic rings to fullerene/cage-like structures) is only attainable once the properties of their precursors (smallest clusters) have been clarified [25–29].

Small C_n clusters are highly reactive species which makes their experimental characterization cumbersome [1,2]. On the other hand, the existence of several (nearly isoenergetic) isomers, a high density of low-lying singlet/triplet electronic states and a significant multi-reference (MR) character, makes their study theoretically challenging [30–39]; see glossary at the end of the paper. Clearly, a detailed knowledge of the structure and energetics of such species requires a faithful interplay between state-of-the-art experimental techniques and high-level *ab initio* calculations.

Most of our knowledge on the title molecules began with the seminal work of Pitzer & Clementi [40]. They first recognized that linear C_n molecules are low-energy isomeric forms with odd- and even-numbered chains (for $n > 2$) attaining $^1\Sigma_g^+$ and $^3\Sigma_g^-$ ground electronic states, respectively. Typically, for such systems, cumulenic structures ($C=C-C=C$) are lower in energy than acetylenic ($C\equiv C-C\cdots C-C$) bonding configurations [1,2,40,41]. More recently, supported by *ab initio* calculations, low-lying monocyclic isomers have also been conjectured as being isoenergetic or even more stable than linear arrangements [25–29,39]. In this work, we survey the current status on the smallest clusters (C_2 , C_3 and C_4) but keep the focal point on the trimer and tetramer. For C_3 , we review our recent work in §3, while in §4a high-level *ab initio* calculations are reported anew for C_4 . A global 6D potential energy surface (PES) of ground-state triplet C_4 is also provided for the first time in §4b.

(a) The carbon dimer: the best studied carbon cluster

The most abundant molecules in carbon vapour produced by laser vapourization of graphite are C_2 and C_3 [42–44], with the former being widely quoted as important stacking subunits during formation (growth) of medium-sized to large fullerenes [45]. Their spectroscopy has been extensively studied over the years, making them by far the best characterized carbon clusters [1,2].

As first observed by Wollaston [46] and Swan [47], C_2 is responsible for the blue glow emanating from hydrocarbon flames. These well-known $d^3\Pi_g-a^3\Pi_u$ Swan bands (the spectroscopic notation employed throughout is the updated one [48]) at 19380.1 cm^{-1} have long been recognized in cometary spectra [49]. Despite previous knowledge of the Phillips ($A^1\Pi_u-X^1\Sigma_g^+$) and Mulliken ($D^1\Sigma_u^+-X^1\Sigma_g^+$) bands involving singlet states [50], the prominence of the Swan emission/absorption features in the laboratory and astrophysical sources led to consider $a^3\Pi_u$ as the ground state of C_2 . This changed with Ballik & Ramsay [50] during investigations of the $b^3\Sigma_g^--a^3\Pi_u$ system (so-called Ballik–Ramsay band). They observed perturbations in the rotational levels of the $^3\Sigma_g^-$ state which were attributed to the presence of a neighbouring singlet state. From the analysis of the spectral lines, the authors first confirmed that $^1\Sigma_g^+$ is the ground state of the carbon dimer. In fact, it lies only 603.8 cm^{-1} below the $a^3\Pi_u$ state [48]. Later on, several other singlet, triplet, quintet and intercombination band systems of the carbon dimer have been reported in the literature [1,2,48,51]. At present, C_2 has a total of 23 identified band systems, covering the spectral range $0\text{--}55000\text{ cm}^{-1}$, and 21 spectroscopically characterized electronic states; see [1,2,48,51] for a review. Guided by this well-known and rich rovibronic line list, the identification C_2 was made possible in a plethora of astrophysical sources, including carbon stars, comets, interstellar medium and the sun [1,2,48]. Such a wealth of spectroscopic information has been recently used [48] to obtain highly accurate partition functions and thermodynamic data of C_2 up to 4000 K.

The first theoretical work on carbon dimer dates back to 1939 by Mulliken [52]. Using known experimental information on C_2 , molecular orbital arguments and an empirical formula for estimating internuclear distances (R_0), he predicted mean relative energies and R_0 values for various low-lying states. Besides assigning the observed band system at 43239.8 cm^{-1} due to $^1\Sigma_u^{+}-^1\Sigma_g^{+}$ transition (now known under his name), Mulliken commented on the possibility that $^1\Sigma_g^{+}$ could be the ‘normal state’ of the carbon dimer. Apart from the pioneering semi-empirical work of Araki & Watari [53], the first VB calculations on C_2 were performed by Clementi & Pitzer [54]. The authors expanded the wave functions of the six lowest states arising from $2\sigma_g^2 2\sigma_u^2 1\pi_u^4$ ($^1\Sigma_g^{+}$), $2\sigma_g^2 2\sigma_u^2 1\pi_u^3 3\sigma_g^1$ ($^3\Pi_u$, $^1\Pi_u$) and $2\sigma_g^2 2\sigma_u^2 1\pi_u^2 3\sigma_g^2$ ($^3\Sigma_g^{-}$, $^1\Delta_g$, $^1\Sigma_g^{+}$) valence configurations in terms of covalent, ionic and double-ionic components whose contributions have been variationally determined. Although the results agreed reasonably with the experimental data at that time (the $^3\Pi_u$ curve turned out to be lowest in energy), the authors recognized the need of a more refined theory to fully understand the inherent complexities of the system. Read and Vanderslice were the first to report PECs of C_2 using the RKR method [55]. Based on the findings of Ballik & Ramsay [50] concerning the true ground state of the system, the authors also tentatively calculated dissociation energies for the nine upper-lying electronic states [55]. To our knowledge, the first purely *ab initio* calculations performed on the dimer are due to Fraga & Ransil [56], Fougere & Nesbet [57] and Kirby & Liu [58] using CI wave functions with Slater-type orbitals. In the most complete work in these series, Kirby and Liu reported PECs for 62 valence states of C_2 , including 28 singlets, 28 triplets and 6 quintets that correlate with carbon atoms in their 3P , 1D and 1S states [58], respectively. Such calculations rendered the identification of 19 possible bound states not yet observed experimentally at that time together with the determination of their spectroscopic constants. In turn, Watts & Bartlett [59] performed CCSD(T) calculations with several Dunning’s correlation-consistent basis sets [60,61]. The discrepancies found in the prediction of the $^1\Sigma_g^{+}/^3\Pi_u$ energy splittings have been attributed to the strong MR character of the ground state. Such an aspect has previously been emphasized by Bauschlicher & Langhoff [62] by means of CASSCF and MRCI calculations.

Since then, C_2 has been the subject of extensive *ab initio* MRCI [30–32,63–71], full CI [72,73], quantum Monte Carlo [74] and explicitly correlated MR [75] calculations aiming at obtaining accurate analytic representations of the various PECs (and their avoided crossings [30–32]), electronic excitation energies, dissociation energies and expectroscopic parameters. Note that these latter approaches frequently rely on extrapolations to the one- and/or N -electron basis sets, core and core–valence correlation contributions, and also relativistic corrections. As argued several times [72–75], the presence of various low-lying excited electronic states and its unusual bonding behaviour makes C_2 a notoriously challenging benchmark test for quantum chemical methods. Recently, with the aid of high-level MR calculations and state-of-the-art experimental techniques, Krechkivska *et al.* reported the existence of novel $4^3\Pi_g-a^3\Pi_u$ [69] and $3^3\Pi_g-a^3\Pi_u$ [71] systems (referred to as Krechkivska–Schmidt bands) and provided an accurate value for the carbon dimer ionization energy [70].

$C_2(X^1\Sigma_g^{+})$ is one of the most strongly bonded diatomic molecule in nature [14,18,19]. Besides being the simplest possible carbon cluster, its bonding has eluded chemists over the years and continues to render extensive debate [12–19]. The simple assumption of a $2\sigma_g^2 2\sigma_u^2 1\pi_u^4$ valence configuration and molecular orbital arguments would suggest a bond order of two [52] ($\text{C}=\text{C}$), while qualitative VB considerations (e.g. assuming two *sp*-hybridized carbons) yield a triply bonded species, $\text{C}\equiv\text{C}$ [12]. Recently, using high-level VB calculations, Shaik and co-workers [13,14,18,19] proposed the existence of a fourth σ -bond on ground-state C_2 (first contemplated by Mulliken [52] and Schleyer *et al.* [76] for excited states). It arises from the interactions between the ‘residual’ singlet odd pair, pointing outwards on the *sp* hybrids, i.e. $\overline{\text{C}}\equiv\overline{\text{C}}$. This additional ‘inverted’ bond would contribute $\approx 70\text{--}90\text{ kJ mol}^{-1}$ to the overall interaction. This has been disputed [15–18], with no consensus yet reached about the C_2 bonding nature.

(b) The carbon trimer

The smallest cluster capable of forming cyclic structures is C_3 . Its well-known $\tilde{A}^1\Pi_u - \tilde{X}^1\Sigma_g^+$ emission spectrum was first recorded by Huggins in 1881, while investigating unknown cometary emission features near 24675.6 cm^{-1} [3]. These so-called Swings emission bands [1] were first reproduced in the laboratory by Herzberg [77]. Although the emitter was initially thought to be CH_2 [77], the unambiguous assignment to linear C_3 is due to Douglas [78] and Gausset *et al.* [79,80], who performed spectroscopic investigations on discharges through ^{13}C -substituted methane and flash photolysis of diazomethane, respectively. From the high-resolution spectra, Gausset *et al.* first emphasized the unusual low bending frequency of $l\text{-}C_3(\tilde{X}^1\Sigma_g^+)$ with $\nu_2 \approx 63\text{ cm}^{-1}$ as well as the strong RT vibronic interactions of the excited $l\text{-}C_3(\tilde{A}^1\Pi_u)$. Such features are responsible for the observed intricate vibrational spectrum [79,80]. Several gas-phase and matrix studies of C_3 have subsequently been devoted to its spectroscopic characterization, resulting in the assignment of the most ground and upper state vibrational frequencies of the $\tilde{A}^1\Pi_u - \tilde{X}^1\Sigma_g^+$ band [81–85] and the discovery of a low-lying triplet electronic state manifold [86–88]. In fact, the carbon trimer is perhaps one of the best characterized non-rigid triatomics in existence [2,89].

C_3 has been observed in a wide range of astrophysical sources [90,91], including circumstellar shells of carbon stars [4,92,93], interstellar molecular clouds [7,94–96] and comets [3,92]. Its mid-IR spectrum (ν_3 antisymmetric stretching mode) was measured in the circumstellar envelope of the C-rich star IRC+10216 by Hinkle *et al.* [4], and the far-IR one (ν_2) detected in the direction of Sgr B2 by Cernicharo *et al.* [92]. The abundance of C_3 were determined in translucent clouds by Maier *et al.* [95], Roueff *et al.* [96] and Oka *et al.* [90] through its Swings' electronic transition. As the most abundant small pure carbon molecule in the interstellar medium, C_3 along with C_2 are key to the formation of more complex carbon clusters, long-chain cyanopolyyynes, carbon dust and polycyclic aromatic hydrocarbons [1,2]. In addition to its astrophysical importance, it is the predominant carbon cluster in equilibrium hot carbon vapour [2,42,44], hydrocarbon flames [1,2] and plasmas generated through energetic processing of carbon-containing materials [2,97,98].

The relevance of C_3 in space as well as in terrestrial sooting flames and combustion processes has motivated many theoretical [34–36,40,99–117] studies both in the ground and low-lying excited singlet and triplet electronic manifolds [33,114,118]. In particular, much effort has been devoted to obtain local (near-equilibrium) ground-state PESs [119] with a view to explore its quasi-linearity and unusual large-amplitude bending motions.

Early *ab initio* SCF studies due to Clementi and co-workers [40,99,100] agree on an electronic structure of the form $C=C=C$ with C_3 assumed linear. Hoffmann [101] reported extended Hückel calculations and predicted it to be nonlinear with an equilibrium CCC bond angle of $\approx 160^\circ$ and a barrier to linearity of only $\approx 63\text{ cm}^{-1}$. Motivated by the discrepancies found in the calculated and experimental entropy values of C_3 as well as the proposition by Gausset and co-workers that the molecule could be quasi-linear, Liskow *et al.* [102] have subsequently performed SCF and CI studies. They highlighted for the first time the unusual bending potential of C_3 as well as the importance of adding d functions to the basis set. In turn, Perić-Radić and co-workers [103] used MRCI calculations and a double- ζ -plus-polarization basis set to report curves for the symmetric, bending and antisymmetric stretching of the ground and first excited ${}^1,{}^3\Pi_u$ trimeric states. The strong RT vibronic interactions to which the Π_u states are subjected was pointed out for the first time [103]. To the best of our knowledge, the first global PES for the ground state of $C_3(1^1A')$ has been reported by Carter *et al.* [105]. The authors employed the MBE [105,119,120] formalism jointly with the experimentally determined force field of Gausset *et al.* and 40 *ab initio* energies [102,104] to obtain an analytic form that exactly reproduces an early experimental heat of formation, geometry and force constants of $l\text{-}C_3(\tilde{X}^1\Sigma_g^+)$. Additionally, other relevant topographical attributes such as the C_{2v} transition states for isomerization between the three equivalent symmetry-related minima are described, as well as an accurate characterization of the adiabatic atom+diatom asymptotic limits, $C_2(a^3\Pi_u) + C(^3P)$ [105–107,119].

Following a previous observation due to Liskow *et al.* that ground-state $l\text{-}C_3$ correlates with an ${}^1E'$ term at equilateral triangular geometries, Whiteside *et al.* [121] used

MP4SDQ/6-31G*//HF/6-31G* to understand the JT nature of the PES. They noted for the first time that both C_{2v} transition state and linear minimum arise from JT distortions of the D_{3h} structure; the corresponding isomerization barrier was predicted to be about 125.1 kJ mol^{-1} . Additionally, they have pointed out that a triplet $^3A'_2$ term arises from the e'^2 valence configuration, with its minimum occurring at equilateral triangular geometries.

Kraemer *et al.* [108] using CISD(Q) and a triple- ζ -plus-polarization basis set reported a local PES which has been expressed as a force field expansion. Its minimum shows the C_3 radical as a bent species with an equilibrium bond angle of approximately 162° and a barrier to linearity of 21 cm^{-1} . The results suggested C_3 to be *quasi-linear*. Such a finding was reinforced by Jensen [109], who used the MORBID Hamiltonian [122] along with experimentally determined bend-stretch term values to obtain an analytic PES for the ground electronic state of C_3 [109]. These earlier PESs were soon superseded by *ab initio* ones from CASSCF calculations [110,111] which suggested C_3 to be non-*quasi-linear* but possessing an exceptionally flat bending potential.

Mladenović *et al.* [113] published an extensive theoretical study of C_3 based on SR CCSD(T) calculations and a basis set of near AVQZ quality. An analytical local PES has also been calibrated from a total of 108 *ab initio* energies up to about 3000 cm^{-1} above the equilibrium geometry by least-squares fitting a Taylor-series-type expansion. With an RMSD of around 2 cm^{-1} , such a form reproduces the rovibrational spectrum of C_3 within 8 cm^{-1} up to the specified energy range.

Ahmed *et al.* [34] and Saha & Western [114] employed MRCI(Q) calculations with the VTZ basis set to model local near-equilibrium PESs for both the ground and excited $\tilde{A}^1\Pi_u$ and $\tilde{D}^1\Delta_g$ electronic states of the C_3 trimer, with the fitted parameters subsequently altered to mimic the experimental data. From these studies, important features were highlighted such as strong RT vibronic interactions for the Π and Δ excited states as well as the presence of a symmetry-required Ci between the ground and first excited singlet states of C_3 at D_{3h} geometries. Suffice to add that a total of 384 *ab initio* energies up to 8000 cm^{-1} above the equilibrium geometry has been employed to fit the ABW Taylor-series expansion for the ground state, which shows an RMSD of 13.2 cm^{-1} . As noted by the authors, their fit covers a range of $\approx 8713\text{ cm}^{-1}$ above the ZPE and mimics 100 rovibrational levels within 3 cm^{-1} . Note that the purely *ab initio* PES shows an RMSD of about 61.6 cm^{-1} for the same levels.

Schröder & Sebald [115] reported a local PES for C_3 employing a quantum mechanical composite approach. Their form was obtained from fc-CCSD(T*)-F12b/AV5Z calculations, with the raw *ab initio* energies corrected additively such as to approximate higher-order correlations, core–core/core–valence effects and also scalar relativistic contributions. All calculated points were then fitted by a polynomial form with a standard deviation of 0.05 cm^{-1} [115]. From it, low-lying rotation–vibration energies for $J \leq 30$ and a few vibrational term energies up to $\approx 3500\text{ cm}^{-1}$ above the ZPE have been reported, and shown to agree within 1 cm^{-1} with the observed values.

In [35], we have reported the first purely *ab initio*-based global PES for $C_3(1^1A')$ (known as DMBE I). A total of 629 *ab initio* energies at the MRCI/AVTZ level of theory have been employed to calibrate a DMBE [123–125] form. To account for the incompleteness of the basis set and truncation of the MRCI expansion, all calculated external correlation energies have been scaled prior to calibration via the DMBE-SEC method [126], and fitted with an RMSD of 4.1 kJ mol^{-1} [35]. In this study, we outlined for the first time the existence of three symmetry-equivalent C_{2v} crossing seams in close proximity to the symmetry-required D_{3h} Ci. Because a third electronic state of $1^1A'$ symmetry ($1^1A'_1$ in D_{3h}) comes quite close in energy to the pair of intersecting states ($1^1E'$ in D_{3h}) near D_{3h} arrangements [36], such unusual topographical attributes have been ascribed to combined JT+PJT vibronic effects $[(E' + A'_1) \otimes e']$ with the proper cusped behaviour modelled accordingly [127,128]. Exploratory rovibrational energy calculations have also been performed, and the DMBE I form shown to reproduce the vibrational energy spectrum of C_3 with an RMSD of 50.4 cm^{-1} for 53 calculated levels up to about 3000 cm^{-1} above the ZPE [35]. The combined JT+PJT problem in C_3 has been further exploited by us [36] with intriguing results. We will come to it later on §3, where other recent results from our group are also discussed for C_3 .

(c) The carbon tetramer

The existence of two low-lying isomeric structures of C₄ is widely accepted: the cumulenic linear chain [*l*-C₄(³Σ_g⁻)] and the bicyclic rhombic [*r*-C₄(¹A_g)] structures [37,38,129–141]. Along with C₂ and C₃, the title species is probably an important molecule in astrophysics and an abundant one in carbon-rich stars as well as interstellar molecular clouds [8,9]. Cernicharo *et al.* [8] reported a pattern of bands at 173.9 cm⁻¹ observed in Sgr B2, IRC+10216, CRL 618, CRL 2688 and NGC 7027 which was tentatively assigned to the ν_5 *cis*-bending mode of *l*-C₄(³Σ_g⁻). Motivated by the observation of C₃ in interstellar clouds [95], Maier *et al.* [142] were the first to attempt the detection of *l*-C₄(³Σ_g⁻) in the ζ Ophiuchi star by measuring the origin bands of its well-known electronic transitions ³Σ_u⁻–³Σ_g⁻ at 26384.9 cm⁻¹ [143]. Unfortunately, as stated by the authors [142], such a detection has not been pursued. Triplet C₄ has been first observed experimentally by Weltner *et al.* [144] and Graham *et al.* [145] using IR and electron spin resonance spectroscopy of graphite vapour trapped in inert-gas matrices. Heath & Saykally [146] first characterized such a species in gas phase through its antisymmetric CC stretching fundamental (ν_3) at 1548.9 cm⁻¹ by means of tunable IR diode laser spectroscopy. Subsequently, Moazzen-Ahmadi *et al.* [147] revisited the rotational constant for the ν_3 mode. From this parameter and the associated averaged C=C bond length ($\approx 2.458a_0$) [147], triplet C₄ was confirmed to be linear with a cumulenic structure [2,147]. A wealth of other experimental efforts have been done to characterize the title species [2,8,140,148,149]. As noted by Senent *et al.* [140], relatively large errors affect other modes besides the ν_3 fundamental, which makes a definitive assignment of *l*-C₄ in interstellar bands a rather difficult task. Apart from the linear isomer, experimental evidence for *r*-C₄(¹A_g) was reported with the Coulomb explosion imaging technique [150–152]. Kella *et al.* [152] observed three distinct photodetachment wavelengths, and conjectured the existence of a third 3D isomer which has been attributed to a tetrahedral structure. However, this has not been supported by any other experimental or theoretical evidence [38,140]. More recently, Blanksby *et al.* [138] performed mass spectrometric studies on isotopically labelled C₄⁻. Upon neutralization of the incident anions and based on the peak abundances of the spectra so obtained, they reported evidence of isotopic scrambling of both singlet (¹Σ_g⁺) and triplet (³Σ_g⁻) neutral *l*-C₄ due to formation of the corresponding rhombic isomers [138].

C₄ has also been the subject of many theoretical studies [37,38,40,41,129–141], starting with the pioneering *ab initio* SCF calculations of Clementi [41]. To our knowledge and apart from semi-empirical MINDO/2 studies of Slanina & Zahradník [153], the first correlated *ab initio* calculations of the relative energies of *l*-C₄(³Σ_g⁻) and *r*-C₄(¹A_g) are due to Whiteside *et al.* [129] at the MP4SDQ/6-31G*//HF/6-31G* level of theory. They have predicted the singlet rhombic structure to be 2.9 kJ mol⁻¹ more stable than the linear chain, and hence the ground state of C₄. The same authors further highlighted the existence of a C_{2v} planar isomeric form (a capped triangle) on the singlet PES which was found to lie approximately 123.4 kJ mol⁻¹ above the *r*-C₄(¹A_g) [129]. Subsequent *ab initio* studies by Magers *et al.* [130], Bernholdt *et al.* [133], Martin *et al.* [136] and Watts *et al.* [137] employing the CC method, as well as CI calculations by Ritchie *et al.* [131] and Pacchioni & Koutecký [132], have indicated the two isomers to be essentially isoenergetic, with the linear-rhombic energy difference being extremely sensitive to the basis set and correlation treatment [136,137]. In turn, Parasuk & Almöf [37] performed MRCI calculations using CAS wave functions as reference and ANO-type basis sets. At the highest level of theory, i.e. 16-electron MRCI in a (13s8p4d)/[5s4p2d] ANO basis, with five dominant configurations in the CAS(10,10) wave function being included in the reference set [37], *l*-C₄(³Σ_g⁻) was predicted to be the ground-state structure with a stabilization energy of approximately 6.8 kJ mol⁻¹ with respect to the ¹A_g state. Motivated by earlier experimental results of Cheung & Graham [154] who conjectured the existence of triplet C₄ as a bent structure, Parasuk & Almöf [37] investigated the PES of *l*-C₄(³Σ_g⁻) along the *cis* (ν_5)- and *trans* (ν_4)-bending modes whose frequencies have been estimated to be 211.0 and 428.0 cm⁻¹ in the same order. In contrast to the floppy nature of C₃ [35,116,117], the authors were the first to point out the stiffness of the bending potential of C₄, thence refuting any evidence for a bent structure in the gas phase [37]. In an attempt

to assign some of the unknown transitions in the IR spectrum of carbon clusters trapped in Ar matrices [144], Martin *et al.* [135,136,155] suggested that the observed band at 1284 cm^{-1} was due to the ν_6 mode of $r\text{-C}_4(^1A_g)$. Subsequently, the authors [155] computed a QFF for such a species using 116 CCSD(T) energies with a VTZ basis [60,61]. Their best ν_6 estimate (including the strong Fermi resonance with the $\nu_3 + \nu_5$ combination band) was $1320 \pm 10\text{ cm}^{-1}$, thence casting doubts on Martin's earlier statement [135,136,155]. As noted by the authors themselves [155], the correct assignment would then imply an unusual large matrix red shift in argon. Recently, Massó *et al.* [38] performed MRCI(Q)/VTZ calculations on C_4 keeping all configurations with coefficients larger than 0.03 in the CAS(8,12) wave function as the reference set. The results so obtained have shown $l\text{-C}_4(^3\Sigma_g^-)$ to be favoured by about 100.7 kJ mol^{-1} over $r\text{-C}_4(^1A_g)$, thus supporting the general trend that the linear triplet structure is the most stable form in MRCI calculations [37,38,132]. Besides various structural parameters of both singlet and triplet PESs, the authors evaluated isomerization pathways between such forms and reported other low-lying excited singlet, triplet and quintet electronic states [38]. To determine new spectroscopic parameters for C_4 and attempt a definitive assignment of the astrophysical band observed by Cernicharo *et al.* [8], Senent *et al.* [140] reported local PESs for both $l\text{-C}_4(^3\Sigma_g^-)$ and $r\text{-C}_4(^1A_g)$ isomers using about 1050 non-redundant energies calculated at the MRCI(Q)/VTZ level [38]. The *ab initio* data so obtained have then been least squares fitted to a Taylor series expansion with an RMSD of 43 cm^{-1} , with spectroscopic parameters determined by standard vibrational perturbation theory (VPT2) [140]. Most recently, Wang *et al.* [141] reported a new QFF PES for $r\text{-C}_4(^1A_g)$ by fitting 255 CCSD(T)/CV5Z energies. A local PES covering a wider range of geometries has also been obtained using 2914 grid points at the CCSD(T)-F12b/AVTZ level of theory, and updated sets of spectroscopic parameters reported for the rhombic isomer using VPT2 and vibrational configuration interaction calculations [141].

Despite the immense theoretical work done on C_4 [37,38,40,41,129–141,143], it is clear from such studies that only some very limited portions of the PES are well understood, namely regions close to the $l\text{-C}_4(^3\Sigma_g^-)$ and $r\text{-C}_4(^1A_g)$ minima. While knowledge of structural and spectroscopic parameters as well as the energetics are key for the identification of C_4 (especially $r\text{-C}_4(^1A_g)$) in experimental analysis and astrophysical sources, many other important issues remain to be assessed. Of particular relevance is the determination of other stable (or even transient) isomeric forms and their interconversion pathways, which provide valuable information for understanding reactive collision processes and formation of C_n clusters in the interstellar medium [9]. In view of the above, we report new results on C_4 in §4. By exploring the isomerization pathway between linear and rhombic structures on both singlet and triplet PESs, other isomers are unravelled, some reported for the first time. Based on such results and the DMBE, an approximate four-body term is calibrated using accurate *ab initio* data, and hence also a global 6D form for triplet C_4 .

2. Further on carbon trimer

(a) Electronic structure

Figure 1 shows the optimized bending potential for ground- and low-lying excited singlet states of C_3 at the MRCI/AVTZ//CASSCF/AVTZ level of theory [35]. Note that, for acute $\angle\text{CCC}$ angles (less than 30°), the optimization process leads naturally to the asymptotic channels, as the optimum bond length corresponds to widely separated atom+diatom fragments. As first pointed out by Murrell and co-workers [105–107,119], the ground state of C_3 does not dissociate adiabatically to ground-state fragments [$\text{C}_2(\text{X}^1\Sigma_g^+) + \text{C}(^3P)$], inasmuch as either C_2 or C must be on an excited state to satisfy the spin–spatial Wigner–Witmer correlation rules [156,157] (see §3d). As figure 1 shows, all degenerate excited states at linear geometries ($\tilde{A}^1\Pi_u$, $\tilde{B}^1\Delta_u$, $\tilde{C}^1\Pi_g$, $\tilde{D}^1\Delta_g$, etc.) are subjected to strong RT vibronic interactions which are manifested as splittings into symmetric (A') and antisymmetric (A'') components as the molecule bends. Such electronic excited states show also numerous crossings between themselves for bending angles smaller

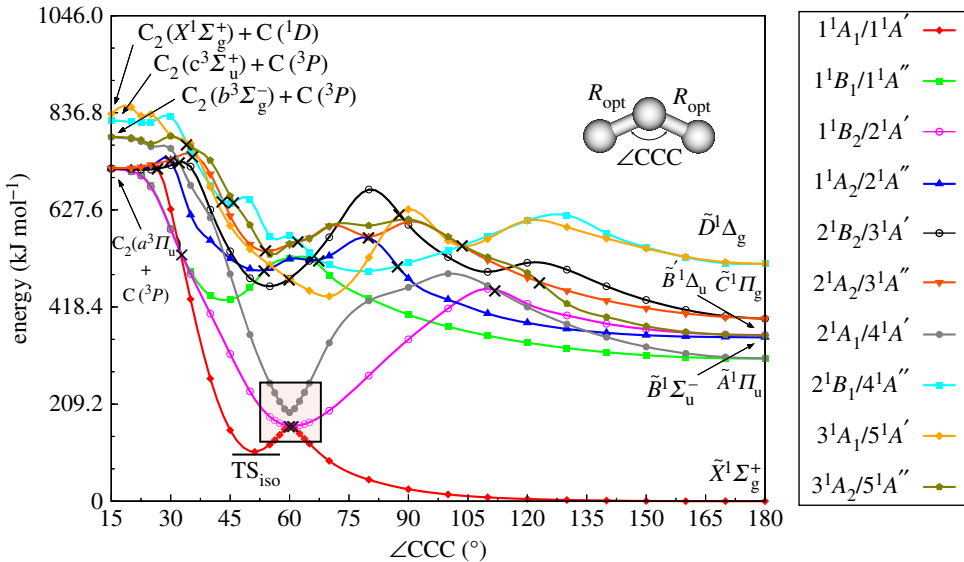


Figure 1. Optimized bending potentials for C_3 at the MRCI/AVTZ//FVCAS/AVTZ level of theory as a function of the $\angle CCC$ angle. Shown in the key are the irreducible representations in C_{2v} symmetry for each state, and correlations within the C_3 point group. Also shown are the associated correlations for linear geometries in $D_{\infty h}$ symmetry, and corresponding dissociation limits. Cis are indicated by the cross symbol. Energies are given with respect to the global minimum of C_3 of $D_{\infty h}$ symmetry. (Online version in colour.)

than 140° . These are indicated by the symbol ‘ \times ’ in figure 1. However, an appreciable gap (up to 377 kJ mol^{-1}) is visible between the excited and ground states for $\angle CCC \geq 100^\circ$. Note that the $\tilde{B}^1\Sigma_u^-$ and $\tilde{B}'^1\Delta_u$ states are close in energy, with the former predicted from our *ab initio* calculations to be $\approx 1.2 \text{ kJ mol}^{-1}$ more stable than the latter. As indicated by Ahmed *et al.* [34] and Saha & Western [114], such energetic proximity (near degeneracy) is expected to be of the same order of magnitude as the accuracy of the *ab initio* calculations themselves, and therefore a proper examination of their relative stability requires a higher level of theory. Recall [34,79,80,114] that the ground-state bending potential is exceptionally flat, and hence large-amplitude bending vibrations are expected: only 25.8 kJ mol^{-1} are required to bend C_3 up to $\angle CCC = 90^\circ$.

A region that deserves attention refers to near equilateral triangular geometries ($\angle CCC = 60^\circ$). As we have first noted [35,36], the C_3 PES shows there intriguing topographical attributes (highlighted in figure 1 by the shaded square): rather than a single symmetry-dictated C_i , a strong mixing of two 1A_1 states occurs which pushes down the lowest to cross twice the 1B_2 state. As similar cross sections of figure 1 exist for rotations by $\pm 120^\circ$, such a combined JT+PJT $[(E' + A'_1) \otimes e']$ effect creates four Cis in the ground-state PES (see §3b). Note that distortions of the D_{3h} structure maintaining C_{2v} symmetry with bend angles less than 60° lead to stabilization of the lower sheet and formation of a saddle point (figure 1). This represents the transition state (TS_{iso}) for isomerization between the three equivalent $D_{\infty h}$ minima in the ground-state PES. Conversely, C_{2v} distortions with angles greater than 60° lead ultimately to the absolute $D_{\infty h}$ minima of C_3 .

(b) The Jahn–Teller plus pseudo-Jahn–Teller problem

As shown in figure 1 and noted elsewhere [34–36,121], both the ground [$1^1A'(1^1A_1)$] and first excited [$2^1A'(1^1B_2)$] singlet states of C_3 correlate with the twofold E' irrep at D_{3h} geometries, thus yielding an e'^2 valence configuration (figure 2). At such geometries, four electronic states arise from HOMO \rightarrow HOMO excitations

$$e' \otimes e' \xrightarrow{D_{3h}} A'_1 + A'_2 + (E') \xrightarrow{C_{2v}} A_1 + B_2 + (A_1 + B_2). \quad (2.1)$$

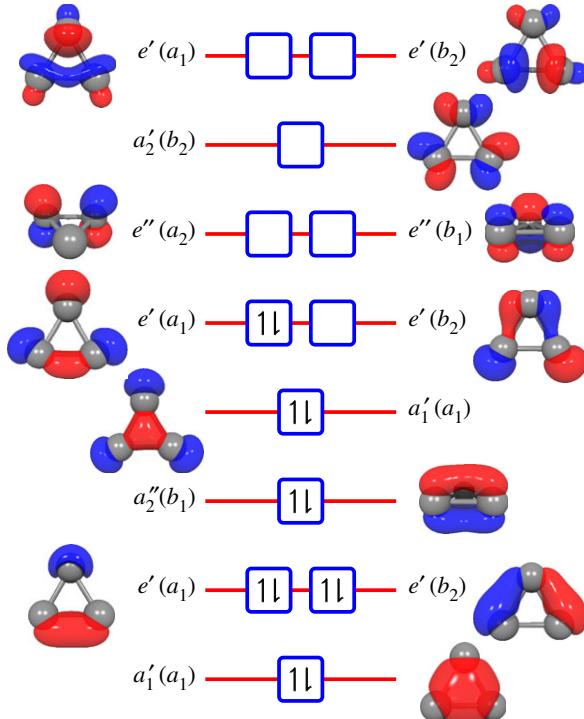


Figure 2. MO diagram and valence electronic configuration of C_3 at equilateral triangular geometries. The 1A_1 (in C_{2v}) component of the $^1E'$ term (in D_{3h}) is schematically shown. MOs are labelled according to D_{3h} irreps with the corresponding correlations with C_{2v} point group in parentheses. Up and down arrows denote as usual α and β spin states. Natural orbitals obtained from a state-averaged FVCAS/AVTZ wave function are also shown. (Online version in colour.)

All of them correlate with the A' irrep in C_s symmetry. Similarly, higher excited states can be obtained from the HOMO – 1 → HOMO, HOMO → LUMO, and HOMO – 2 → HOMO excitations, but they are not considered here. At FVCAS/AVTZ, the leading (spin–spatial symmetry adapted) CSFs for each electronic term of equation (2.1) are then given by [36]

$$|\Psi_1\ ^3A'_2(1^3B_2)\rangle = |\alpha\rangle \quad (2.2)$$

$$|\Psi_2\ ^1E'(1^1A_1)\rangle = \frac{1}{\sqrt{\mathcal{A}^2 + \mathcal{B}^2}} [\mathcal{A} |\beta\rangle - \mathcal{B} |\gamma\rangle] \quad (2.3)$$

$$|\Psi_3\ ^1E'(1^1B_2)\rangle = \frac{1}{\sqrt{\mathcal{C}^2 + \mathcal{D}^2}} [\mathcal{C} |\delta\rangle - \mathcal{D} |\epsilon\rangle] \quad (2.4)$$

and

$$|\Psi_4\ ^1A'_1(2^1A_1)\rangle = \frac{1}{\sqrt{\mathcal{E}^2 + \mathcal{F}^2}} [\mathcal{E} |\beta\rangle + \mathcal{F} |\gamma\rangle], \quad (2.5)$$

where $|\alpha\rangle$, $|\beta\rangle$, $|\gamma\rangle$, $|\delta\rangle$ and $|\epsilon\rangle$ are Slater determinants schematically shown in figure 3: \mathcal{A} , \mathcal{B} , \mathcal{C} , \mathcal{D} , \mathcal{E} and \mathcal{F} are coefficients that weight the relative contributions in the associated CSF. At D_{3h} geometries, their ratios are approximately equal to one, with $|\mathcal{A}| = |\mathcal{B}| \approx |\mathcal{C}| = |\mathcal{D}| \approx |\mathcal{E}| = |\mathcal{F}| \approx 1$. However, if any distortion of the molecular triangle occurs, the ratio of each determinant changes inasmuch as different CSFs belonging to the same spin and spatial symmetry can mix.

As seen from equations (2.2)–(2.5) and figure 4, an $^3A'_2(1^3B_2)$ term lower than the $^1E'(1^1A_1, 1^1B_2)$ and $^1A'_1(2^1A_1)$ states also arises from the HOMO → HOMO excitations. Such a triplet state shows the minimum at a geometry with D_{3h} symmetry (*c*- $C_3(^3A'_2)$; table 1) and hence is non-JT [36,121].

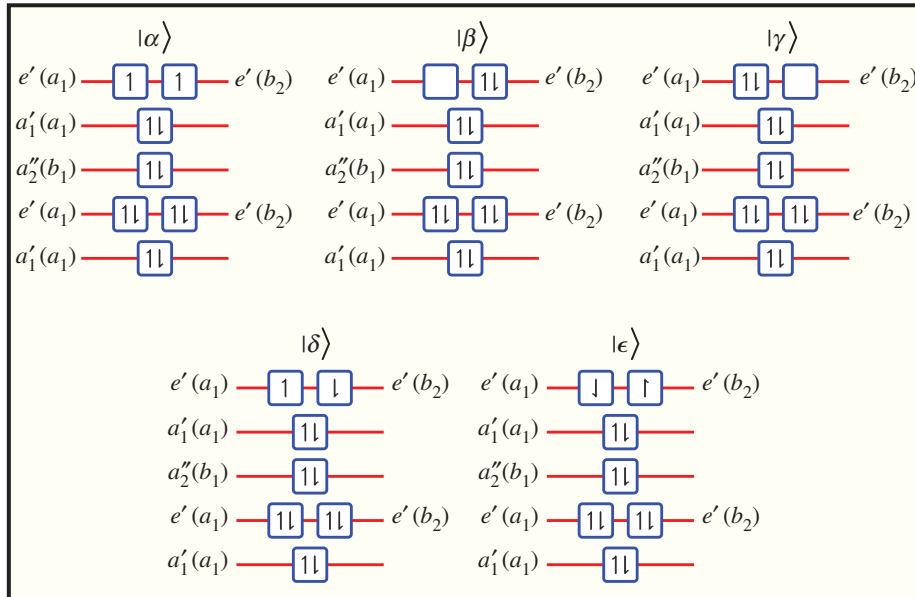


Figure 3. Slater determinants arising from $\text{HOMO} \rightarrow \text{HOMO}$ excitations in the e^2 valence configuration of C_3 (figure 2). All MOs are labelled according to D_{3h} irreps with the corresponding C_{2v} correlations given in parentheses. Up and down arrows denote α and β spin states. (Online version in colour.)

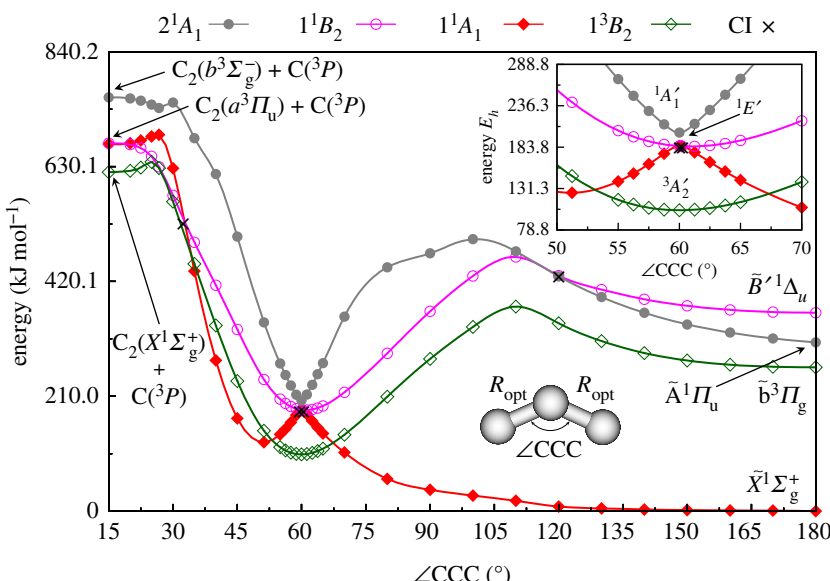


Figure 4. Optimized FVCAS/AVTZ bending potential for the four electronic states of C_3 arising from $\text{HOMO} \rightarrow \text{HOMO}$ excitations in the e^2 configuration (see equations (2.1)–(2.5)). Shown in the key are the irreps, in C_{2v} symmetry, for each state. Cis are indicated by the symbol \times . (Online version in colour.)

A close inspection of figures 1 and 4 gives an insight into the real nature of the vibronic problem. Clearly, instead of a typical linear $E' \otimes e'$ JT problem [158] in which only linear JT vibronic coupling constants are taken into account, the non-negligible contribution of the quadratic coupling constants is key for the title system (linear plus quadratic JT problem [158,159]). Additionally, an interaction occurs due to strong vibronic mixing between the close

Table 1. Properties of stationary points on ground and excited PESs of C_3 . Structures are labelled by the irrep, and energies (in kJ mol^{-1}) are relative to the $D_{\infty h}$ absolute minimum [$I-C_3(^1\Sigma_g^+)$] of the ground-state PES. Bond lengths (R), bond angles ($\angle CCC$) and harmonic vibrational frequencies (w_i) are in a_0 , degrees and cm^{-1} , respectively.

structure	method ^a	R	$\angle CCC$	ΔE	w_1	w_2	w_3
$I-C_3(^1\Sigma_g^+)$	FVCAS/AVTZ	2.474	180.0	0.0	1171.0	56.1	2060.9
	CBS			0.0			
$c-C_3(^3A'_2)$	FVCAS/AVTZ	2.629	60.0	114.6	1508.3	1064.2	1064.2
	CBS			84.2			
$d-C_3(^1B_2)$	FVCAS/AVTZ	2.629	60.9	195.5	1512.7	1124.7	3690.7
	CBS			151.3			
	equation (2.9)	2.616	60.8				
$c-C_3(^1A'_1)$	FVCAS/AVTZ	2.678	60.0	213.0	1456.3	5069.5	5069.5
	CBS			185.6			
	equation (2.9)	2.626	60.0				

^aData retrieved from [36].

lying ${}^1E'$ and ${}^1A'_1$ states [158,160]. Such a JT+PJT $[(E' + A'_1) \otimes e']$ vibronic problem introduces profound changes on the topology of the PESs near equilateral triangular geometries. Indeed, as we have first shown [36] for both the ground (${}^1A'$) and first excited (${}^1A'$) singlet states of the C_3 radical, besides the D_{3h} symmetry-required crossing seam there are three symmetry-equivalent C_{2v} seams in close proximity to the former central Ci. A cross-sectional cut of such a region is shown in figure 5 at the MRCI/AVTZ level of theory [36]. Note that $\mathbf{Q} = (Q_1, Q_2, Q_3)$ defines the standard (symmetry-adapted) JT coordinates in terms of the internuclear distances by [119,125]

$$\begin{pmatrix} Q_1 \\ Q_2 \\ Q_3 \end{pmatrix} = \begin{pmatrix} \sqrt{\frac{1}{3}} & \sqrt{\frac{1}{3}} & \sqrt{\frac{1}{3}} \\ 0 & \sqrt{\frac{1}{2}} & -\sqrt{\frac{1}{2}} \\ \sqrt{\frac{2}{3}} & -\sqrt{\frac{1}{6}} & -\sqrt{\frac{1}{6}} \end{pmatrix} \begin{pmatrix} R_1 \\ R_2 \\ R_3 \end{pmatrix}, \quad (2.6)$$

where Q_1 is the totally symmetric representation $a_1(a_1)$ or breathing mode, and (Q_2, Q_3) is the pair of $e(b_2, a_1)$ JT-active vibrations associated with the asymmetric stretch and bending normal modes, respectively. As noted above, cross sections similar to figure 5 exist for rotations by $\pm 120^\circ$, with $\rho(Q_1) = \sqrt{Q_2^2 + Q_3^2}$ being the radial polar coordinate in the 2D branching plane [$Q_b(Q_1) = (Q_2, Q_3)$]. Thus, for the circle of radius ρ_0 , the four Cis are defined by $Q_b(Q_1) = (0, 0)$, and $Q_b(Q_1) = (0, \rho_0), (-\sqrt{3}\rho_0/2, -\rho_0/2), (\sqrt{3}\rho_0/2, -\rho_0/2)$.

To model the above JT+PJT $[(E' + A'_1) \otimes e']$ vibronic problem, we write the electronic Hamiltonian (H_e) as a Taylor series expansion in the nuclear displacements from the high-symmetry D_{3h} configuration [158,160]

$$\begin{aligned} H_e(\mathbf{r}, \mathbf{Q}) &= H_e^{(0)}(\mathbf{r}, \mathbf{0}) + \sum_{\bar{F}\bar{\gamma}} \left(\frac{\partial V}{\partial Q_{\bar{F}\bar{\gamma}}} \right)_0 Q_{\bar{F}\bar{\gamma}} \\ &\quad + \frac{1}{2} \sum_{\bar{F}\bar{\gamma}} \sum_{\bar{F}_1\bar{F}_2} \left\{ \left(\frac{\partial^2 V}{\partial Q_{\bar{F}_1} \partial Q_{\bar{F}_2}} \right)_0 \right\}_{\bar{F}\bar{\gamma}} \{Q_{\bar{F}_1} \otimes Q_{\bar{F}_2}\}_{\bar{F}\bar{\gamma}} + \dots \\ &= H_e^{(0)}(\mathbf{r}, \mathbf{0}) + W(\mathbf{r}, \mathbf{Q}), \end{aligned} \quad (2.7)$$

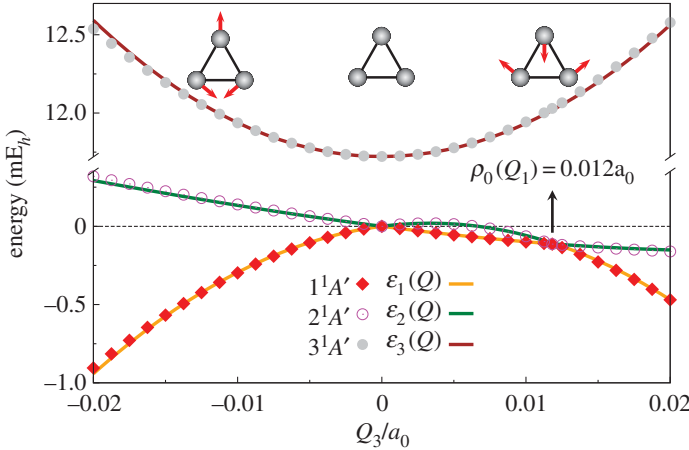


Figure 5. PES cuts along the bending coordinate Q_3 (for $Q_2 = 0$ and $Q_1 = 4.548a_0$) for the three lowest ${}^1A'$ electronic states of C_3 over the range of $-0.020a_0 \leq Q_3 \leq 0.020a_0$. Symbols indicate MRCI/AVTZ points, and the solid lines the associated eigenvalues of equation (2.9) as obtained from the least-squares fitting procedure. (Online version in colour.)

where the zeroth-order Hamiltonian $H_e^{(0)}(\mathbf{r}, \mathbf{0}) = H(\mathbf{r}) + V(\mathbf{r}, \mathbf{0})$ includes the purely electronic part [$H(\mathbf{r})$] and the electron–nuclear plus nuclear–nuclear interactions [$V(\mathbf{r}, \mathbf{0})$] with the nuclei fixed at origin (\mathbf{Q}_0); \mathbf{r} is the set of electronic coordinates and $Q_{\bar{\Gamma}\bar{\gamma}}$ are symmetrized nuclear displacements (see equation (2.6)) which transform according to the line $\bar{\gamma}$ of the D_{3h} irrep $\bar{\Gamma}$. In turn, $W(\mathbf{r}, \mathbf{Q})$ is the vibronic coupling perturbative operator whose matrix elements (vibronic constants) measure the effect of changes in the electronic structure upon nuclear motion [158,160]. Note that $\{(\partial^2 V / \partial Q_{\bar{\Gamma}_1} \partial Q_{\bar{\Gamma}_2})_0\}_{\bar{\Gamma}\bar{\gamma}}$ defines an irreducible product [161] (tensor convolution [158]); this is a linear combination of second derivatives with respect to $Q_{\bar{\Gamma}_1}$ and $Q_{\bar{\Gamma}_2}$, which transforms according to the line $\bar{\gamma}$ of the D_{3h} irrep $\bar{\Gamma} \subset \bar{\Gamma}_1 \otimes \bar{\Gamma}_2$. Likewise, $\{Q_{\bar{\Gamma}_1} \otimes Q_{\bar{\Gamma}_2}\}_{\bar{\Gamma}\bar{\gamma}}$ denotes the irreducible product for the corresponding symmetrized coordinates.

The starting point consists therefore of solving the electronic Schrödinger equation with the nuclei fixed at the origin

$$H_e^{(0)}(\mathbf{r}, \mathbf{0})|\varphi_k(\mathbf{r}, \mathbf{0})\rangle = \mathcal{E}_k(\mathbf{0})|\varphi_k(\mathbf{r}, \mathbf{0})\rangle, \quad (2.8)$$

where $\{|\varphi_k\rangle\} = \{|\Psi_2 {}^1E'(1^1A_1)\rangle, |\Psi_3 {}^1E'(1^1B_2)\rangle, |\Psi_4 {}^1A'_1(2^1A_1)\rangle\}$ is the orthonormal set of eigenvectors (the eigenvalues are $\{\mathcal{E}_k(\mathbf{0})\}$) used here to approximate the electronic function space with the nuclei clamped at \mathbf{Q}_0 . The corresponding matrix representation of the electronic Hamiltonian H_e (equation (2.7)) in such a basis assumes the form [36,162]

$$\mathbf{H}_e = \begin{pmatrix} -F_{E'}Q_3 + \kappa_{E'} - G_{E'}(Q_2^2 - Q_3^2) & F_{E'}Q_2 + 2G_{E'}Q_2Q_3 & H_{E'/A'_1}Q_3 \\ F_{E'}Q_2 + 2G_{E'}Q_2Q_3 & F_{E'}Q_3 + \kappa_{E'} + G_{E'}(Q_2^2 - Q_3^2) & H_{E'/A'_1}Q_2 \\ H_{E'/A'_1}Q_3 & H_{E'/A'_1}Q_2 & \Delta + \kappa_{A'_1} \end{pmatrix}, \quad (2.9)$$

where $\kappa_{E'}(\mathbf{Q}) = \frac{1}{2}K_{E'}(Q_2^2 + Q_3^2)$ and $\kappa_{A'_1}(\mathbf{Q}) = \frac{1}{2}K_{A'_1}(Q_2^2 + Q_3^2)$ are harmonic potentials for the ${}^1E'$ and ${}^1A'_1$ electronic states centred at \mathbf{Q}_0 , with force constants $K_{E'}$ and $K_{A'_1}$, respectively. In turn, $F_{E'}$ and $G_{E'}$ are linear and quadratic JT vibronic coupling constants, respectively, and H_{E'/A'_1} is the associated linear PJT parameter [36,162]. Correspondingly, Δ denotes the energy gap (at the origin) between the vibronically mixed ${}^1E'$ and ${}^1A'_1$ terms. Note that the vibronic coupling constants of equation (2.9) can be obtained from group-theoretic considerations [158,161]; see appendix A. They were all determined from a fit to *ab initio* MRCI/AVTZ energies, with the numerical values and definition given in table 2. As seen, the linear JT vibronic constant ($F_{E'}$) is small: about 1 and 2 orders of magnitude smaller than H_{E'/A'_1} and $G_{E'}$, respectively. This is the signature of the so-called small linear parameter (SLP) JT molecules [159,163].

Table 2. Vibronic coupling constants and parameters in equation (2.9). The numerical data were obtained from a fit to the *ab initio* MRCI/AVTZ energies in figure 5.

parameter ^a	expression ^b	value ^c
$K_{E'}$	$\left\langle {}^1E'_{\theta/\epsilon} \left \left(\frac{\partial^2 V}{\partial Q_2^2} \right)_0 + \left(\frac{\partial^2 V}{\partial Q_3^2} \right)_0 \right {}^1E'_{\theta/\epsilon} \right\rangle$	351.3 ^c
$K_{A'_1}$	$\left\langle {}^1A'_1 \left \left(\frac{\partial^2 V}{\partial Q_2^2} \right)_0 + \left(\frac{\partial^2 V}{\partial Q_3^2} \right)_0 \right {}^1A'_1 \right\rangle$	399.0 ^c
$F_{E'}$	$\left\langle {}^1E'_{\epsilon} \left \left(\frac{\partial V}{\partial Q_3} \right)_0 \right {}^1E'_{\epsilon} \right\rangle$	11.8 ^d
$G_{E'}$	$\left\langle {}^1E'_{\epsilon} \left \left(\frac{\partial^2 V}{\partial Q_2^2} \right)_0 - \left(\frac{\partial^2 V}{\partial Q_3^2} \right)_0 \right {}^1E'_{\epsilon} \right\rangle$	1940.0 ^c
H_{E'/A'_1}	$\left\langle {}^1E'_{\epsilon} \left \left(\frac{\partial V}{\partial Q_2} \right)_0 \right {}^1A'_1 \right\rangle$	150.8 ^d
Δ		11.7 ^e

^aRef. [36].^bThe following symmetry correlations have been employed: $|\Psi_2 {}^1E'({}^1A_1)\rangle \equiv |{}^1E'_{\theta}\rangle$, $|\Psi_3 {}^1E'({}^1B_2)\rangle \equiv |{}^1E'_{\epsilon}\rangle$ and $|\Psi_4 {}^1A'_1({}^2A_1)\rangle \equiv |{}^1A'_1\rangle$.^cUnits in $mE_h a_0^{-2}$.^dUnits in $mE_h a_0^{-1}$.^eUnits in mE_h .

The solutions of the present JT+PJT vibronic problem are shown in figures 5 and 6. Clearly, the model reproduces the full picture of the adiabatic PESs near D_{3h} symmetry, including the cusped behaviour at all electronic degeneracies and vibronic mixing between close-in-energy terms. Interestingly, the current three-state JT+PJT model Hamiltonian also predicts a stationary point (labelled d -C₃(1B_2)) in the ${}^2A'$ electronic state. Such a structure has been confirmed by *ab initio* FVCAS/AVTZ optimizations, and shown to be a minimum (table 1). Note that the PJT vibronic effect provides an additional stabilization of the undistorted D_{3h} minimum of the ${}^3A'$ state. Note also from table 1 that the predicted structures agree well with the *ab initio* ones.

(c) The Longuet–Higgins sign-change theorem

As stated by the Longuet–Higgins theorem [164]: if a real-valued electronic wave function changes sign when adiabatically transported around a closed circuit C in the two-dimensional branching plane, then it must become discontinuous and degenerate with another state at an odd number of points lying on that surface and within that loop [164–166].

Varandas *et al.* [167] were the first to demonstrate the numerical validity of such sign-reversal criterion for LiNaK by following the variation of the dominant coefficients in the ground-state wave function along a path that encircles the crossing point [167]. We have followed the same approach with state-averaged FVCAS/AVTZ calculations. The results are shown in figure 7.

As first pointed out by Zwanziger & Grant [159], for SLP JT molecules the additional three symmetry-equivalent C_{2v} seams may prevent the associated electronic wave function of changing sign when transported around a loop enclosing the four Cis. In other words, the net geometric phase (GP) effect [164–166] is largely suppressed. Consider first the case in which a circular path is chosen such that $\rho < \rho_0(Q_1)$ (figure 7a). In this case, only one Ci (the central one) is enclosed and the adiabatic wave function changes sign along this loop, as seen in figure 7a for the ${}^1A'$ and ${}^2A'$ electronic states. In fact, a similar sign change is expected when only one of the three equivalent degeneracies of C_{2v} symmetry is encircled (figure 7b). Conversely, as figure 7c

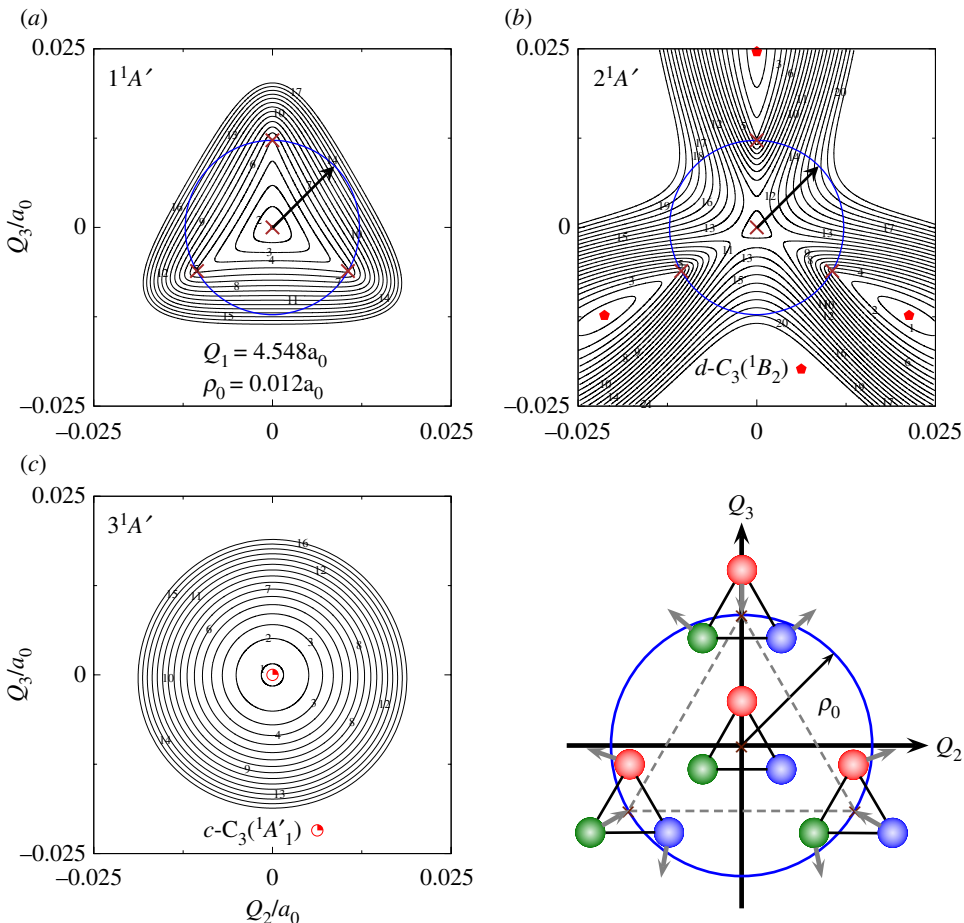


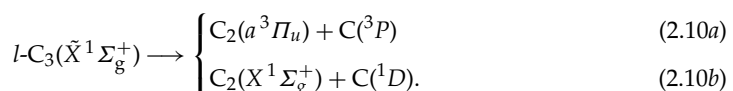
Figure 6. Contour plot of the lowest eigenvalues of the JT+PJT vibronic Hamiltonian of C_3 (equation (2.9)) for $Q_1 = 4.548a_0$; (a) $1^1A'$; (b) $2^1A'$; (c) $3^1A'$. Contours in (a) are equally spaced by -0.0300 mE_h starting at 0.0000 mE_h , with values of 0.0168 mE_h and -0.2000 mE_h for (b), and 0.0500 mE_h and 11.7224 mE_h for (c). Cis are indicated by crosses (\times). (Online version in colour.)

shows, a closed circuit enclosing both the central and one of the C_{2v} Cis is sign-preserving. By the same token, when $\rho > \rho_0(Q_1)$ (figure 7d), the associated electronic adiabatic wave function is sign-unchanged upon transportation along the corresponding loop. Note that $\rho_0(Q_1)$ marks the important transition between a JT- and RT-like behaviour in the sense that the adiabatic wave functions for the $1^1A'$ and $2^1A'$ electronic states experience a sign change upon adiabatic transportation about the origin (D_{3h} seam) in the case $\rho < \rho_0(Q_1)$, but not for $\rho > \rho_0(Q_1)$ [159]. Note also from figure 7 that the adiabatic wave function for the $3^1A'$ state does not change sign in any of the cases mentioned above: it is non-JT in nature.

(d) Global potential energy surfaces

(i) Accurate DMBE forms

According to the spin–spatial Wigner–Witmer correlation rules [156,157], $l\text{-}C_3(\tilde{X}^1\Sigma_g^+)$ dissociates adiabatically into



$$(2.10b)$$

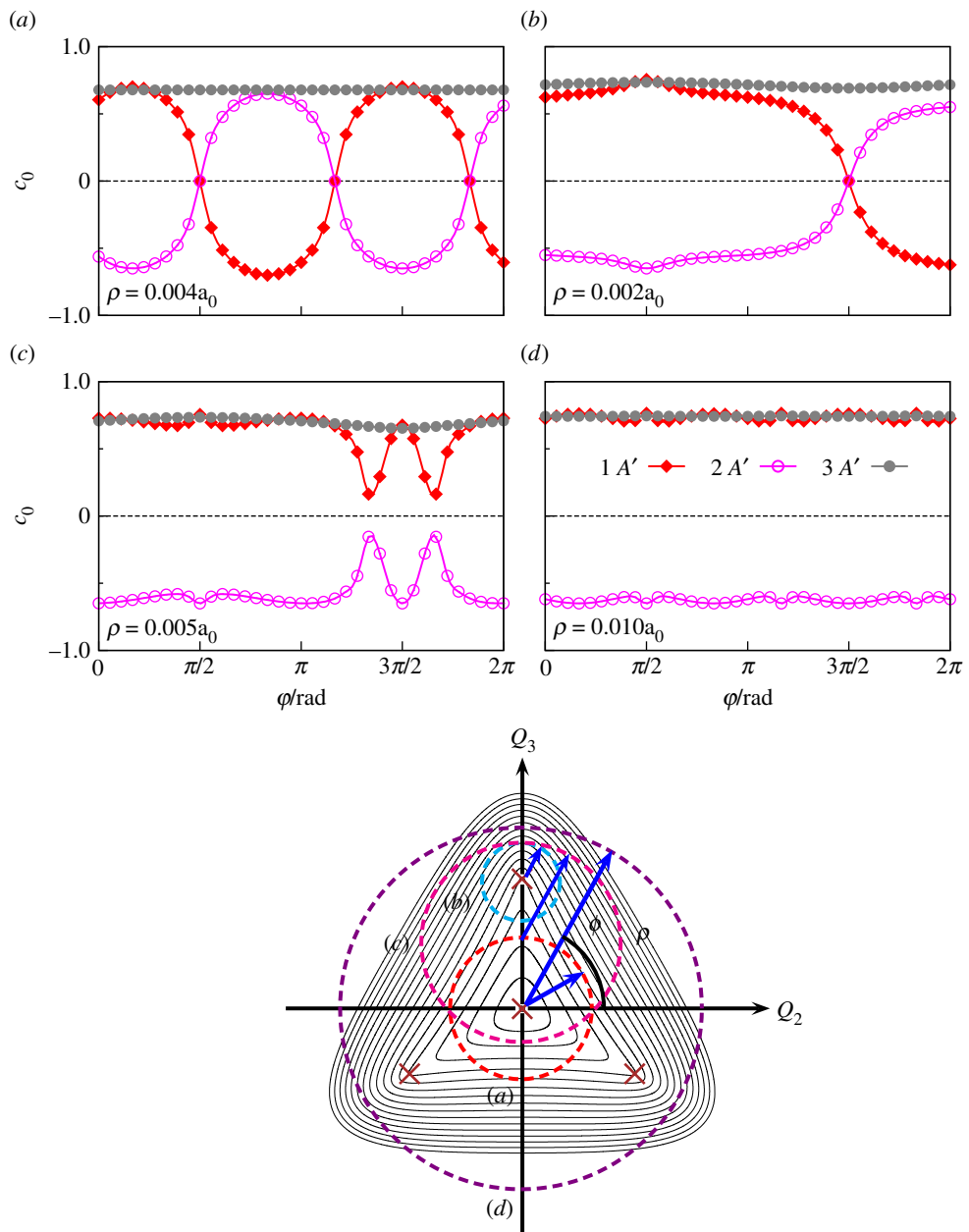


Figure 7. Adiabatic evolution of the $1^1A'$, $2^1A'$ and $3^1A'$ wave functions of C_3 along a closed circuit C in the two-dimensional branching plane encircling one or more Cis; c_0 is the coefficient of the leading determinant (CSF) of the FVCAS/AVTZ wave function for each state. Four closed loops are considered that encircle: (a) the central (D_{3h}) Ci; (b) one C_{2v} Ci; (c) two Cis; (d) four Cis. See also text. (Online version in colour.)

As noted elsewhere [105–107,119], the first excited triplet state of C_2 lies only 8.6 kJ mol^{-1} (the term value T_e) above the corresponding ground state [48], whereas the energy separation between the 3P state of atomic carbon and its first excited state $C({}^1D)$ is $122.0 \text{ kJ mol}^{-1}$ [168]. Thus, as figure 1 shows, the lowest channel $C_2(a^3\Pi_u) + C({}^3P)$ is favoured by $113.4 \text{ kJ mol}^{-1}$ relative to $C_2(X^1\Sigma_g^+) + C({}^1D)$.

Table 3. Functional representation of the three-body EHF energy terms shown in equation (2.12) for the DMBE I and DMBE II PESs.

X	$V_{x,\text{EHF}}^{(3)}$	$V_{x,\text{EHF}}''^{(3)}$	$V_{x,\text{EHF}}'''^{(3)}$
I ^a	$(P_1^N - \sqrt{T_2} P_2^M) T'_1$	$(P_3^{N'} - \Delta_1 \Delta_2 \Delta_3 P_4^{M'}) T''_1$	0
II ^b	$(P_1^N - \mathcal{F}_{nJT} \sqrt{T_2} P_2^M) T'_{ }$	$(P_3^{N'} - \mathcal{F}_{nJT} \sqrt{T_2} P_4^{M'} - \Delta P_5^{P''}) T''_{ }$	$(P_6^{N'''} - \mathcal{F}_{nJT} \sqrt{T_2} P_7^{M'''} - \Delta P_8^{P''''}) T'''_{ }$

^aDMBE I of [35].^bDMBE II of [116].

In [35,116], we modelled the adiabatic ground-state PES of C_3 by

$$V_{\text{I/II}}(\mathbf{R}) = V^{(1)}(\mathbf{R}) + V^{(2)}(\mathbf{R}) + V_{\text{dc}}^{(3)}(\mathbf{R}) + V_{\text{I/II,EHF}}^{(3)}(\mathbf{R}), \quad (2.11)$$

where [124,125] $V^{(1)}$ is a one-body term equal to the dissociation energy (D_e) of $C_2(a^3\Pi_u)$, $V^{(2)}(\mathbf{R})$ is the sum of the two-body potentials and $V_{\text{dc}}^{(3)}(\mathbf{R})$ is the three-body dc. In both DMBE I and DMBE II potentials, the three-body EHF energy assumes the form [35,116]

$$V_{\text{I/II,EHF}}^{(3)}(\mathbf{R}) = V_{\text{I/II,EHF}}^{(3)}(\mathbf{R}) + V_{\text{I/II,EHF}}''^{(3)}(\mathbf{R}) + V_{\text{I/II,EHF}}'''^{(3)}(\mathbf{R}), \quad (2.12)$$

where $V_{\text{I/II,EHF}}^{(3)}(\mathbf{R})$ is responsible for introducing non-analyticity into the potential along the line of D_{3h} symmetry, and the remaining terms provide the required cusp behaviour at the C_{2v} degeneracies. The corresponding forms are presented in table 3; for simplicity, obvious coordinate dependences have been eliminated. Note that $P_n^J(\Gamma_1, \Gamma_2, \Gamma_3)$ are J th-order polynomials expressed in the integrity basis [169] and the $T(\mathbf{R})$'s are range-decaying factors. In turn, $\sqrt{T_2} = (Q_2^2 + Q_3^2)^{1/2}$ is the so-called JT-type coordinate [120,170] which essentially measures the distance from any point in the (Q_2, Q_3) -plane to the D_{3h} Ci (where $Q_b(Q_1) = (0, 0), \forall Q_1$) [127,128]. Likewise, $\Delta_1 \Delta_2 \Delta_3$ is the (product of) distances from any point in \mathbf{R} -space to the three permutationally equivalent C_{2v} crossing seams. Note that $V_{\text{I,EHF}}''^{(3)}(\mathbf{R})$ dies off Gaussian-like [127] in DMBE I, and hence the cusps at such geometries are warranted only close to the minimum of the crossing seam [35]. All major topographical features are shown in figure 8.

As we have shown elsewhere [36], the three C_{2v} seams are not static with respect to the D_{3h} Ci but evolve instead with the size of the molecule. In so doing, such degeneracy points approach the central D_{3h} Ci almost linearly and ultimately coalesce with it, thence forming a node of confluence. Indeed, by increasing the size of the molecular triangle, the C_{2v} disjoint seams get rotated by $\pm\pi$ in the branching plane [36]. To mimic such a behaviour, we suggested a DMBE II form [116] and a novel coordinate (Δ in table 3) that incorporates by built-in construction the exact equation of the seam as a function of Q_1 . Likewise the JT coordinate, Δ assumes the form [116]

$$\Delta = \sqrt{S_2^2 + S_3^2}, \quad (2.13)$$

where S_2 and S_3 are symmetrized coordinates made of the distances $\Delta = \{\Delta'_1, \Delta'_2, \Delta'_3\}$ from an arbitrary point to the C_{2v} Cis [116]:

$$\Delta'_c = \sqrt{(Q_2 - Q_2^c)^2 + (Q_3 - Q_3^c)^2} \quad c = 1, 2, 3, \quad (2.14)$$

with the disjoint crossings point (Q_2^c, Q_3^c) given by

$$(Q_2^c, Q_3^c) = (\rho_0 \cos(\varphi_c \pm n\pi), \rho_0 \sin(\varphi_c \pm n\pi)). \quad (2.15)$$

As in §3b,c, ρ_0 denotes the radius at which the disjoint seams are located with respect to the central Ci and φ_c ($c = 1, 2, 3$) is the polar angle that explicitly defines the positions of the crossings: $\varphi_1 = \pi/2$, $\varphi_2 = 7\pi/6$ and $\varphi_3 = 11\pi/6$ (see figure 7). In equation (2.15), $n = 0$ or 1 is an integer that

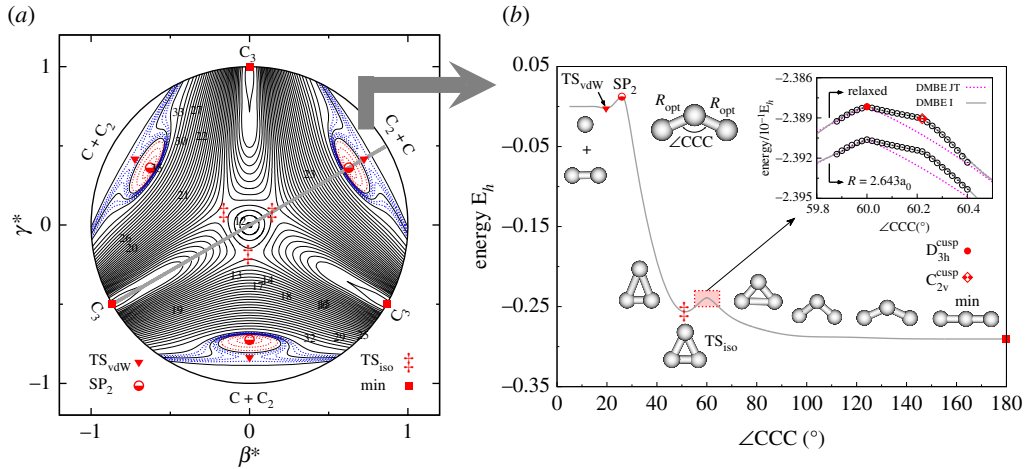


Figure 8. (a) Relaxed triangular plot in hyperspherical coordinates [171] depicting the location and symmetry of all stationary points of the DMBE I PES for ground-state C_3 . Solid black lines are equally spaced by $0.005 E_h$, starting at $-0.2904 E_h$. Dashed red and blue lines are equally spaced by $0.001 E_h$, starting at $0.00067 E_h$ and $-0.0206 E_h$, respectively. (b) Optimized reaction path along C_{2v} arrangements. The plot starts at $\angle CCC = 5^\circ$, which corresponds to the $C + C_2$ limit and leads to the linear global minimum at $\angle CCC = 180^\circ$ via the Ci region. The insert shows an amplified view of the nuclear configuration space illustrating the correct cusped behaviour at the D_{3h} and C_{2v} crossing seams. The dots indicate fitted points, with the lowest curve shifted by $-0.0025 E_h$ for visibility. Indicated by DMBE JT is the PES without the $V_{1,\text{EHF}}^{(3)}(\mathbf{R})$ contributions in table 3. (Online version in colour.)

accounts for the proper rotation-in-plane of the C_{2v} seams on passing through the confluence point [116]. The equation of the seam is self-contained in the proper definition of ρ_0 , and is accurately represented by

$$\rho_0(Q_1) = \left| \varrho - \delta \tanh \left[\sum_{i=1}^5 \xi_i (Q_1 - Q_1^0)^i \right] \right|, \quad (2.16)$$

where ϱ , δ , ξ_i and Q_1^0 are adjustable parameters; the details are given elsewhere [116]. As figure 9 shows, Δ is capable of accurately modelling the three symmetry-equivalent C_{2v} disjoint seams, in addition to the symmetry-required D_{3h} one, over the entire configuration.

One wonders at this stage about the topographical form of the PES when all Cis meet each other. As shown in figure 9, at this point of all confluentes the PESs become tangentially touching paraboloids rather than two cones connected by the vertex. To mimic such a behaviour, it suffices to add a term $\mathcal{F}_{\text{JT}}(\mathbf{R})$ (non-JT factor) that warrants the $\sqrt{I_2}$ singularity on the adiabatic PESs to be cancelled out (table 3). The result, obtained from the DMBE II PES, is illustrated in figure 9, which shows the evolution of such crossings versus Q_1 . Table 4 presents only the properties of the linear global minima. The agreement with experimental data is good, while the properties of other stationary points (not shown) agree well with the corresponding *ab initio* attributes [35,116].

(ii) Realistic ES/DMBE forms

To improve the C_3 DMBE II PES at the linear global minima, we used [117] a simplified version of Varandas' ES scheme [173] to morph DMBE II and the ABW [34] and SS [115] local functions. Both DMBE/ES/ABW and DMBE/ES/SS PESs so obtained [117] read

$$V_{\text{DMBE/ES}/x} = f(\Delta E)[V_{\text{DMBE II}}(\mathbf{R}) - V_x(\mathbf{R})] + V_x(\mathbf{R}), \quad (2.17)$$

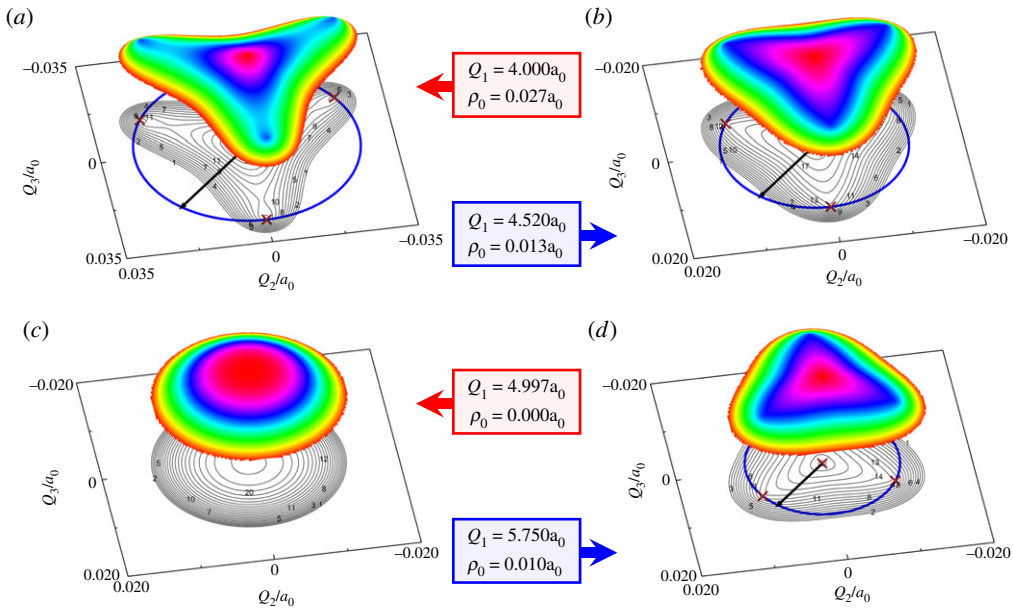


Figure 9. Evolution of D_{3h} and C_{2v} crossing seams versus Q_1 as predicted from the DMBE II PES for ground-state C_3 : (a) $Q_1 = 4.000a_0$; (b) $Q_1 = 4.520a_0$; (c) $Q_1 = 4.997a_0$; (d) $Q_1 = 5.750a_0$. Contours are spaced as follows (from (a) to (d)): 0.025 mE_h, starting at $-0.1710 E_h$; 0.015 mE_h, starting at $-0.2392 E_h$; 0.012 mE_h, starting at $-0.2081 E_h$ and 0.022 mE_h, starting at $-0.1048 E_h$. Cis are indicated by crosses. (Online version in colour.)

Table 4. Properties of the global linear minima on the $C_3(1^1A')$ DMBE PESs. Relative energies (ΔE), bond lengths (R_i) and harmonic frequencies (w_i) are in kJ mol⁻¹, a₀ and cm⁻¹, respectively.

method	R_1	R_2	R_3	ΔE	w_1	w_2	w_3
DMBE I ^a	4.888	2.444	2.444	0.0 ^b	1204.2	63.5	2126.5
DMBE II ^c	4.888	2.444	2.444	0.0	1203.9	61.0	2125.5
DMBE/ES/ABW ^d	4.920	2.460	2.460	0.0	1214.5	64.6	2109.8
DMBE/ES/SS ^d	4.890	2.445	2.445	0.0	1206.7	42.8	2101.3
Expt.	4.902	2.451	2.451 ^e		1224.49 ^f	63.42 ^f	2040.02 ^f
	4.890	2.445	2.445 ^g				

^aRef. [35].

^bRelative to the $C_3(1^1\Sigma_g^+)$ global minimum.

^cRef. [116].

^dRef. [117].

^eRef. [4].

^fRefs. [84,172]. Separation between origin level and lowest $v_n = 1$ level.

^gMixed theoretical/experimental approach of Refs. [85,115].

where $x = \text{ABW}$ or SS , and $f(\Delta E)$ is defined by [173]

$$f(\Delta E) = \begin{cases} \exp \left[-\beta \left(\frac{\Delta E_0}{\Delta E + \xi} - 1 \right)^n \right] & \text{if } \Delta E < \Delta E_0 \\ 1 & \text{if } \Delta E \geq \Delta E_0. \end{cases} \quad (2.18)$$

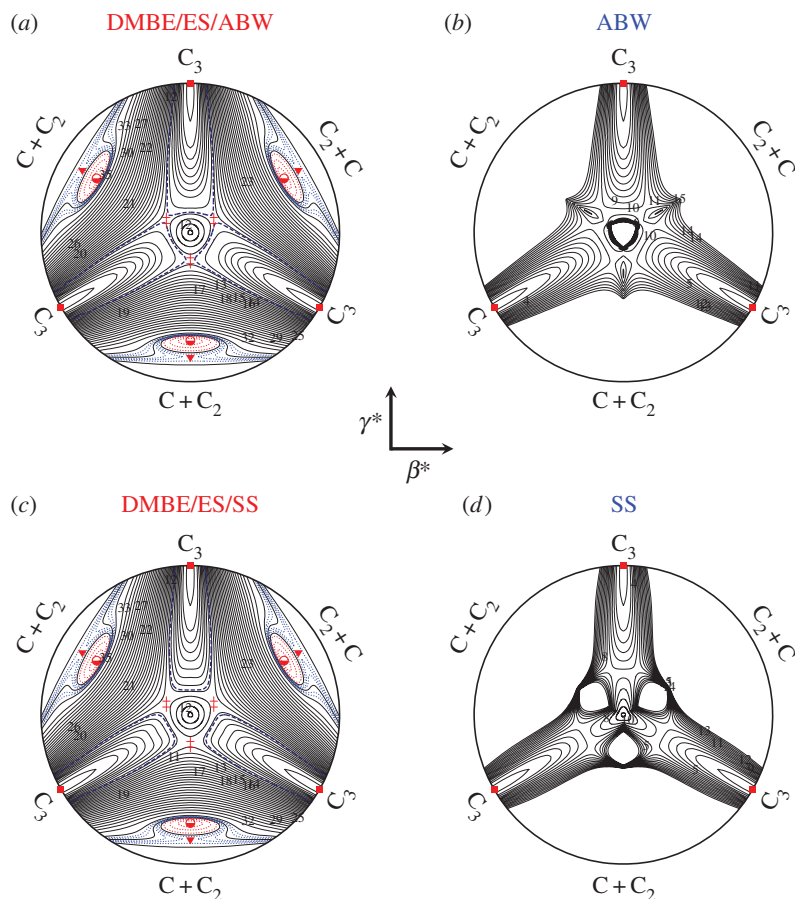


Figure 10. Relaxed triangular plot in hyperspherical coordinates [171] for C_3 : (a) DMBE/ES/ABW [117]; (b) ABW [34]; (c) DMBE/ES/SS [117]; (d) SS [115]. Key for all global forms are as in figure 8. For local forms, contours are equally spaced by $0.005 E_h$, starting at $-0.2904 E_h$. Navy dashed lines in panels (a) and (c) define cut-off energies (E_0) of equation (2.18). (Online version in colour.)

Table 5. Stratified root-mean-square deviations (in cm^{-1}) obtained for 100 calculated energy levels for $J \leq 1$.

energy ^a	N ^b	RMSD					
		DMBE/ES/ABW	ABW	DMBE/ES/SS	SS	DMBE II	DMBE I
1000	8	3.3	3.2	2.5	2.3	24.5	32.5
2000	17	3.3	2.8	7.3	6.9	38.9	41.8
3000	35	4.2	2.6	9.7	9.1	37.5	47.0
4000	49	8.2	2.7	13.2	11.1	40.1	48.1
6000	83	18.0	3.0	19.8	13.4	42.2	49.0
9000	100	26.9	2.9	31.0	12.5	45.7	53.4

^aThe units of energy are cm^{-1} . Energy strata defined relative to the corresponding zero-point energy level.

^bNumber of vibrational states up to indicated energy range.

In turn, $\Delta E = E - E_{\min}$ is the energy displacement with respect to the absolute global minima of the DMBE II PES, and $\Delta E_0 = E_0 - E_{\min}$ is the energy difference between E_{\min} and the cut-off energy E_0 . Finally, β is a trial-and-error parameter, n is an even integer and ξ a small number chosen to avoid numerical overflows at $E = E_{\min}$. Clearly, $f(\Delta E)$ ensures that the resulting PESs converge to the local potentials at energy ranges near E_{\min} , while smoothly changing to the global PES as long as the energy approaches E_0 . The topographical features of the final ES PESs are shown in figure 10, together with the used local potentials. Clearly, the ES scheme allows a convenient merge of the global and local forms while eliminating spurious holes in the latter near equilateral triangular geometries. Additionally, they allow an extension of such spectroscopic forms to the dissociative regions. Their reliability is illustrated in table 5, which summarizes stratified RMSDs for 100 rovibrational energy levels up to 9000 cm^{-1} above the ZPE.

As seen, near-spectroscopic accuracy is conveyed to both global forms up to 4000 cm^{-1} above the ZPE, while keeping unaltered all attributes of the original DMBE II PES (table 4). Not surprisingly, discrepancies appear with increasing energy, particularly for DMBE/ES/ABW because the original PESs differ most. Despite this, a reduction of approximately 20 cm^{-1} in levels up to 9000 cm^{-1} is already an asset of the ES method [173].

3. Further on carbon tetramer

(a) Electronic structure

All structures have been optimized with MOLPRO [174] at the CASSCF (or, simply, CAS) level of theory [175] in C_1 symmetry with the AVTZ basis set [60,61]. The reference wave functions have then been obtained using the largest possible active space, which involves 8 correlated electrons in 12 orbitals (CAS(8,12)); 8 orbitals were treated as inactive, but optimized, throughout all calculations. Geometry optimizations were also done, and followed by harmonic vibrational analysis to confirm the nature of the stationary point as minima (only real frequencies) or transition-state structures (only one imaginary frequency). To understand the connections between the predicted transition states and associated minima, calculations along convenient ORC paths [176,177] have further been carried out. This involves a selection of a single reactive coordinate, i.e. the one that determines the bond-breaking/bond-forming process, with all other degrees of freedom fully optimized at each point of the predefined grid for the active coordinate. Such a process has proved very effective in obtaining accurate reaction dissociation profiles for HO_3 [176], HO_2 and HS_2 [177] as well as for the $\text{Li}_3\text{N}-\text{CO}_2$ complex [178]. For every point of the various ORCs, an enhanced estimate of the energetics has then been obtained at the MRCI(Q) level [175] with AVTZ and AVQZ basis sets, followed by extrapolation to the CBS limit [179,180]. Suffice it to add that all CAS(8,12) vectors were included in the reference space for the 8-electron MRCI(Q)-8 calculations; the 8 inner orbitals were left uncorrelated.

For CBS extrapolation of the CAS energies, a double-level protocol developed in our group [179] has been used,

$$E_X^{\text{CAS}(8,12)}(\mathbf{R}) = E_\infty^{\text{CAS}(8,12)}(\mathbf{R}) + A e^{-1.63x}, \quad (3.1)$$

where $x = t(2.94), q(3.87)$ are hierarchical numbers [181,182] associated with the $X = T : 3, Q : 4$ cardinals and \mathbf{R} is a six-dimensional coordinate vector; $E_\infty^{\text{CAS}(8,12)}(\mathbf{R})$ and A are parameters obtained from the fit to the CAS(8,12)/AVXZ ndc energies.

In turn, the extrapolated dc contribution [$E_\infty^{\text{dc-8}}(\mathbf{R})$] is obtained with Varandas' USTE protocol [180]

$$E_X^{\text{dc-8}}(\mathbf{R}) = E_\infty^{\text{dc-8}}(\mathbf{R}) + \frac{A_3}{(X - 3/8)^3} + \frac{A_5(0) + c A_3^{5/4}}{(X - 3/8)^5}, \quad (3.2)$$

where $A_5(0)$ and c are universal parameters [180], and $E_\infty^{\text{dc-8}}(\mathbf{R})$ and A_3 are obtained by fitting the raw MRCI(Q)-8/AVXZ dc energies:

$$E_X^{\text{dc-8}}(\mathbf{R}) = E_X^{\text{MRCI}(Q)-8}(\mathbf{R}) - E_X^{\text{CAS}(8,12)}(\mathbf{R}). \quad (3.3)$$

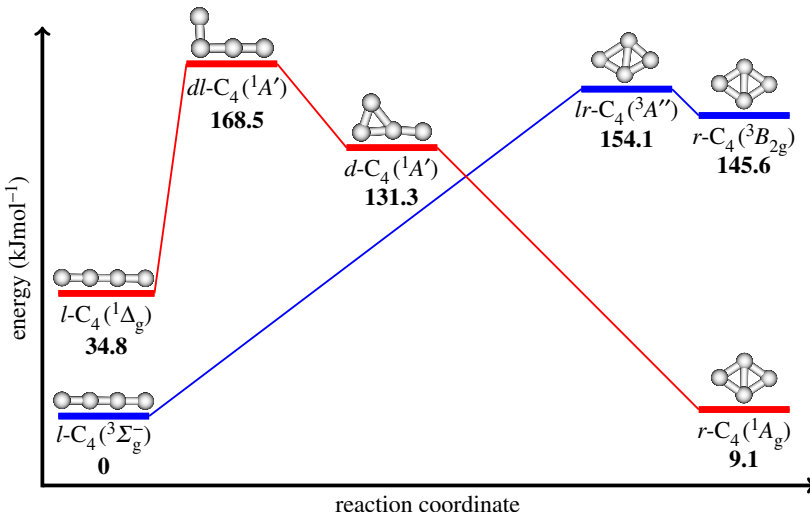


Figure 11. Minimum energy paths for interconversion of linear and rhombic C_4 in both the triplet (blue online) and singlet (red) ground-state PESs. Energies are given with respect to the $l\text{-}\text{C}_4(^3\Sigma_g^-)$ form and have been obtained at the ve-CASDC/CBS level of theory. Structural parameters and vibrational frequencies for each structure are in tables 6 and 7. (Online version in colour.)

For a specified nuclear arrangement \mathbf{R} , the total energy is then obtained as

$$E_{\infty}^{\text{CASDC/CBS-8}}(\mathbf{R}) = E_{\infty}^{\text{CAS}(8,12)}(\mathbf{R}) + E_{\infty}^{\text{dc-8}}(\mathbf{R}), \quad (3.4)$$

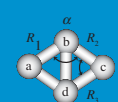
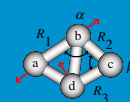
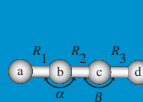
and denoted by CASDC/CBS-8 as suggested elsewhere [177].

As noted by Parasuk & Alm  f [37], the inclusion of all valence electrons in the correlation treatment is key to obtaining the best energy differences between the linear and cyclic forms. Thence, we carried out FVCAS geometry optimizations with the AVTZ basis set, followed by single-point AVQZ computations. Such calculations involve correlating the 16 electrons in 16 orbitals, which are affordable only by including point-group symmetry in the wave function. Because this could not be pursued for stationary points of symmetry lower than C_{2v} , single-point FVCAS/AVXZ calculations were performed at the optimum CAS(8,12)/AVTZ geometries. To obtain a reliable estimate of the total CBS energy, the ndc extrapolated components $E_{\infty}^{\text{CAS}(16,16)}(\mathbf{R})$ were added to the $E_{\infty}^{\text{dc-8}}(\mathbf{R})$ contributions, with the energies so obtained denoted as ve-CASDC/CBS. Figure 11 shows the minimum energy pathways for interconversion between the linear and rhombic C_4 for both triplet and singlet isomers. The corresponding structural parameters, harmonic vibrational frequencies and relative energies are given in tables 6 and 7.

Some remarks are due at this point on the $l\text{-}\text{C}_4(^3\Sigma_g^-)$ and $r\text{-}\text{C}_4(^1A_g)$ energetics. As noted in the Introduction, it is a common trend [37,38,132] that the singlet versus triplet relative positioning, and hence the ground-state structure, depends on whether SR versus MR methodologies are used: $r\text{-}\text{C}_4(^1A_g)$ is found more stable than $l\text{-}\text{C}_4(^3\Sigma_g^-)$ at the SR level, while the reverse is true for MR. Indeed, as noted by Parasuk & Alm  f [37], SR approaches may not be sufficient to treat adequately the high density of electronic states present in C_4 which occur already for very low internal energies [38]. Our own calculations at the CASDC/CBS-8 level suggest from tables 6 and 7 that $l\text{-}\text{C}_4(^3\Sigma_g^-)$ lies about 25.9 kJ mol^{-1} lower in energy than the corresponding rhombic singlet structure. However, at our highest level of theory, i.e. ve-CASDC/CBS, the linear-rhombic energy difference is reduced to only 9.1 kJ mol^{-1} (positive signs favours the linear form). These results are in good agreement with those obtained by Parasuk and Alm  f in their 16-electron MRCI/G[542] calculations (6.8 kJ mol^{-1}) [37]. Although such relative quantity certainly converges to different values for distinct correlation methods, extrapolations to the CBS limit tend to level their relative positioning; the isomer with larger correlation energy, i.e. $r\text{-}\text{C}_4(^1A_g)$ tends to be favoured. Indeed,

Table 6. Structural parameters (distances R_i in a_0 , angles in degrees) and vibrational frequencies (in cm^{-1}) of the stationary points on the ground-state triplet PES of C_4 . Energies (in kJ mol^{-1}) relative to $l\text{-}\text{C}_4(^3\Sigma_g^-)$. (Online version in colour.)

feature/method	$l\text{-}\text{C}_4(^3\Sigma_g^-)$	$lr\text{-}\text{C}_4(^3A'')$	$r\text{-}\text{C}_4(^3B_{2g})$
	$D_{\infty h}$	C_s	D_{2h}
CAS(8,12)/AVTZ ^a	0.0	229.0	220.9
FVCAS/AVTZ ^a	0.0	122.5	105.5
CASDC/CBS-8 ^a	0.0	262.4	261.0
ve-CASDC/CBS ^a	0.0	154.1	145.6
R_1^b	2.458(2.506) ^{c,d}	3.076	2.698(2.744) ^c
R_2	2.449(2.463) ^c	2.604	2.698(2.744) ^c
R_3	2.458(2.506) ^c	2.637	2.698(2.744) ^c
α	180.0(180.0) ^c	105.6	111.4(112.8) ^c
β	180.0(180.0) ^c	70.4	68.6(67.2) ^c
w_1^b	2165.0(2057.0) ^e	1347.1	1316.2
w_2	949.3	1325.9	1038.4
w_3	1667.2(1548.9) ^e	992.0	877.3
w_4	538.8(323.0) ^e	706.0	665.5
w_5	216.0(174.0) ^e	552.2	618.2
w_6		392.1 <i>i</i>	608.8

^aThis work.^bObtained at CAS(8,12)/AVTZ level of theory.^cFVCAS/AVTZ optimized values.^dThe experimentally averaged C=C bond length is $2.458a_0$ [2].^eExperimental band origins taken from [8,146,148].

the energy splittings predicted from our (FVCAS + dc-8)/AVTZ, (FVCAS + dc-8)/AVQZ and ve-CASDC/CBS calculations are 14.7, 11.2 and 9.1 kJ mol^{-1} , respectively. A similar basis-set effect is also observed in the MRCI(Q)-8/AVTZ, MRCI(Q)-8/AVQZ and CASDC/CBS-8 series (i.e. 31.2, 27.9 and 25.9 kJ mol^{-1} , respectively). Suffice it to add that the corresponding (harmonic) ZPE contribution is about -4.2 kJ mol^{-1} at the CAS(8,12)/AVTZ level which, in turn, reduces the corresponding energy differences even further. As noted by Massó *et al.* [38], such energetic proximity ($\approx 4.9 \text{ kJ mol}^{-1}$) between the $l\text{-}\text{C}_4(^3\Sigma_g^-)$ and $r\text{-}\text{C}_4(^1A_g)$ isomers is expected to be of the same order of accuracy of the *ab initio* calculations themselves, and hence any statement about the true ground state of C_4 is possibly risky at present.

Unquestionably, the triplet ground state is the $^3\Sigma_g^-$ structure. Its cumulenic nature is evidenced by the nearly equal C=C bond lengths which are predicted from our FVCAS/AVTZ calculations to be 2.506 and $2.463 a_0$ for the outer ($R_1 = R_3$) and inner (R_2) distances, respectively. Such values agree well with the experimental (averaged) bond length of $2.458 a_0$ [2]. As first remarked by Parasuk & Alm  f [37], the corresponding acetylenic form is of $^3\Sigma_u^+$ symmetry and lies well above in energy ($\approx 107.6 \text{ kJ mol}^{-1}$). This state of C_4 has characteristic bond distances of an acetylenic-like molecule, i.e. the outer C=C bonds are about $0.3 a_0$ shorter than the inner R_1

Table 7. Structural parameters (distances R_i in a_0 , angles in degrees) and vibrational frequencies (in cm^{-1}) of the stationary points on the ground-state singlet PES of C_4 . Energies (in kJ mol^{-1}) relative to $I-\text{C}_4(^3\Sigma_g^-)$. (Online version in colour.)

feature/method					
	$r\text{-C}_4(^1\text{A}_g)$	$d\text{-C}_4(^1\text{A}')$	$dl\text{-C}_4(^1\text{A}')$	$I\text{-C}_4(^1\Delta_g)$	$dd\text{-C}_4(^1\text{A}_1)$
	D_{2h}	C_s	C_s	$D_{\infty h}$	C_{2v}
CAS(8,12)/AVTZ ^a	29.8	127.0	156.8	27.5	130.2
FVCAS/AVTZ ^a	12.7	124.4	158.2	32.0	126.5
CASDC/CBS-8 ^a	25.9	137.6	168.3	38.7	138.8
ve-CASDC/CBS ^a	9.1	131.3	168.5	34.8	133.5
R_1^b	2.725(2.758) ^c	2.616	2.507	2.467(2.509) ^c	2.655(2.643) ^c
R_2	2.725(2.758) ^c	2.938	2.583	2.457(2.484) ^c	2.785(2.778) ^c
R_3	2.725(2.758) ^c	2.496	2.488	2.467(2.509) ^c	2.480(2.556) ^c
α	115.9(116.7) ^c	56.6	91.7	180.0(180.0) ^c	61.5(61.6) ^c
β	64.4(63.3) ^c	130.8	179.5	180.0(180.0) ^c	151.5(151.6) ^c
w_1^b	1271.9	1643.0	1796.3	2021.8	1739.8
w_2	964.1	1296.1	1561.1	936.5	1269.6
w_3	983.3	902.6	1103.7	1643.0	818.1
w_4	406.3	689.3	1065.6	406.4/375.2	628.7
w_5	514.2	287.5	284.8	209.6/194.1	257.2
w_6	1445.0	211.8	475.5 <i>i</i>		238.0 <i>i</i>

^aThis work.

^bObtained at CAS(8,12)/AVTZ level of theory.

^cFVCAS/AVTZ optimized values.

distance [37]. It should be noted that, at linear geometries, two low-lying $^1\Delta_g$ and $^1\Sigma_g^+$ excited states also arise from the π_g^2 configuration (figure 12a). These have been measured in anion photoelectron spectra [148] to be about 32.0 and 48.2 kJ mol^{-1} , respectively, above the $^3\Sigma_g^-$ state. The corresponding adiabatic excitation energies predicted from our ve-CASDC/CBS calculations are 34.8 and 50.2 kJ mol^{-1} , respectively.

Figure 11 shows that the ground singlet is the rhombic $^1\text{A}_g$ structure, thence an a_g^2 electronic configuration (figure 12b). At the FVCAS/AVTZ level of theory, this molecule shows characteristic peripheral and cross-ring C–C bond lengths of 2.758 and 2.895 a_0 , respectively. Such quantities agree nicely with the most recent *ab initio* values of 2.739 and 2.855 a_0 reported by Wang *et al.* [141] at the CCSD(T)-F12b/AVTZ level of theory as well as those obtained from ve-MRCI(Q)/VTZ calculations by Senent *et al.* [140] (2.742 and 2.873 a_0). Actually, as seen in tables 6 and 7, all stationary structures optimized at the CAS(8,12)/AVTZ level differ by less than $\approx 0.05a_0$ and $\approx 1^\circ$ for bond lengths and bond angles, from those obtained when all valence electrons are included in the ndc treatment. This situation clearly reflects the general observation that geometries are often less sensitive to the theoretical level than relative energies [176,177].

Figure 11 further depicts an additional (local) minimum on the lowest triplet PES of C_4 , namely $r\text{-C}_4(^3B_{2g})$. At the CASDC/CBS-8 level, such a structure lies about 261.0 kJ mol^{-1} higher in energy relative to the $^3\Sigma_g^-$ isomer and is located well above the corresponding $^1\text{A}_g$ rhombic partner

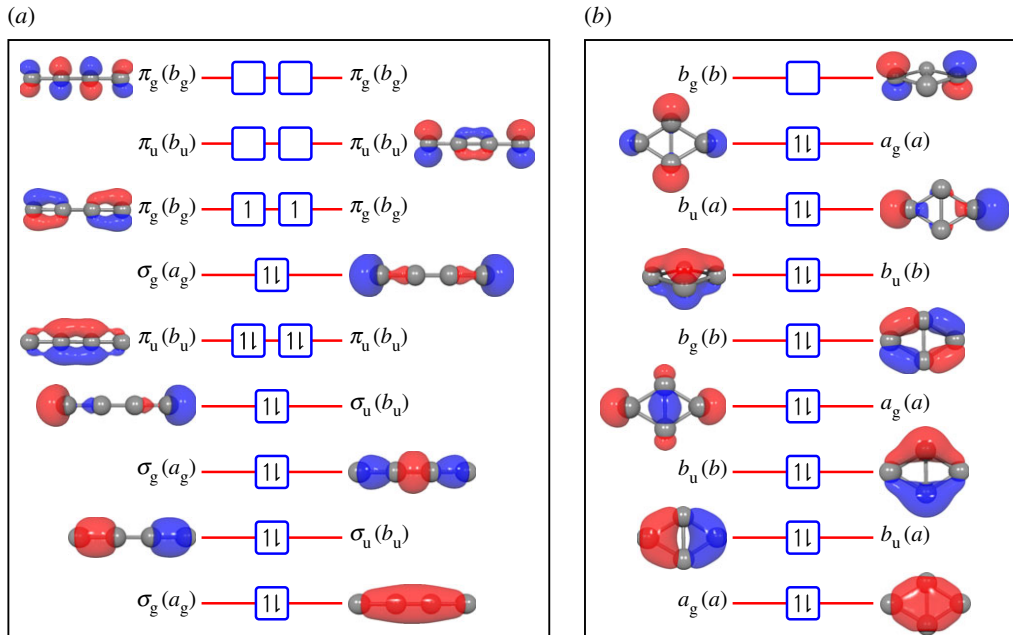


Figure 12. Molecular orbital diagrams and valence electronic configurations for (a) *l*-C₄(³ Σ_g^-) and (b) *r*-C₄(¹ A_g). Molecular orbitals are labelled according to $D_{\infty h}$ and D_{2h} irreps, respectively, with the corresponding correlations with D_{2h} and C_{2v} point groups given in parentheses. Up and down arrows denote α and β spin states, respectively. Natural orbitals obtained from FVCAS/AVTZ wave functions are also depicted. (Online version in colour.)

(tables 6 and 7). Note that although the optimized structures predicted from the CAS(8,12)/AVTZ calculations are in excellent agreement with those obtained at the FVCAS/AVTZ level, the inclusion of all valence space in the ndc treatment reduces the energy difference between *l*-C₄(³ Σ_g^-) and *r*-C₄(³ B_{2g}) by about 115.4 kJ mol⁻¹. In fact, at the ve-CASDC/CBS level, these latter forms are separated by 145.6 kJ mol⁻¹. Note that the energy splitting between the ³ B_{2g} and ¹ A_g rhombic structures is predicted to be 136.5 kJ mol⁻¹ at this level. Such a result is in reasonable agreement with the corresponding vertical excitation energy of 187.2 kJ mol⁻¹ reported by Massó *et al.* [38] at the ve-MRCI(Q)/VTZ level. As emphasized by the authors, their value would be decreased if one considers the relaxation of all nuclear coordinates.

The isomerization of *l*-C₄(³ Σ_g^-) into *r*-C₄(³ B_{2g}) structure occurs via a C_s transition state *lr*-C₄(³ A'') (figures 11 and 13). At the CASDC/CBS-8 level, the latter is about 262.4 kJ mol⁻¹ above the corresponding linear minimum. The full valence ndc treatment reduces that value by about 108.3 kJ mol⁻¹. Indeed, the classical barrier height predicted from our ve-CASDC/CBS protocol is 154.1 kJ mol⁻¹. The corresponding ORC path for such an isomerization reaction is depicted in figure 13. For this we performed CAS(8,12)/AVTZ constrained optimizations in which a single peripheral bond length of the *r*-C₄(³ B_{2g}) structure (*R*) is treated as inactive, with all other degrees freedom (two bond lengths and two bond angles) optimized at each grid point. Single-point MRCI(Q)-8/AVXT (X = T, Q) calculations along the optimized CAS(8,12)/AVTZ path have subsequently been performed, followed by extrapolations to the CASDC/CBS-8 limit. To check the proper convergence of the CAS wave function, all ORCs have been performed in both ‘forward’ and ‘backward’ directions. Unfortunately, at FVCAS/AVXZ level, such paths are unaffordable with the means at our disposal, and hence not pursued. However, as emphasized in §4b, an alternative approach can be employed that brings MRCI(Q)-8/AVTZ energies in close agreement with the predicted linear–rhombic energy splittings at ve-CASDC/CBS.

Figure 13 shows that, although the predicted potential barriers increase by 21.0, 28.3 and 33.5 kJ mol⁻¹ with the MRCI(Q)-8/AVTZ, MRCI(Q)-8/AVQZ and CASDC/CBS-8 correlation

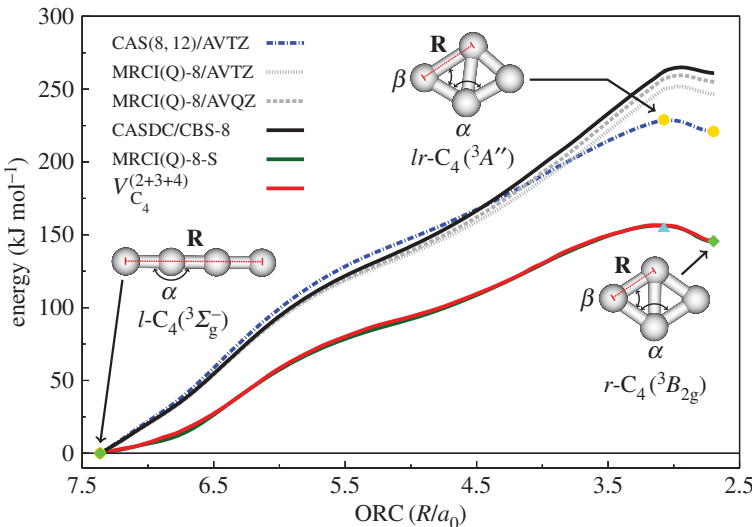


Figure 13. ORC paths for interconversion of $l\text{-C}_4(^3\Sigma_g^-)$ and $r\text{-C}_4(^3B_{2g})$ via $lr\text{-C}_4(^3A'')$ transition state. The inactive coordinate corresponds to the peripheral bond length of the $r\text{-C}_4(^3B_{2g})$ structure (R), with all other degrees of freedom optimized at each grid point. Stationary structures at the CAS(8,12)/AVTZ, ve-CASDC/CBS and ve-CASDC/CBS/CAS(8,12)/AVTZ levels are shown by dots, diamonds and triangles, respectively. Energies are relative to $l\text{-C}_4(^3\Sigma_g^-)$. The MRCI(Q)-8-S and $V_{\text{C}_4}^{(2+3+4)}$ curves are discussed in §4b. (Online version in colour.)

treatments, respectively, the structure of the transition state differs only slightly from the CAS(8,12)/AVTZ one. Overall, the addition of dynamical correlation shifts the location of $lr\text{-C}_4(^3A'')$ TS towards the rhombic isomer. Suffice to highlight that, although only a single peripheral bond has been followed in the ORC path, the above isomerization process clearly involves the formation/breaking of both peripheral and cross-ring bonds.

To the best of our knowledge, the only *ab initio* study on such a reaction path for C_4 is that of Blanksby *et al.* [138]. The authors used CCSD(T)/AVDZ//B3LYP/6-31G* to report a value of $108.1 \text{ kJ mol}^{-1}$ for the isomerization barrier of $l\text{-C}_4(^3\Sigma_g^-)$ into $r\text{-C}_4(^3B_{2g})$. Suffice to add that the rhombic 1A_g structure is 11.7 kJ mol^{-1} more stable than $l\text{-C}_4(^3\Sigma_g^-)$ at their level of theory [138].

In contrast to the triplet ground-state surface, the isomerization between rhombic and linear forms on the singlet PES occurs in a stepwise manner (figures 11 and 14). Starting from the 1A_g global minimum, the system attains an intermediate C_s monocyclic ring [$d\text{-C}_4(^1A')$] via a ring-opening (barrierless) process in which only a single peripheral bond is broken. Indeed, $d\text{-C}_4(^1A')$ shows itself as a local minimum on the singlet ground-state PES and lies about 111.7 and $122.2 \text{ kJ mol}^{-1}$ above the $r\text{-C}_4(^1A_g)$ structure at the CASDC/CBS-8 and ve-CASDC/CBS levels of theory, respectively. As we shall see, the discrepancies between full-valence and truncated-space correlation approaches are generally smaller for the singlet than the triplet states. This stems from a higher multi-configurational character of the latter [141]. In fact, because the isomerization process in the singlet PES occurs in a stepwise manner, reactants and products are somewhat similar in nature, thus allowing for some error compensation in the *ab initio* calculations.

The ORC path for interconversion of $r\text{-C}_4(^1A_g)$ and $d\text{-C}_4(^1A')$ is depicted in figure 14a. The salient feature relates to the appearance of a small barrier at $\alpha = 151.5^\circ$ in the CAS(8,12)/AVTZ optimized curve. Indeed, such a geometry corresponds to a C_{2v} capped triangle ($dd\text{-C}_4(^1A_1)$ in table 7) which was first identified by Whiteside *et al.* [129]. At the CAS(8,12)/AVTZ level, this form represents a transition state with an imaginary frequency of only 238.0 cm^{-1} . A close inspection of figure 14a reveals that $dd\text{-C}_4(^1A_1)$ is responsible for the degenerate isomerization between symmetrically equivalent $d\text{-C}_4(^1A')$ structures (one with $\alpha = 130.8^\circ$, the other $\alpha = 173.6^\circ$). The isomerization barrier is only 3.2 kJ mol^{-1} at this level. However, as first noted by Massó *et al.*

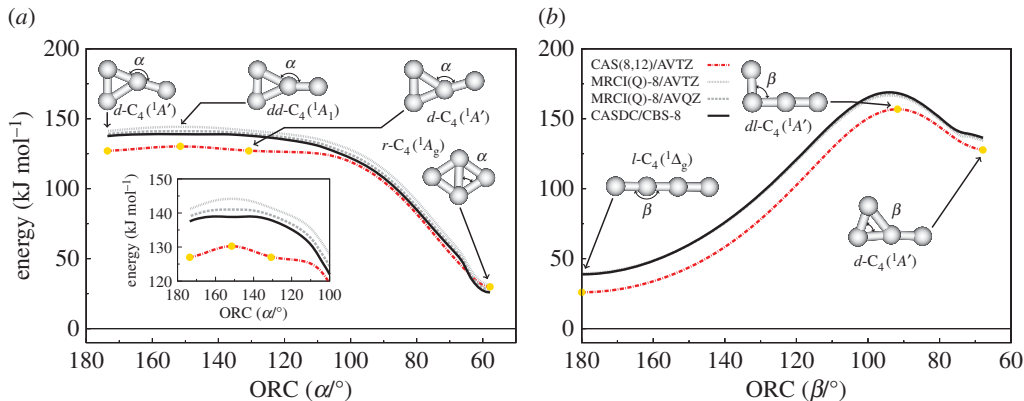


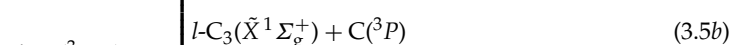
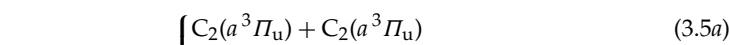
Figure 14. ORC paths for the $r\text{-C}_4(^1\text{A}_g)$ and $l\text{-C}_4(^1\Delta_g)$ isomerization. (a) Interconversion of $r\text{-C}_4(^1\text{A}_g)$ and $d\text{-C}_4(^1\text{A}')$. The inactive coordinate corresponds to the angle formed between peripheral and cross-ring bond lengths (α). (b) Interconversion of $d\text{-C}_4(^1\text{A}')$ and $l\text{-C}_4(^1\Delta_g)$ via the $dl\text{-C}_4(^1\text{A}')$ transition state. The inactive coordinate corresponds to the ring-opening angle β . Stationary structures at the CAS(8,12)/AVTZ level are indicated by solid dots. Energies are relative to $l\text{-C}_4(^3\Sigma_g^-)$. (Online version in colour.)

[38] and clearly seen in figure 14a, extrapolations to the CBS limit make the appearance of a very shallow minimum at such a geometry. At the CASDC/CBS-8 and ve-CASDC/CBS levels of theory, $dd\text{-C}_4(^1\text{A}_1)$ is found to be 112.9 and 124.4 kJ mol⁻¹ higher in energy than the singlet rhombus, respectively. Note from figure 14a that if one increases α up to about 244.1°, a symmetry-equivalent conformer of $r\text{-C}_4(^1\text{A}_g)$ (in which the cross-ring bond is converted to peripheral and vice versa) is obtained. Suffice to say that Blanksby *et al.* predicted a CCSD(T)/AVDZ//B3LYP/6-31G* transition state of C_s symmetry for interconversion of $r\text{-C}_4(^1\text{A}_g)$ and $d\text{-C}_4(^1\text{A}')$ but, surprisingly, lying below the latter. In our preliminary CAS(8,12)/AVTZ geometry searches, a similar transition state has been found but the IRC revealed discontinuities. Such an unphysical behaviour is removed using the ORC method.

The ultimate path in the isomerization process consists of converting $d\text{-C}_4(^1\text{A}')$ into the more stable $l\text{-C}_4(^1\Delta_g)$ form. As figure 14b shows, this is the rate-determining step, which occurs via an L-type transition structure $dl\text{-C}_4(^1\text{A}')$ with a ve-CASDC/CBS barrier height of about 37.2 kJ mol⁻¹ relative to $d\text{-C}_4(^1\text{A}')$. This compares with the value 58.6 kJ mol⁻¹ predicted by Blanksby *et al.* A final remark goes to work by Ngandjong *et al.* [183] who studied the above cyclization pathway for singlet C₄ at the M06-2X/AVDZ level of theory. The authors suggested a one-step isomerization process where $r\text{-C}_4(^1\text{A}_g)$ is directly attained from $l\text{-C}_4(^1\Delta_g)$ via a C_s transition structure similar to $dl\text{-C}_4(^1\text{A}')$. Clearly, their result differs dramatically from our own MR result. In fact, as noted by the authors themselves, the use of DFT on electronic structure calculations of carbon clusters can be notoriously complicated due to their intrinsic multistate character [183].

(b) A novel DMBE for triplet C₄

Following the Wigner–Witmer rules [156,157], one has



Likewise $C_3(\tilde{X}^1\Sigma_g^+)$ [35,105,106,119], the title species does not correlate to ground-state C₂ fragments, with the asymptote (3.5a) lying [51] 17.2 kJ mol⁻¹ above the $C_2(X^1\Sigma_g^+) + C_2(X^1\Sigma_g^+)$

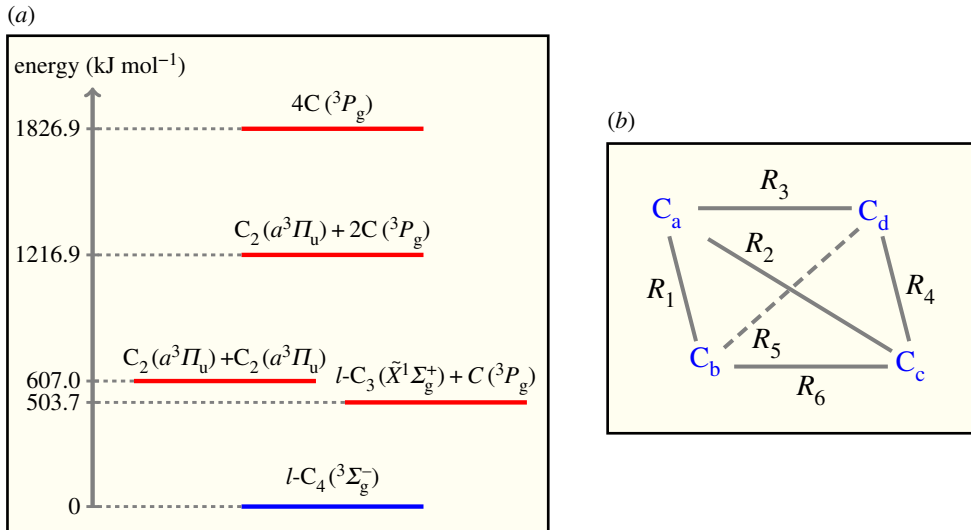


Figure 15. (a) Energetics of the various asymptotic channels of *l*-C₄(³ Σ_g^-) shown in equation (3.5). The atomization energy (at 0 K) for C₄ is taken from [42] with the zero-point vibrational energy retrieved from [184]. The corresponding experimental data for C₃($\tilde{X}^1\Sigma_g^+$) and C₂(^a $^3\Pi_u$) are from [35]. (b) Inter-particle coordinate system employed in the construction of the DMBE-(2 + 3) and DMBE-(2 + 3 + 4) PESs. (Online version in colour.)

spin-forbidden channel. As noted by Ritchie *et al.* [131], this latter correlates with the excited *l*-C₄(¹ Σ_g^+) form. Figure 15a shows that the dissociation process into C₂(^a $^3\Pi_u$) occurs with an endothermicity of about 607.0 kJ mol⁻¹. In turn, the dissociation into unlike species gives both C₃ and C fragments into their ground electronic states. As noted by Wakelam *et al.* [9], such a collinear reaction is the lowest path yielding *l*-C₄(³ Σ_g^-), which according to figure 15a is exothermic by about 503.7 kJ mol⁻¹. Note that the first excited asymptotic channel C₃($\tilde{a}^3\Pi_u$) + C(³ P) lies [86,88] 202.8 kJ mol⁻¹ above the asymptote (3.5b) and correlates with higher excited electronic states such as *l*-C₄(³ Π_u) [9] and *l*-C₄(¹ Σ_g^+). Suffice to say that the exit channels (3.5c) and (3.5d) arise from the dissociation of C₃($\tilde{X}^1\Sigma_g^+$) (in channel (3.5b)) into C₂(^a $^3\Pi_u$) + C(³ P), with subsequent fragmentation into C(³ P) + C(³ P) [35].

Among the most reliable approaches to obtain a realistic representation of a global PES, the MBE [119,120] and DMBE [123–125] methods play a prominent role and have acquired popularity. Accordingly, the PES of a molecular system is expanded in sub-clusters of atoms [119], thus warranting by built-in construction the correct asymptotic behaviour in any fragmentation. Indeed, once the potentials of all fragments have been obtained, the key MBE development enables a first estimate of the PES for the target polyatomic [119,120]. One should bear in mind that even if the series converges rapidly, chemical accuracy is only attainable by including the highest-order (i.e. beyond pairwise additivity) possible contributions [119,125]. As the potentials of C₃($\tilde{X}^1\Sigma_g^+$) and C₂(^a $^3\Pi_u$) are already known (§3d), one can proceed to the *a priori* estimate of the C₄ triplet PES.

Following the DMBE method [123–125] and equation (3.5), the approximate cluster expansion for the title species including two- and three-body contributions only assumes the form

$$\begin{aligned}
 V_{\text{C}_4}^{(2+3)}(\mathbf{R}) = & V_{\text{C}_a\text{C}_b}^{(2)}(R_1) + V_{\text{C}_a\text{C}_c}^{(2)}(R_2) + V_{\text{C}_a\text{C}_d}^{(2)}(R_3) + V_{\text{C}_b\text{C}_d}^{(2)}(R_4) + V_{\text{C}_b\text{C}_c}^{(2)}(R_5) \\
 & + V_{\text{C}_b\text{C}_c}^{(2)}(R_6) + V_{\text{C}_a\text{C}_b\text{C}_c}^{(3)}(R_1, R_2, R_6) + V_{\text{C}_a\text{C}_c\text{C}_d}^{(3)}(R_2, R_3, R_4) \\
 & + V_{\text{C}_a\text{C}_b\text{C}_d}^{(3)}(R_1, R_3, R_5) + V_{\text{C}_b\text{C}_c\text{C}_d}^{(3)}(R_4, R_5, R_6),
 \end{aligned} \tag{3.6}$$

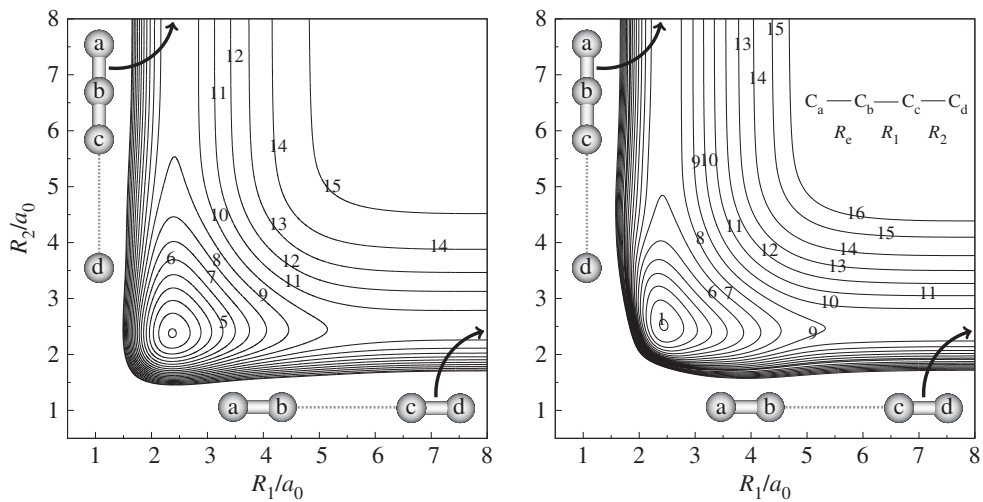


Figure 16. Partially relaxed ($2.2 \leq R_e/a_0 \leq 2.6$) contour plot for $C_{\infty v}$ insertion of a C atom into a C_3 triatomic molecule. (a) DMBe/ES/SS-(2 + 3) PES. (b) DMBe/ES/SS-(2 + 3 + 4) PES. Contours in panel (a) are equally spaced by $0.03 E_h$, starting at $-0.8370 E_h$. In (b), they are $0.03 E_h$, and $-0.7127 E_h$ in the same order.

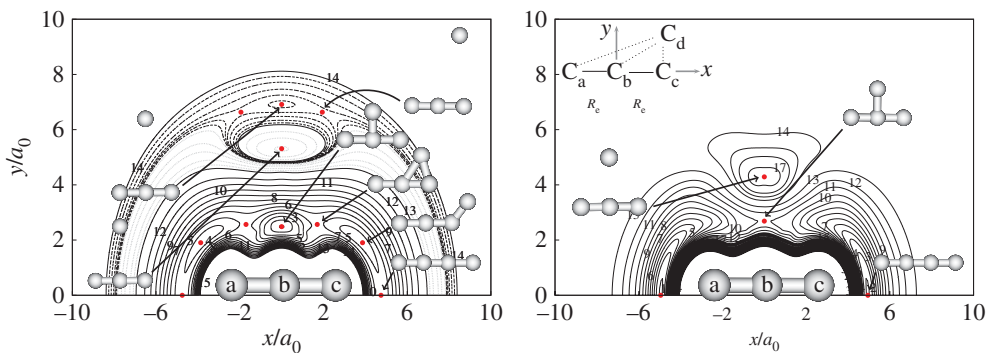


Figure 17. As in figure 16, but for a partially relaxed ($2.2 \leq R_e/a_0 \leq 2.6$) contour plot for the C atom moving around C_3 which lies along the x-axis with the origin fixed at the central carbon atom. Solid black lines are in panel (a) equally spaced by $0.01 E_h$, starting at $-0.8864 E_h$. In panel (b), the corresponding values are $0.015 E_h$ and $-0.7127 E_h$. Dotted grey and dashed black lines are equally spaced by 0.005 and $0.0002 E_h$, starting at -0.5624 and $-0.5326 E_h$, respectively. (Online version in colour.)

where $\mathbf{R} = \{R_1, R_2, R_3, R_4, R_5, R_6\}$ is a collective variable of the inter-particle distances in figure 15b. As usual [123–125], each n -body term is split into EHF and dc energy contributions [35,116]: $V^{(n)} = V_{\text{EHF}}^{(n)} + V_{\text{dc}}^{(n)}$. Note that all fragments dissociate into ground-state C atoms, and hence there is no need for one-body terms; the zero of energy is the exit channel (3.5d). Because the DMBe/ES/SS [117] form of C_3 is used here to obtain such an approximate potential, the C_4 PES will be denoted as DMBe/ES/SS-(2 + 3). The required three-body terms have been obtained by subtracting the sum of two bodies from the total energy,

$$V_{C_3}^{(3)}(R_i, R_j, R_k) = V_{\text{ES}}(R_i, R_j, R_k) - [V_{C_2}^{(2)}(R_i) + V_{C_2}^{(2)}(R_j) + V_{C_2}^{(2)}(R_k)]. \quad (3.7)$$

Similar topographical features are obtained when using any other of our functions. Figures 16a and 17a show relevant aspects of the purely *ab initio*-based DMBe/ES/SS-(2 + 3) expansion.

Table 8. Integrity basis used for the representation of the triplet C₄ PES.

$\Gamma_1 = Q_1$	$\Gamma_4 = Q_2 Q_3 Q_4$
$\Gamma_2 = Q_2^2 + Q_3^2 + Q_4^2$	$\Gamma_5 = Q_6^3 - 3Q_6 Q_5^2$
$\Gamma_3 = Q_5^2 + Q_6^2$	$\Gamma_6 = Q_6(2Q_2^2 - Q_3^2 - Q_4^2) + \sqrt{3}Q_5(Q_3^2 - Q_4^2)$

As expected, the DMBE/ES/SS-(2 + 3) PES provides a realistic representation of the potential both in the valence and long-range interaction regions. In fact, as figures 16a and 17a show, the current DMBE has the correct asymptotic behaviour, which is a well-established asset of MBE theory [119,123–125]. It should be stressed that although the truncated potentials give a good representation of the triplet linear global minimum, l-C₄(³Σ_g⁻) is predicted to be a saddle point of index 4, with imaginary frequencies corresponding to the degenerate trans-(w₄) and cis-bending (w₅) modes. This result stems largely from the lack of the four-body term which, according to figure 15a and the DMBE/ES/SS-(2 + 3) PES, is estimated to be as repulsive as 376 kJ mol⁻¹ at this geometry. Similar magnitudes of four-body interaction energies have been reported for X₄-type elemental clusters such as H₄ [120,185] and O₄ [186]. In fact, for ground-state C₃, the three-body energy is known [35,116,185] to strongly favour the linear structure: it is attractive in this region, but repulsive (or less attractive) as the molecule bends, in such a way as to counteract the increased attraction of the two-body terms. Thus, at D_{3h} geometries, a minimum of the latter is accompanied by a maximum in energy of the former. Ongoing from C₃ to C₄, the two-body terms are doubled in number, while the three-body terms are quadrupled. If the four-body energy is ignored *a priori*, one expects, therefore, an over-stabilization of the linear structure due to the three-body terms, with highly symmetric geometries such as T_d forms being greatly destabilized. Obviously, there are cases in which the gain in two-body energy on passing from chains to rings will compensate for the loss of three-body interaction so that cyclic structures can be almost isoenergetic or even more stable than l-C₄(³Σ_g⁻). However, such forms are predicted from our *ab initio* calculations to be high-lying stationary structures on the triplet ground-state PES. This is mostly attributed to the generally repulsive nature of the four-body term: although this contributes significantly to the total energy, it is a well-accepted trend that the two- and three-body terms are predominantly structure determining in elemental clusters [119,120,185,186].

In an attempt to improve the above PES, an approximate four-body term has been added to the DMBE/ES/SS-(2 + 3) potential in equation (3.6). For this, we employed a distributed Gaussian approach [187,188] in which sets of correcting locally valid functions are centred at convenient geometries; see also Ref. [189] for the original *n*-body distributed polynomial method. The effective four-body term is then written as

$$V_{C_4}^{(4)}(\mathbf{R}) = \sum_{i=1}^7 P_i^{(4)}(\boldsymbol{\Gamma}) G_i(\boldsymbol{\Gamma}), \quad (3.8)$$

where $P_i^{(4)}(\boldsymbol{\Gamma})$ are cubic polynomials of the form

$$\begin{aligned} P_i^{(4)}(\boldsymbol{\Gamma}) = & (c_0 + c_1 \Gamma_1 + c_2 \Gamma_1^2 + c_3 \Gamma_2 + c_4 \Gamma_3 + c_5 \Gamma_1^3 + c_6 \Gamma_1 \Gamma_2 \\ & + c_7 \Gamma_1 \Gamma_3 + c_8 \Gamma_4 + c_9 \Gamma_5 + c_{10} \Gamma_6), \end{aligned} \quad (3.9)$$

and $G_i(\boldsymbol{\Gamma}) = \exp[-\gamma_i(\Gamma_1)^2]$ are Gaussian factors that quickly die off away from the origin point. Following Varandas and co-workers [119,169,186], Γ_i ($i = 1 - 6$) are totally symmetric combinations of the Q_i ($i = 1 - 6$) coordinates (table 8), which are written as symmetrized

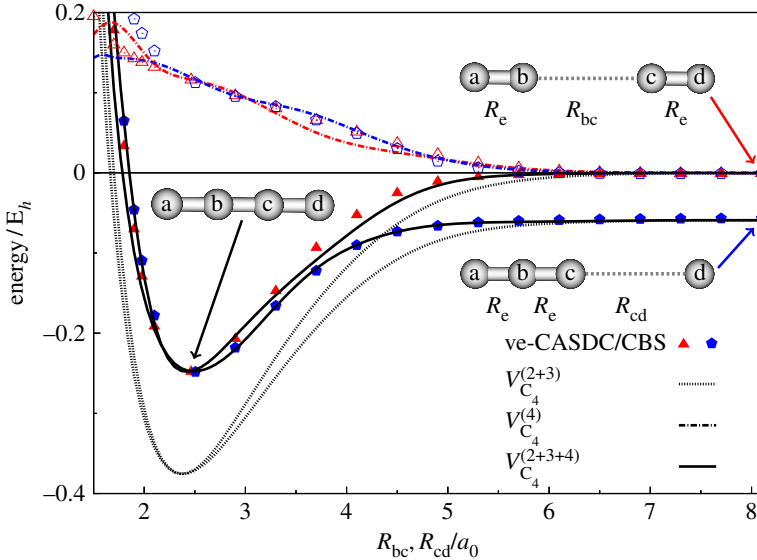


Figure 18. Relaxed 1D cuts for dissociation of $l\text{-C}_4(^3\Sigma_g^-)$ into $\text{C}_2(^3\Pi_u) + \text{C}_2(^3\Pi_u)$ and $l\text{-C}_3(\tilde{\chi}^1\Sigma_g^+) + \text{C}(^3P)$ as obtained from DMBE/ES/SS-(2 + 3) and DMBE/ES/SS-(2 + 3 + 4). Also shown are the approximate four-body interaction energies obtained at the ve-CASDC/CBS level and the additional term $V_{\text{C}_4}^{(4)}(\mathbf{R})$. (Online version in colour.)

displacements from a T_d geometry of side R_0 [119,169,186]

$$\begin{pmatrix} Q_1 \\ Q_2 \\ Q_3 \\ Q_4 \\ Q_5 \\ Q_6 \end{pmatrix} = \begin{pmatrix} \sqrt{\frac{1}{6}} & \sqrt{\frac{1}{6}} & \sqrt{\frac{1}{6}} & \sqrt{\frac{1}{6}} & \sqrt{\frac{1}{6}} & \sqrt{\frac{1}{6}} \\ \sqrt{\frac{1}{2}} & 0 & 0 & -\sqrt{\frac{1}{2}} & 0 & 0 \\ 0 & \sqrt{\frac{1}{2}} & 0 & 0 & -\sqrt{\frac{1}{2}} & 0 \\ 0 & 0 & \sqrt{\frac{1}{2}} & 0 & 0 & -\sqrt{\frac{1}{2}} \\ 0 & \frac{1}{2} & -\frac{1}{2} & 0 & \frac{1}{2} & -\frac{1}{2} \\ \sqrt{\frac{1}{3}} & -\sqrt{\frac{1}{12}} & -\sqrt{\frac{1}{12}} & \sqrt{\frac{1}{3}} & -\sqrt{\frac{1}{12}} & -\sqrt{\frac{1}{12}} \end{pmatrix} \begin{pmatrix} \Delta R_1 \\ \Delta R_2 \\ \Delta R_3 \\ \Delta R_4 \\ \Delta R_5 \\ \Delta R_6 \end{pmatrix}, \quad (3.10)$$

where $\Delta R_i = R_i - R_0$. Thus, using symmetry labels of the T_d point group, $(Q_1, (Q_2, Q_3, Q_4))$ and (Q_5, Q_6) transform as A_1, T_2 and E irreps, respectively. To calibrate equation (3.8), a total of 663 *ab initio* points have been employed as follows. First, a set of 53 (constrained) optimized geometries for collinear approximations of the $\text{C}_3 + \text{C}$ and $\text{C}_2 + \text{C}_2$ fragments has been obtained at the ve-CASDC/CBS level using C_{2v} and D_{2h} symmetries, respectively (figure 18). The corresponding four-body interaction energies have then been determined from the requirement that they vanish at all dissociation limits (assumed as $R_{bc} = R_{cd} = 10.0a_0$) and by further subtracting the energies predicted from DMBE/ES/SS-(2 + 3). An additional set of 76 nuclear arrangements related to the ORC path shown in figure 13 has also been included. To give them ve-CASDC/CBS quality, we have scaled the corresponding MRCI(Q)-8/AVTZ energies in such a way as to reproduce the correct splitting between the $l\text{-C}_4(^3\Sigma_g^-)$ and $r\text{-C}_4(^3B_2g)$ forms at the ve-CASDC/CBS level, i.e. $\Delta E_{lr} = 0.0555 \text{ E}_h$ (see table 6). Such a factor has been determined with

$$\mathcal{F} = \frac{[E_3^{\text{MRCI}(Q)-8}(\mathbf{R}_r) - E_3^{\text{MRCI}(Q)-8}(\mathbf{R}_l)]}{\Delta E_{lr}}, \quad (3.11)$$

Table 9. Stratified RMSD (in kJ mol^{-1}) of the DMBE/ES/SS-(2 + 3 + 4) PES.

energy ^a	<i>N</i> ^b	RMSD	energy ^a	<i>N</i> ^b	RMSD
41	54	0.4	334	245	5.2
83	90	0.8	460	320	6.2
125	133	1.2	878	582	6.2
167	169	2.2	1297	616	8.1
209	182	2.3	2133	633	9.3
251	207	2.9	2552	640	10.2
292	221	3.1	6317	663	12.6

^aEnergy strata defined relative to the $l\text{-C}_4(^3\Sigma_g^-)$ structure.

^bNumber of calculated points up to the indicated energy range.

where $E_3^{\text{MRCI}(Q)-8}(\mathbf{R}_r)$ and $E_3^{\text{MRCI}(Q)-8}(\mathbf{R}_l)$ denote the MRCI(Q)-8/AVTZ absolute energies of the rhombic and linear isomers, yielding $\mathcal{F} = 1.7010$. From (3.11), the total interaction energy, with respect to $l\text{-C}_4(^3\Sigma_g^-)$, for any structure x can be expressed by

$$E(\mathbf{R}_x) = \frac{[E_3^{\text{MRCI}(Q)-8}(\mathbf{R}_x) - E_3^{\text{MRCI}(Q)-8}(\mathbf{R}_l)]}{\mathcal{F}} + E(\mathbf{R}_l), \quad (3.12)$$

where $E(\mathbf{R}_l) = -0.7127 E_h$ is the total interaction energy of the linear global minima (relative to the infinitely separated atoms) predicted from ve-CASDC/CBS calculations. Note that this is in excellent agreement with the experimental estimate of $-0.6958 E_h$ [35,42,184] (figure 15a). The ORC path obtained from equation (3.12) and denoted by MRCI(Q)-8-S is shown in figure 13. Clearly, the present approach brings MRCI(Q)-8/AVTZ energies in close agreement with the predicted linear-rhombic energy separations at ve-CASDC/CBS, while reasonably describing the region defined by the transition state $lr\text{-C}_4(^3A'')$.

With the aid of equation (3.12), an extra set of 534 *ab initio* points calculated at MRCI(Q)-8/AVTZ level has further been added in the least-squares fitting procedure. Note that the effective four-body energies have been determined simply by subtracting the total interaction energies predicted by equation (3.12) from the ones estimated with the DMBE/ES/SS-(2 + 3) form. Suffice to say that, differently from the set of linear coefficients (equation (3.9)) in which small initial guesses have been freely varied, the origin points (R_0) and range-decaying parameters (γ_i) of every Gaussian have been optimized by trial and error. Table 9 displays the stratified RMSD values of the final PES with respect to all fitted datasets. Thus, chemical accuracy is ensured up to approximately 334 kJ mol^{-1} above the absolute linear minima with larger deviations occurring for more repulsive energy strata. The optimum numerical coefficients of equation (3.8) are given as electronic supplementary material.

Figures 16b, 17b and 18–20 depict the most salient attributes of the full DMBE PES for triplet C_4 . As figure 18 shows, the approximate four-body interaction energy (equation (3.8)) mimics well the expensive set of calculated *ab initio* points at the ve-CASDC/CBS level of theory. Note that such a plot corresponds in figure 16b to orthogonal cuts taken along the R_2 and R_1 directions. As clearly seen from figure 18, the four-body term is as repulsive as $300.0 \text{ kJ mol}^{-1}$ (at ve-CASDC/CBS level) for such geometries. In fact, such a trend is further exacerbated as long as other regions of the nuclear configuration space are accessed. Yet, the simple addition of the $V_{\text{C}_4}^{(4)}(\mathbf{R})$ term makes the triplet linear structure, $l\text{-C}_4(^3\Sigma_g^-)$, to be a true minimum on the full PES with characteristic bond lengths $R_1 = R_3 = 2.524a_0$ and $R_2 = 2.435a_0$; such a feature can best be seen from figure 17. Moreover, the four-body term ensures that the DMBE form reproduces the correct endothermicities for dissociation into $\text{C}_2(a^3\Pi_u) + \text{C}_2(a^3\Pi_u)$

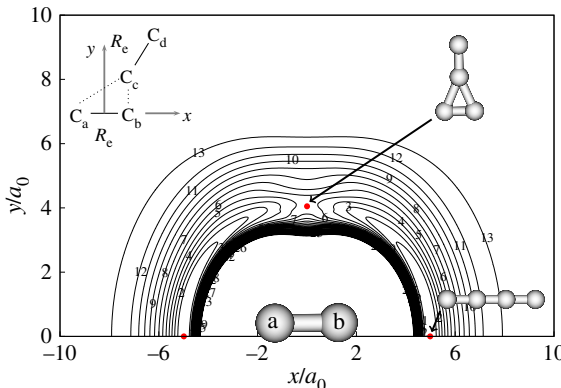


Figure 19. Partially relaxed contour plot ($2.2 \leq R_e/a_0 \leq 2.6$) of the DMBE/ES/SS-(2 + 3 + 4) PES for a C_2 fragment moving around another C_2 molecule which lies along the x -axis with the origin fixed at the centre of the $C-C$ bond length. Contours are equally spaced by 0.015 E_h , starting at -0.7127 E_h . (Online version in colour.)

and $l\text{-}C_3(\tilde{X}^1\Sigma_g^+)$ + $C(^3P)$, which are of about 647.8 and 504.0 kJ mol^{-1} , respectively. As shown in figure 15a, the corresponding experimental estimates are around 607.0 and 503.7 kJ mol^{-1} .

Besides accurately describing the region of the global minima, the DMBE/ES/SS-(2 + 3 + 4) form reproduces the minimum-energy interconversion pathway from $l\text{-}C_4(^3\Sigma_g^-)$ to $r\text{-}C_4(^3B_{2g})$ obtained at the MRCI(Q)-8-S level, as shown in figure 13. Yet, the triplet rhombic structure is described as a stable local minimum on the global PES (figure 20) with characteristic bond lengths and angles of $R_1 = R_2 = R_3 = 2.786\text{ a}_0$, $\alpha = 104.8^\circ$ and $\beta = 75.2^\circ$; see also table 6. The classical barrier height predicted for such a process is 155.2 kJ mol^{-1} relative to the linear minima.

Figure 17b illustrates the total PES for C moving around C_3 , and corresponds to plot (a) for DMBE/ES/SS-(2 + 3). As shown, the addition of the four-body term yields a simpler topography, in the sense of free from spurious extrema. Indeed, the T-shaped valence structure (at $x = 0.000\text{ a}_0$ and $y = 2.686\text{ a}_0$) appears in the full PES as a barrier-like feature connecting the two symmetry-equivalent $l\text{-}C_4(^3\Sigma_g^-)$ structures. However, this is not a true transition state on the six-dimensional configuration space, but a saddle point of index 3, in accordance with the MRCI(Q)-8/AVTZ calculations. Note that the additional T-shaped long-range structure (at $x = 0.000\text{ a}_0$ and $y = 4.290\text{ a}_0$) forms a high-symmetry D_{3h} triangle that could therefore evidence a C_i . Preliminary work at the CAS(8,12)/AVTZ level using the sign-reversal property of the wave function [167] has shown this not to be the case (at least for the ground triplet state) but revealed the presence of a high density of close-in-energy states at this region.

The in-plane attack of C_2 to another C_2 as obtained from DMBE/ES/SS-(2 + 3 + 4) is shown in figures 19 and 20. A notable feature from figure 19 refers to the barrier connecting the two adjacent linear isomers, which is now a true saddle point of index 1. This feature has been confirmed by *ab initio* MRCI(Q)-8/AVTZ and CCSD(T)/AVTZ calculations. Recall that Blanksby [138] and Ngandjong *et al.* [183] using DFT predicted such a structure to be a minimum. Also seen from figure 20 is the presence of two additional stationary points on the full PES: a slightly distorted C_{2v} capped triangle (at $x = 4.582\text{ a}_0$ and $y = 2.642\text{ a}_0$), and a *quasi*-rhombic form (at $x = 5.084\text{ a}_0$ and $y = 0.669\text{ a}_0$). Although such forms are predicted to be a minimum and transition state in 2D, this could not be confirmed here by *ab initio* calculations. Clearly, a true statement about their nature demands higher-level FVCAS/MRCI frequency calculations which are computationally unaffordable. Despite this, the chosen four-body term has been found reasonable at all investigated geometries. Of course, an enhanced fit may require an extended set of points for such geometries, and more complicated polynomial forms eventually involving all possible X_4 symmetry invariants. This is clearly a task outside the scope of the present work.

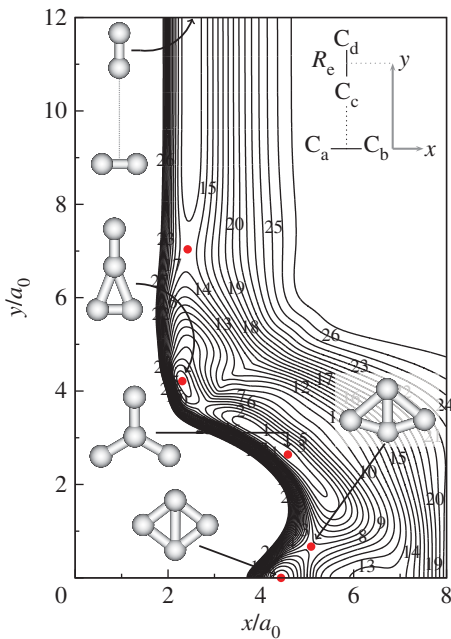


Figure 20. Partially relaxed contour plot ($2.4 \leq R_e/a_0 \leq 3.4$) for C_{2v} insertion of a C_2 fragment into another C_2 diatomic molecule as obtained from the DMBE/ES/SS-(2 + 3 + 4) PES. Contours are equally spaced by $0.015 E_h$, starting at $-0.6770 E_h$. (Online version in colour.)

4. Concluding remarks

A detailed analysis of the major features of the C_2 , C_3 and C_4 carbon clusters has been presented. For C_2 , we have briefly assessed its current status. Regarding C_3 , the most recent results obtained in our group were reviewed with emphasis on the PES which is particularly complicated due to multiple conical intersections. For C_4 , the most stable isomeric forms of both triplet and singlet PESs and their possible interconversion pathways were examined anew by means of accurate *ab initio* calculations. Based on such results, the strategy towards a global PES for triplet C_4 has also been discussed. Starting from a truncated cluster expansion of the molecular PES that uses our own functions for C_3 , an approximate four-body term has been suggested using 663 accurate *ab initio* energies. The resulting full 6D DMBE form reproduces all known topographical aspects of triplet C_4 as well as its linear-rhombic isomerization path: it is therefore commended for reaction dynamics studies. Clearly, the understanding of the electronic structure and properties of small carbon clusters provides valuable information on reactive collision processes where they may act as precursors to formation of larger clusters in the interstellar medium.

Data accessibility. The coefficients of the four-body term for the ground-state triplet PES of C_4 are available as electronic supplementary material.

Competing interests. We declare we have no competing interests.

Funding. This work is supported by Fundação para a Ciência e a Tecnologia and Coimbra Chemistry Centre, Portugal, through the project UI0313/QUI/2013, co-funded by FEDER/COMPETE 2020-EU.

Acknowledgements. C.M. thanks also the CAPES Foundation (Ministry of Education of Brazil) for a scholarship (Process BEX 0417/13-0).

Appendix A. The $(E + A_1) \otimes e$ vibronic Hamiltonian

Consider a X_3 -type molecule in a doubly degenerate electronic state E . Because no out-of-plane bending is possible, and the wave functions are symmetric with respect to reflection in the

molecular plane, the subgroup C_{3v} of D_{3h} may be used. Assume further that by solving the clamped-nuclei electronic Schrödinger equation (equation (2.8)), one obtains, besides the E term with component wave functions $|E_\theta(\mathbf{r}; \mathbf{0})\rangle$ and $|E_\epsilon(\mathbf{r}; \mathbf{0})\rangle$, a non-degenerate close-in-energy state $|A_1(\mathbf{r}; \mathbf{0})\rangle$. All such terms will then get vibronically mixed along the JT-active displacements with the vibronic problem becoming effectively a three-state one, thence a combined JT+PJT or $(E + A_1) \otimes e$. Clearly, we are assuming that the coupled states are well separated in energy from all others, and hence only their subspace needs consideration. Let now $\mathcal{E}_1(\mathbf{0}) = \mathcal{E}_2(\mathbf{0})$ and $\mathcal{E}_3(\mathbf{0})$ be the associated eigenvalues of the E and A_1 states, respectively. Let further the components of the normal E -type displacement be defined by $Q_{e_\epsilon} \equiv Q_2$ and $Q_{e_\theta} \equiv Q_3$, while $Q_{a_{1\ell}} \equiv Q_1$ is the totally symmetric mode that transforms according to the single line ℓ of the A_1 irrep.

The adiabatic PESs in the vicinity of \mathbf{Q}_0 are obtained by diagonalizing the electronic Hamiltonian operator matrix in the basis $\{|E_\theta(\mathbf{r}; \mathbf{0})\rangle, |E_\epsilon(\mathbf{r}; \mathbf{0})\rangle, |A_{1\ell}(\mathbf{r}; \mathbf{0})\rangle\}$. From equation (2.7), the associated matrix elements can be cast as (obvious coordinate dependencies are suppressed)

$$\begin{aligned} H_{ji} = & \mathcal{E}_j \delta_{ji} + \sum_{\bar{\Gamma}\bar{\gamma} \neq a_{1\ell}} F_{\bar{\Gamma}\bar{\gamma}}^{(\Gamma'\gamma'_j\Gamma\gamma_i)} Q_{\bar{\Gamma}\bar{\gamma}} + \sum_{\bar{\Gamma}\bar{\gamma} \neq a_{1\ell}} G_{\bar{\Gamma}\bar{\gamma}}^{(\Gamma'\gamma'_j\Gamma\gamma_i)} \{Q_{\bar{\Gamma}_1} \otimes Q_{\bar{\Gamma}_2}\}_{\bar{\Gamma}\bar{\gamma}} \\ & + \sum_{\bar{\Gamma}\bar{\gamma} = a_{1\ell}} \frac{1}{2} K_\Gamma \{Q_{\bar{\Gamma}_1} \otimes Q_{\bar{\Gamma}_2}\}_{\bar{\Gamma}\bar{\gamma}} \delta_{ji}, \end{aligned} \quad (\text{A } 1)$$

where $F_{\bar{\Gamma}\bar{\gamma}}^{(\Gamma'\gamma'_j\Gamma\gamma_i)}$ and $G_{\bar{\Gamma}\bar{\gamma}}^{(\Gamma'\gamma'_j\Gamma\gamma_i)}$ are linear and quadratic vibronic coupling constants which, from the Wigner–Eckart theorem, assume the form [158,161]

$$F_{\bar{\Gamma}\bar{\gamma}}^{(\Gamma'\gamma'_j\Gamma\gamma_i)} = \left\langle \Gamma'\gamma'_j \left| \left(\frac{\partial V}{\partial Q_{\bar{\Gamma}\bar{\gamma}}} \right)_0 \right| \Gamma\gamma_i \right\rangle = F_{\bar{\Gamma}}^{(\Gamma'\Gamma)} V \begin{pmatrix} \Gamma' & \Gamma & \bar{\Gamma} \\ \gamma'_j & \gamma_i & \bar{\gamma} \end{pmatrix} \quad (\text{A } 2)$$

and

$$G_{\bar{\Gamma}\bar{\gamma}}^{(\Gamma'\gamma'_j\Gamma\gamma_i)} = \frac{1}{2} \left\langle \Gamma'\gamma'_j \left| \left\{ \left(\frac{\partial^2 V}{\partial Q_{\bar{\Gamma}_1} \partial Q_{\bar{\Gamma}_2}} \right)_0 \right\}_{\bar{\Gamma}\bar{\gamma}} \right| \Gamma\gamma_i \right\rangle = \frac{1}{2} G_{\bar{\Gamma}}^{(\Gamma'\Gamma)} V \begin{pmatrix} \Gamma' & \Gamma & \bar{\Gamma} \\ \gamma'_j & \gamma_i & \bar{\gamma} \end{pmatrix}. \quad (\text{A } 3)$$

Thus, $F_{\bar{\Gamma}}^{(\Gamma'\Gamma)}$ and $G_{\bar{\Gamma}}^{(\Gamma'\Gamma)}$ are reduced matrix elements (do not depend on γ' , γ and $\bar{\gamma}$), while the last terms are V coefficients, which are symmetrized forms of the Clebsch–Gordan coefficients [158,161]. Such coefficients involving the E and A_1 terms of the symmetry point group C_{3v} are given in table 10. Note that all entries not shown are zero by symmetry considerations [161]. Note further that, following the rules of group theory (table 10), linear vibronic coupling constants between states of the same symmetry (diagonal elements, H_{jj}) are non-zero along the $Q_{a_{1\ell}}$ breathing mode: $F_{a_{1\ell}}^{(E_\epsilon E_\epsilon)}$, $F_{a_{1\ell}}^{(E_\theta E_\theta)}$ and $F_{a_{1\ell}}^{(A_1 A_1)}$. However, as the degeneracy of the E term is only lifted along JT-active displacements, they are assumed unimportant, and hence neglected in the summation of equation (A 1). Additionally, the diagonal quadratic coupling constants evaluated from totally symmetric irreducible products, $G_{a_{1\ell}}^{(E_\epsilon E_\epsilon)}$, $G_{a_{1\ell}}^{(E_\theta E_\theta)}$ and $G_{a_{1\ell}}^{(A_1 A_1)}$ are non-zero: they assume the physical meaning of (non-vibronic) force constants, K_Γ . For convenience, each term of equation (A 1) is considered *per se*:

$$H_{ji} = H_{ji}^{(0)} + W_{ji}^{(1)} + W_{ji}^{(2)} + K_{ji}, \quad (\text{A } 4)$$

where $H_{ji}^{(0)}$ and K_{ji} are elements of the zeroth-order and force constant (diagonal) matrices, and $W_{ji}^{(1)}$ and $W_{ji}^{(2)}$ contain linear (first-order) and quadratic (second-order) vibronic terms.

Table 10. V coefficients for the point group C_{3v} (subgroup of D_{3h}) calculated between twofold degenerate E and one-dimensional (totally symmetric) A_1 terms. All V which are not given are zero. Data taken from ref. [161].

			E	E	A_1	V	
			or				
			E	A_1	E	V	
			or				
E	E	E	V	A_1	E	V	
θ	θ	θ	$-\frac{1}{2}$	θ	θ	ι	$\frac{1}{\sqrt{2}}$
θ	ϵ	ϵ	$\frac{1}{2}$	ϵ	ϵ	ι	$\frac{1}{\sqrt{2}}$
ϵ	θ	ϵ	$\frac{1}{2}$	θ	ι	θ	$\frac{1}{\sqrt{2}}$
ϵ	ϵ	θ	$\frac{1}{2}$	ϵ	ι	ϵ	$\frac{1}{\sqrt{2}}$
				ι	θ	θ	$\frac{1}{\sqrt{2}}$
				ι	ϵ	ϵ	$\frac{1}{\sqrt{2}}$

All that remains is to determine the matrix elements of the set of sub-matrices (A 4). Consider the case of $W_{ji}^{(1)}$. Following equations (A 1), (A 2) and table 10, one gets

$$\begin{aligned} -W_{11}^{(1)} = W_{22}^{(1)} &= \left\langle E_\epsilon \left| \left(\frac{\partial V}{\partial Q_{e_\theta}} \right)_0 \right| E_\epsilon \right\rangle Q_{e_\theta} \\ &= \left\{ \bar{F}_E V \begin{pmatrix} E & E & e \\ \epsilon & \epsilon & \theta \end{pmatrix} \right\} Q_{e_\theta} = \left(\frac{1}{2} \bar{F}_E \right) Q_{e_\theta} = F_E Q_{e_\theta}, \end{aligned} \quad (\text{A } 5)$$

$$\begin{aligned} W_{12}^{(1)} = W_{21}^{(1)} &= \left\langle E_\epsilon \left| \left(\frac{\partial V}{\partial Q_{e_\epsilon}} \right)_0 \right| E_\theta \right\rangle Q_{e_\epsilon} \\ &= \left\{ \bar{F}_E V \begin{pmatrix} E & E & e \\ \epsilon & \theta & \epsilon \end{pmatrix} \right\} Q_{e_\epsilon} = \left(\frac{1}{2} \bar{F}_E \right) Q_{e_\epsilon} = F_E Q_{e_\epsilon}, \end{aligned} \quad (\text{A } 6)$$

$$\begin{aligned} W_{13}^{(1)} = W_{31}^{(1)} &= \left\langle A_{1\iota} \left| \left(\frac{\partial V}{\partial Q_{e_\theta}} \right)_0 \right| E_\theta \right\rangle Q_{e_\theta} \\ &= \left\{ \bar{H}_{E/A_1} V \begin{pmatrix} A_1 & E & e \\ \iota & \theta & \theta \end{pmatrix} \right\} Q_{e_\theta} = \left(\frac{1}{\sqrt{2}} \bar{H}_{E/A_1} \right) Q_{e_\theta} = H_{E/A_1} Q_{e_\theta} \end{aligned} \quad (\text{A } 7)$$

and

$$\begin{aligned} W_{23}^{(1)} = W_{32}^{(1)} &= \left\langle A_{1\iota} \left| \left(\frac{\partial V}{\partial Q_{e_\epsilon}} \right)_0 \right| E_\epsilon \right\rangle Q_{e_\epsilon} \\ &= \left\{ \bar{H}_{E/A_1} V \begin{pmatrix} A_1 & E & e \\ \iota & \epsilon & \epsilon \end{pmatrix} \right\} Q_{e_\epsilon} = \left(\frac{1}{\sqrt{2}} \bar{H}_{E/A_1} \right) Q_{e_\epsilon} = H_{E/A_1} Q_{e_\epsilon}, \end{aligned} \quad (\text{A } 8)$$

where F_E defines the linear JT vibronic coupling constant and \bar{F}_E is the reduced matrix element. For convenience, the linear PJT parameter has been denoted by H_{E/A_1} , and \bar{H}_{E/A_1} its corresponding reduced matrix element. As any vibronic perturbation associated with the breathing coordinate is neglected in the present JT+PJT problem, $W_{33}^{(1)} = 0$. Suffice to add that no other combinations of θ , ϵ and ι are possible in equations (A 5)–(A 8) due to having vanishing V coefficients.

The next step consists in obtaining corresponding expressions for $W_{ji}^{(2)}$ in equation (A 4). Following equations (A 1) and (A 3), and table 10, one has

$$\begin{aligned}
 -W_{11}^{(2)} &= W_{22}^{(2)} = \frac{1}{2} \left\langle E_\epsilon \left| \left\{ \left(\frac{\partial^2 V}{\partial Q_e \partial Q_e} \right)_0 \right\}_{e_\theta} \right| E_\epsilon \right\rangle \{Q_e \otimes Q_e\}_{e_\theta} \\
 &= \frac{1}{2} \left\langle E_\epsilon \left| \frac{\sqrt{2}}{2} \left\{ \left(\frac{\partial^2 V}{\partial Q_{e_\epsilon}^2} \right)_0 - \left(\frac{\partial^2 V}{\partial Q_{e_\theta}^2} \right)_0 \right\} \right| E_\epsilon \right\rangle \frac{\sqrt{2}}{2} (Q_{e_\epsilon}^2 - Q_{e_\theta}^2) \\
 &= \left\{ \frac{1}{4} \left\langle E_\epsilon \left| \left(\frac{\partial^2 V}{\partial Q_{e_\epsilon}^2} \right)_0 - \left(\frac{\partial^2 V}{\partial Q_{e_\theta}^2} \right)_0 \right| E_\epsilon \right\rangle \right\} (Q_{e_\epsilon}^2 - Q_{e_\theta}^2) \\
 &= \left\{ \frac{1}{4} \tilde{G}_E V \begin{pmatrix} E & E & e \\ \epsilon & \epsilon & \theta \end{pmatrix} \right\} (Q_{e_\epsilon}^2 - Q_{e_\theta}^2) \\
 &= \left(\frac{1}{8} \tilde{G}_E \right) (Q_{e_\epsilon}^2 - Q_{e_\theta}^2) = G_E (Q_{e_\epsilon}^2 - Q_{e_\theta}^2) \tag{A 9}
 \end{aligned}$$

and

$$\begin{aligned}
 W_{12}^{(2)} &= W_{21}^{(2)} = \frac{1}{2} \left\langle E_\epsilon \left| \left\{ \left(\frac{\partial^2 V}{\partial Q_e \partial Q_e} \right)_0 \right\}_{e_\epsilon} \right| E_\theta \right\rangle \{Q_e \otimes Q_e\}_{e_\epsilon} \\
 &= \frac{1}{2} \left\langle E_\epsilon \left| \sqrt{2} \left\{ \left(\frac{\partial^2 V}{\partial Q_{e_\theta} \partial Q_{e_\epsilon}} \right)_0 \right\} \right| E_\theta \right\rangle \frac{\sqrt{2}}{2} (Q_{e_\theta} Q_{e_\epsilon}) \\
 &= \left\{ \frac{1}{2} \left\langle E_\epsilon \left| \left(\frac{\partial^2 V}{\partial Q_{e_\theta} \partial Q_{e_\epsilon}} \right)_0 \right| E_\theta \right\rangle \right\} Q_{e_\theta} Q_{e_\epsilon} \\
 &= \left\{ \frac{1}{2} \tilde{G}_E V \begin{pmatrix} E & E & e \\ \epsilon & \theta & \epsilon \end{pmatrix} \right\} Q_{e_\theta} Q_{e_\epsilon} \\
 &= \left(\frac{1}{4} \tilde{G}_E \right) Q_{e_\theta} Q_{e_\epsilon} = 2G_E Q_{e_\theta} Q_{e_\epsilon}. \tag{A 10}
 \end{aligned}$$

In the above equations, G_E is the quadratic JT parameter and \tilde{G}_E the corresponding reduced matrix element. No other combinations of θ and ϵ are possible because $V=0$ (table 10). Recall that the explicit definition of the irreducible products in equations (A 9) and (A 10) is readily found by group-theoretic transformations, together with the Wigner–Eckart theorem (eqn (5.1) of [161]), and hence only the results are given. Because the non-adiabatic corrections due to PJT interaction are accounted up to first-order, the corresponding $W_{ji}^{(2)}$ block is identically zero, $W_{13}^{(2)} = W_{23}^{(2)} = W_{31}^{(2)} = W_{32}^{(2)} = 0$.

We define next the diagonal matrix elements K_{jj} (off-diagonal terms are zero by symmetry). The procedure is similar to the one used for $W_{ji}^{(2)}$, with the exception that totally symmetric irreducible products are employed. They read

$$\begin{aligned}
 K_{11} &= K_{22} = \kappa_E = \frac{1}{2} \left\langle E_\epsilon \left| \left\{ \left(\frac{\partial^2 V}{\partial Q_e \partial Q_e} \right)_0 \right\}_{a_{11}} \right| E_\epsilon \right\rangle \{Q_e \otimes Q_e\}_{a_{11}} \\
 &= \frac{1}{2} \left\langle E_\epsilon \left| \frac{1}{\sqrt{2}} \left\{ \left(\frac{\partial^2 V}{\partial Q_{e_\theta}^2} \right)_0 + \left(\frac{\partial^2 V}{\partial Q_{e_\epsilon}^2} \right)_0 \right\} \right| E_\epsilon \right\rangle \frac{1}{\sqrt{2}} (Q_{e_\theta}^2 + Q_{e_\epsilon}^2) \\
 &= \frac{1}{2} \left\{ \frac{1}{2} \left\langle E_\epsilon \left| \left(\frac{\partial^2 V}{\partial Q_{e_\theta}^2} \right)_0 + \left(\frac{\partial^2 V}{\partial Q_{e_\epsilon}^2} \right)_0 \right| E_\epsilon \right\rangle \right\} (Q_{e_\theta}^2 + Q_{e_\epsilon}^2)
 \end{aligned}$$

$$\begin{aligned}
 &= \frac{1}{2} \left\{ \frac{1}{2} \bar{K}_E V \begin{pmatrix} E & E & a_1 \\ \epsilon & \epsilon & \iota \end{pmatrix} \right\} (Q_{e_\theta}^2 + Q_{e_\epsilon}^2) \\
 &= \frac{1}{2} \left(\frac{1}{2\sqrt{2}} \bar{K}_E \right) (Q_{e_\theta}^2 + Q_{e_\epsilon}^2) = \frac{1}{2} K_E (Q_{e_\theta}^2 + Q_{e_\epsilon}^2)
 \end{aligned} \tag{A 11}$$

and

$$\begin{aligned}
 K_{33} = \kappa_{A_1} &= \frac{1}{2} \left\langle A_{1\iota} \left| \left\{ \left(\frac{\partial^2 V}{\partial Q_e \partial Q_e} \right)_0 \right\}_{a_1\iota} \right| A_{1\iota} \right\rangle \{Q_e \otimes Q_e\}_{a_1\iota} \\
 &= \frac{1}{2} \left\langle A_{1\iota} \left| \frac{1}{\sqrt{2}} \left\{ \left(\frac{\partial^2 V}{\partial Q_{e_\theta}^2} \right)_0 + \left(\frac{\partial^2 V}{\partial Q_{e_\epsilon}^2} \right)_0 \right\} \right| A_{1\iota} \right\rangle \frac{1}{\sqrt{2}} (Q_{e_\theta}^2 + Q_{e_\epsilon}^2) \\
 &= \frac{1}{2} \left\{ \frac{1}{2} \left\langle A_{1\iota} \left| \left(\frac{\partial^2 V}{\partial Q_{e_\theta}^2} \right)_0 + \left(\frac{\partial^2 V}{\partial Q_{e_\epsilon}^2} \right)_0 \right| A_{1\iota} \right\rangle \right\} (Q_{e_\theta}^2 + Q_{e_\epsilon}^2) \\
 &= \frac{1}{2} \left\{ \frac{1}{2} \bar{K}_{A_1} V \begin{pmatrix} A_1 & A_1 & a_1 \\ \iota & \iota & \iota \end{pmatrix} \right\} (Q_{e_\theta}^2 + Q_{e_\epsilon}^2) \\
 &= \frac{1}{2} \left(\frac{1}{2} \bar{K}_{A_1} \right) (Q_{e_\theta}^2 + Q_{e_\epsilon}^2) = \frac{1}{2} K_{A_1} (Q_{e_\theta}^2 + Q_{e_\epsilon}^2),
 \end{aligned} \tag{A 12}$$

where K_E and K_{A_1} are the primary force constants for the E and A_1 states (respectively) along the JT-active displacements, with κ_E and κ_{A_1} defining the corresponding harmonic potentials. By considering all the above matrix elements together, as defined in equation (A 4), the final $(E + A_1) \otimes e$ vibronic Hamiltonian assumes the form

$$\mathbf{H}_e = \begin{pmatrix} \mathcal{E}_1 - F_E Q_{e_\theta} - G_E (Q_{e_\epsilon}^2 - Q_{e_\theta}^2) + \kappa_E & F_E Q_{e_\epsilon} + 2G_E Q_{e_\epsilon} Q_{e_\theta} & H_{E/A_1} Q_{e_\theta} \\ F_E Q_{e_\theta} + 2G_E Q_{e_\epsilon} Q_{e_\theta} & \mathcal{E}_2 + F_E Q_{e_\theta} + G_E (Q_{e_\epsilon}^2 - Q_{e_\theta}^2) + \kappa_E & H_{E/A_1} Q_{e_\epsilon} \\ H_{E/A_1} Q_{e_\theta} & H_{E/A_1} Q_{e_\epsilon} & \mathcal{E}_3 + \kappa_{A_1} \end{pmatrix}. \tag{A 13}$$

If the appropriate symmetry correlations are employed and the zero of energy is taken as the E term at the reference configuration (so that $\Delta = \mathcal{E}_3 - \mathcal{E}_2$), equation (2.9) is obtained.

References

1. Weltner W, van Zee RJ. 1989 Carbon molecules, ions, and clusters. *Chem. Rev.* **89**, 1713–1747. ([doi:10.1021/cr00098a005](https://doi.org/10.1021/cr00098a005))
2. van Orden A, Saykally RJ. 1998 Small carbon clusters: spectroscopy, structure, and energetics. *Chem. Rev.* **98**, 2313–2358. ([doi:10.1021/cr970086n](https://doi.org/10.1021/cr970086n))
3. Huggins W. 1881 Preliminary note on the photographic spectrum of Comet b 1881. *Proc. R. Soc. Lond.* **33**, 1–3. ([doi:10.1098/rspa.1881.0060](https://doi.org/10.1098/rspa.1881.0060))
4. Hinkle KW, Keady JJ, Bernath PF. 1988 Detection of C₃ in the circumstellar shell of IRC+10216. *Science* **241**, 1319–1322. ([doi:10.1126/science.241.4871.1319](https://doi.org/10.1126/science.241.4871.1319))
5. Bernath PF, Hinkle KW, Keady JJ. 1989 Detection of C₅ in the circumstellar shell of IRC+10216. *Science* **244**, 562–564. ([doi:10.1126/science.244.4904.562](https://doi.org/10.1126/science.244.4904.562))
6. Lara LM, Lin ZY, Rodrigo R, Ip WH. 2011 67P/Churyumov-Gerasimenko activity evolution during its last perihelion before the Rosetta encounter. *Astron. Astrophys.* **525**, A36. ([doi:10.1051/0004-6361/201015515](https://doi.org/10.1051/0004-6361/201015515))
7. Cox NLJ, Patat F. 2014 Dense molecular clouds in the SN 2008 fp host galaxy. *Astron. Astrophys.* **565**, A61–A71. ([doi:10.1051/0004-6361/201219143](https://doi.org/10.1051/0004-6361/201219143))
8. Cernicharo J, Goicoechea JR, Benilan Y. 2002 A new infrared band in interstellar and circumstellar clouds: C₄ or C₄H? *Astrophys. J.* **580**, L157. ([doi:10.1086/345588](https://doi.org/10.1086/345588))

9. Wakelam V, Loison JC, Herbst E, Talbi D, Quan D, Caralp F. 2009 A sensitivity study of the neutral-neutral reactions C + C₃ and C + C₅ in cold dense interstellar clouds. *Astron. Astrophys.* **495**, 513–521. (doi:10.1051/0004-6361:200810967)
10. Sakai N, Yamamoto S. 2013 Warm carbon-chain chemistry. *Chem. Rev.* **113**, 8981–9015. (doi:10.1021/cr4001308)
11. Koinuma H, Horiuchi T, Inomata K, Ha HK, Nakajima K, Chaudhary KA. 1996 Synthesis of carbon clusters and thin films by low temperature plasma chemical vapor deposition under atmospheric pressure. *Pure Appl. Chem.* **68**, 1151–1154. (doi:10.1351/pac199668051151)
12. Su P, Wu J, Gu J, Wu W, Shaik S, Hiberty PC. 2011 Bonding conundrums in the C₂ molecule: a valence bond study. *J. Chem. Theory Comput.* **7**, 121–130. (doi:10.1021/ct100577v)
13. Shaik S, Danovich D, Wu W, Su P, Rzepa HS, Hiberty PC. 2012 Quadruple bonding in C₂ and analogous eight-valence electron species. *Nat. Chem.* **4**, 195–200. (doi:10.1038/nchem.1263)
14. Shaik S, Rzepa HS, Hoffmann R. 2013 One molecule, two atoms, three views, four bonds? *Angew. Chem.* **52**, 3020–3033. (doi:10.1002/anie.201208206)
15. Danovich D, Hiberty PC, Wu W, Rzepa HS, Shaik S. 2014 The nature of the fourth bond in the ground state of C₂: the quadruple bond conundrum. *Chem. Eur. J.* **20**, 6220–6232. (doi:10.1002/chem.201400356)
16. Hermann M, Frenking G. 2016 The chemical bond in C₂. *Chem. Eur. J.* **22**, 4100–4108. (doi:10.1002/chem.201503762)
17. de Sousa DWO, Nascimento MAC. 2016 Is there a quadruple bond in C₂? *J. Chem. Theory Comput.* **12**, 2234–2241. (doi:10.1021/acs.jctc.6b00055)
18. Shaik S, Danovich D, Braida B, Hiberty PC. 2016 The quadruple bonding in C₂ reproduces the properties of the molecule. *Chem. Eur. J.* **22**, 4116–4128. (doi:10.1002/chem.201600011)
19. Shaik S, Danovich D, Hiberty PC. 2017 To hybridize or not to hybridize? This is the dilemma. *Comput. Theor. Chem.* **1116**, 242–249. (doi:10.1016/j.comptc.2017.01.017)
20. Hirsch A. 2010 The era of carbon allotropes. *Nat. Mater.* **9**, 868–871. (doi:10.1038/nmat2885)
21. Kroto HW, Heath JR, O'Brien SC, Curl RF, Smalley RE. 1985 C₆₀: buckminsterfullerene. *Nature* **318**, 162–163. (doi:10.1038/318162a0)
22. Iijima S. 1991 Helical microtubules of graphitic carbon. *Nature* **354**, 56–58. (doi:10.1038/354056a0)
23. Novoselov KS, Geim AK, Morozov SV, Jiang D, Zhang Y, Dubonos SV, Grigorieva IV, Firsov AA. 2004 Electric field effect in atomically thin carbon films. *Science* **306**, 666–669. (doi:10.1126/science.1102896)
24. Diederich F, Kivala M. 2010 All-carbon scaffolds by rational design. *Adv. Mat.* **22**, 803–812. (doi:10.1002/adma.200902623)
25. Ueno Y, Saito S. 2008 Geometries, stabilities, and reactions of carbon clusters: towards a microscopic theory of fullerene formation. *Phys. Rev. B* **77**, 085403–085413. (doi:10.1103/PhysRevB.77.085403)
26. Kosimov DP, Dzhurakhalov AA, Peeters FM. 2008 Theoretical study of the stable states of small carbon clusters C_n (n = 2–10). *Phys. Rev. B* **78**, 235433–235441. (doi:10.1103/PhysRevB.78.235433)
27. Kosimov DP, Dzhurakhalov AA, Peeters FM. 2010 Carbon clusters: from ring structures to nanographene. *Phys. Rev. B* **81**, 195414–195426. (doi:10.1103/PhysRevB.81.195414)
28. Yen TW, Lai SK. 2015 Use of density functional theory method to calculate structures of neutral carbon clusters C_n (3 ≤ n ≤ 24) and study their variability of structural forms. *J. Chem. Phys.* **142**, 084313–084325. (doi:10.1063/1.4908561)
29. Lai SK, Setiyawati I, Yen TW, Tang YH. 2016 Studying lowest energy structures of carbon clusters by bond-order empirical potentials. *Theor. Chem. Acc.* **136**, 20–32. (doi:10.1007/s00214-016-2042-2)
30. Varandas AJC. 2008 Extrapolation to the complete-basis-set limit and the implications of avoided crossings: the X¹Σ_g⁺, B¹Δ_g, and B'¹Σ_g⁺ states of C₂. *J. Chem. Phys.* **129**, 234103–234116. (doi:10.1063/1.3036115)
31. Varandas AJC. 2009 A simple, yet reliable, direct diabatization scheme. The ¹Σ_g⁺ states of C₂. *Chem. Phys. Lett.* **471**, 315–321. (doi:10.1016/j.cplett.2009.02.028)
32. Boggio-Pasqua M, Voronin AI, Halvick P, Rayez JC. 2000 Analytical representations of high level *ab initio* potential energy curves of the C₂ molecule. *J. Mol. Struct.: THEOCHEM* **531**, 159–167. (doi:10.1016/S0166-1280(00)00442-5)

33. Terentyev A, Scholz R, Schreiber M, Seifert G. 2004 Theoretical investigation of excited states of C₃. *J. Chem. Phys.* **121**, 5767–5776. ([doi:10.1063/1.1786291](https://doi.org/10.1063/1.1786291))
34. Ahmed K, Balint-Kurti GG, Western CM. 2004 *Ab initio* calculations and vibrational energy level fits for the lower singlet potential-energy surfaces of C₃. *J. Chem. Phys.* **121**, 10041–10051. ([doi:10.1063/1.1806820](https://doi.org/10.1063/1.1806820))
35. Rocha CMR, Varandas AJC. 2015 Accurate *ab initio*-based double many-body expansion potential energy surface for the adiabatic ground-state of the C₃ radical including combined Jahn-Teller plus pseudo-Jahn-Teller interactions. *J. Chem. Phys.* **143**, 074302–074318. ([doi:10.1063/1.4928434](https://doi.org/10.1063/1.4928434))
36. Rocha CMR, Varandas AJC. 2016 The Jahn-Teller plus pseudo-Jahn-Teller vibronic problem in the C₃ radical and its topological implications. *J. Chem. Phys.* **144**, 064309–064324. ([doi:10.1063/1.4941382](https://doi.org/10.1063/1.4941382))
37. Parasuk V, Almlöf J. 1991 The electronic and molecular structure of C₄: multireference configuration-interaction calculations. *J. Chem. Phys.* **94**, 8172–8178. ([doi:10.1063/1.460100](https://doi.org/10.1063/1.460100))
38. Massó H, Senent ML, Rosmus P, Hochlaf M. 2006 Electronic structure calculations on the C₄ cluster. *J. Chem. Phys.* **124**, 234304–234311. ([doi:10.1063/1.2187972](https://doi.org/10.1063/1.2187972))
39. Yousaf KE, Taylor PR. 2008 On the electronic structure of small cyclic carbon clusters. *Chem. Phys.* **349**, 58–68. ([doi:10.1016/j.chemphys.2008.02.059](https://doi.org/10.1016/j.chemphys.2008.02.059))
40. Pitzer KS, Clementi E. 1959 Large molecules in carbon vapor. *J. Am. Chem. Soc.* **81**, 4477–4485. ([doi:10.1021/ja01526a010](https://doi.org/10.1021/ja01526a010))
41. Clementi E. 1961 Electronic states in the C₄ molecule. *J. Am. Chem. Soc.* **83**, 4501–4505. ([doi:10.1021/ja01483a002](https://doi.org/10.1021/ja01483a002))
42. Gingerich KA, Finkbeiner HC, Schmude RW. 1994 Enthalpies of formation of small linear carbon clusters. *J. Am. Chem. Soc.* **116**, 3884–3888. ([doi:10.1021/ja00088a025](https://doi.org/10.1021/ja00088a025))
43. Sasaki K, Wakasaki T, Matsui S, Kadota K. 2002 Distributions of C₂ and C₃ radical densities in laser-ablation carbon plumes measured by laser-induced fluorescence imaging spectroscopy. *J. Appl. Phys.* **91**, 4033–4039. ([doi:10.1063/1.1455151](https://doi.org/10.1063/1.1455151))
44. Belau L, Wheeler SE, Ticknor BW, Ahmed M, Leone SR, Allen WD, Schaefer HF, Duncan MA. 2007 Ionization thresholds of small carbon clusters: tunable VUV experiments and theory. *J. Am. Chem. Soc.* **129**, 10229–10243. ([doi:10.1021/ja072526q](https://doi.org/10.1021/ja072526q))
45. Rodríguez-Fortea A, Irle S, Poblet JM. 2011 Fullerenes: formation, stability, and reactivity. *WIREs Comput. Mol. Sci.* **1**, 350–367. ([doi:10.1002/wcms.21](https://doi.org/10.1002/wcms.21))
46. Wollaston WH. 1802 A method of examining refractive and dispersive powers, by prismatic reflection. *Phil. Trans. R. Soc. A* **92**, 365–380. ([doi:10.1098/rstl.1802.0014](https://doi.org/10.1098/rstl.1802.0014))
47. Swan W. 1857 XXIX. On the prismatic spectra of the flames of compounds of carbon and hydrogen. *Trans. R. Soc. Edinburgh* **21**, 411–429. ([doi:10.1017/S0080456800032233](https://doi.org/10.1017/S0080456800032233))
48. Furtenbacher T, Szabó I, Császár AG, Bernath PF, Yurchenko SN, Tennyson J. 2016 Experimental energy levels and partition function of the ¹²C₂ molecule. *Astrophys. J. Suppl. Ser.* **224**, 44–58. ([doi:10.3847/0067-0049/224/2/44](https://doi.org/10.3847/0067-0049/224/2/44))
49. Swings P. 1943 Cometary spectra (council report on the progress at astronomy). *Mon. Not. R. Astron. Soc.* **103**, 86–110. ([doi:10.1093/mnras/103.2.86](https://doi.org/10.1093/mnras/103.2.86))
50. Ballik EA, Ramsay DA. 1959 Ground state of the C₂ molecule. *J. Chem. Phys.* **31**, 1128–1128. ([doi:10.1063/1.1730515](https://doi.org/10.1063/1.1730515))
51. Martin M. 1992 C₂ spectroscopy and kinetics. *J. Photochem. Photobiol. A* **66**, 263–289. ([doi:10.1016/1010-6030\(92\)80001-C](https://doi.org/10.1016/1010-6030(92)80001-C))
52. Mulliken RS. 1939 Note on electronic states of diatomic carbon, and the carbon-carbon bond. *Phys. Rev.* **56**, 778–781. ([doi:10.1103/PhysRev.56.778](https://doi.org/10.1103/PhysRev.56.778))
53. Araki G, Watari W. 1951 Electronic states of C₂-molecule, II: effect of 2s-shells. *Progr. Theor. Phys.* **6**, 945–960. ([doi:10.1143/ptp/6.6.945](https://doi.org/10.1143/ptp/6.6.945))
54. Clementi E, Pitzer KS. 1960 Low excited states in C₂. *J. Chem. Phys.* **32**, 656–662. ([doi:10.1063/1.1730776](https://doi.org/10.1063/1.1730776))
55. Read SM, Vanderslice JT. 1962 Potential energy curves for C₂. *J. Chem. Phys.* **36**, 2366–2369. ([doi:10.1063/1.1732890](https://doi.org/10.1063/1.1732890))
56. Fraga S, Ransil BJ. 1962 Studies in molecular structure. VII. Limited configuration interaction for selected first-row diatomics. *J. Chem. Phys.* **36**, 1127–1142. ([doi:10.1063/1.1732704](https://doi.org/10.1063/1.1732704))
57. Fougere PF, Nesbet RK. 1966 Electronic structure of C₂. *J. Chem. Phys.* **44**, 285–298. ([doi:10.1063/1.1726460](https://doi.org/10.1063/1.1726460))

58. Kirby K, Liu B. 1979 The valence states of C₂: a configuration interaction study. *J. Chem. Phys.* **70**, 893–900. (doi:10.1063/1.437480)
59. Watts JD, Bartlett RJ. 1992 Coupled-cluster calculations on the C₂ molecule and the C₂⁺ and C₂⁻ molecular ions. *J. Chem. Phys.* **96**, 6073–6084. (doi:10.1063/1.462649)
60. Dunning TH. 1989 Gaussian basis sets for use in correlated molecular calculations. I. The atoms boron through neon and hydrogen. *J. Chem. Phys.* **90**, 1007–1023. (doi:10.1063/1.456153)
61. Kendall RA, Dunning TH, Harrison RJ. 1992 Electron affinities of the first-row atoms revisited. Systematic basis sets and wave functions. *J. Chem. Phys.* **96**, 6796–6806. (doi:10.1063/1.462569)
62. Bauschlicher CW, Langhoff SR. 1987 *Ab initio* calculations on C₂, Si₂, and SiC. *J. Chem. Phys.* **87**, 2919–2924. (doi:10.1063/1.453080)
63. Pradhan AD, Partridge H, Bauschlicher CW. 1994 The dissociation energy of CN and C₂. *J. Chem. Phys.* **101**, 3857–3861. (doi:10.1063/1.467503)
64. Peterson KA. 1995 Accurate multireference configuration interaction calculations on the lowest 1Σ⁺ and 3Π electronic states of C₂, CN⁺, BN, and BO⁺. *J. Chem. Phys.* **102**, 262–277. (doi:10.1063/1.469399)
65. Bruna PJ, Grein F. 2001 Spectroscopy of the C₂ molecule: valence and Rydberg states in the 7–10 eV region. An *ab initio* study. *Can. J. Phys.* **79**, 653–671. (doi:10.1139/p01-019)
66. M"ller T, Dallos M, Lischka H, Dubrovay Z, Szalay PG. 2001 A systematic theoretical investigation of the valence excited states of the diatomic molecules B₂, C₂, N₂ and O₂. *Theor. Chem. Acc.* **105**, 227–243. (doi:10.1007/s002140000210)
67. Schmidt TW, Bacsikay GB. 2007 Oscillator strengths of the Mulliken, Swan, Ballik-Ramsay, Phillips, and d³Π_g-c³Σ_u⁺ systems of C₂ calculated by MRCI methods utilizing a biorthogonal transformation of CASSCF orbitals. *J. Chem. Phys.* **127**, 234310–234313. (doi:10.1063/1.2806988)
68. Schmidt TW, Bacsikay GB. 2011 The 1⁵Π_g state of C₂. *J. Chem. Phys.* **134**, 224311–224314. (doi:10.1063/1.3599933)
69. Krechkivska O, Bacsikay GB, Troy TP, Nauta K, Kreuscher TD, Kable SH, Schmidt TW. 2015 Resonance-enhanced 2-photon ionization scheme for C₂ through a newly identified band system: 4³Π_g-a³Π_u. *J. Phys. Chem. A* **119**, 12102–12108. (doi:10.1021/acs.jpca.5b05685)
70. Krechkivska O, Bacsikay GB, Welsh BA, Nauta K, Kable SH, Stanton JF, Schmidt TW. 2016 The ionization energy of C₂. *J. Chem. Phys.* **144**, 144305–144310. (doi:10.1063/1.4944932)
71. Krechkivska O, Welsh BA, Bacsikay GB, Nauta K, Kable SH, Schmidt TW. 2017 First observation of the 3³Π_g state of C₂: Born-Oppenheimer breakdown. *J. Chem. Phys.* **146**, 134306–134313. (doi:10.1063/1.4979293)
72. Abrams ML, Sherrill CD. 2004 Full configuration interaction potential energy curves for the X¹Σ_g⁺, B¹Δ_g, and B'¹Σ_g⁺ states of C₂: a challenge for approximate methods. *J. Chem. Phys.* **121**, 9211–9219. (doi:10.1063/1.1804498)
73. Sherrill CD, Piecuch P. 2005 The X¹Σ_g⁺, B¹Δ_g, and B'¹Σ_g⁺ states of C₂: a comparison of renormalized coupled-cluster and multireference methods with full configuration interaction benchmarks. *J. Chem. Phys.* **122**, 124104–124120. (doi:10.1063/1.1867379)
74. Booth GH, Cleland D, Thom AJW, Alavi A. 2011 Breaking the carbon dimer: the challenges of multiple bond dissociation with full configuration interaction quantum Monte Carlo methods. *J. Chem. Phys.* **135**, 084104–084117. (doi:10.1063/1.3624383)
75. Roskop LB, Kong L, Valeev EF, Gordon MS, Windus TL. 2014 Assessment of perturbative explicitly correlated methods for prototypes of multiconfiguration electronic structure. *J. Chem. Theory Comput.* **10**, 90–101. (doi:10.1021/ct4006773)
76. Schleyer PvR, Maslak P, Chandrasekhar J, Grev RS. 1993 Is a C–C quadruple bond possible? *Tetrahedron Lett.* **34**, 6387–6390. (doi:10.1016/0040-4039(93)85052-X)
77. Herzberg G. 1942 Laboratory production of the λ 4050 group occurring in cometary spectra; future evidence for the presence of CH₂ molecules in comets. *Astrophys. J.* **96**, 314–315. (doi:10.1086/144464)
78. Douglas AE. 1951 Laboratory studies of the λ 4050 group of cometary spectra. *Astrophys. J.* **114**, 446–449. (doi:10.1086/145486)
79. Gausset L, Herzberg G, Lagerqvist A, Rosen B. 1963 Spectrum of the C₃ molecule. *Discuss. Faraday Soc.* **35**, 113–117. (doi:10.1039/DF9633500113)

80. Gausset L, Herzberg G, Lagerqvist A, Rosen B. 1965 Analysis of the 4050-Å group of the C₃ molecule. *Astrophys. J.* **142**, 45–82. ([doi:10.1086/148262](https://doi.org/10.1086/148262))
81. Rohlfing EA, Goldsmith JEM. 1990 Stimulated-emission pumping spectroscopy of jet-cooled C₃: antisymmetric stretch-bend levels. *J. Opt. Soc. Am. B* **7**, 1915–1923. ([doi:10.1364/JOSAB.7.001915](https://doi.org/10.1364/JOSAB.7.001915))
82. Northrup FJ, Sears TJ. 1990 Stimulated-emission pumping spectroscopy study of jet-cooled C₃: pure bending levels and bend-symmetric-stretch combination levels of $\tilde{X}^1\Sigma_g^+$. *J. Opt. Soc. Am. B* **7**, 1924–1934. ([doi:10.1364/JOSAB.7.001924](https://doi.org/10.1364/JOSAB.7.001924))
83. Chen CW, Merer AJ, Chao JM, Hsu YC. 2010 Laser excitation spectrum of C₃ in the region 26 000–30 700 cm⁻¹. *J. Mol. Spectrosc.* **263**, 56–70. ([doi:10.1016/j.jms.2010.06.010](https://doi.org/10.1016/j.jms.2010.06.010))
84. Krieg J *et al.* 2013 High-resolution spectroscopy of C₃ around 3 μm. *J. Phys. Chem. A* **117**, 3332–3339. ([doi:10.1021/jp3119204](https://doi.org/10.1021/jp3119204))
85. Breier AA, Büchling T, Schnierer R, Lutter V, Fuchs GW, Yamada KMT, Mookerjea B, Stutzki J, Giesen TF. 2016 Lowest bending mode of ¹³C-substituted C₃ and an experimentally derived structure. *J. Chem. Phys.* **145**, 234 302–234 311. ([doi:10.1063/1.4971854](https://doi.org/10.1063/1.4971854))
86. Weltner W, McLeod D. 1964 Spectroscopy of carbon vapor condensed in rare-gas matrices at 4 and 20 K. II. *J. Chem. Phys.* **40**, 1305–1316. ([doi:10.1063/1.1725313](https://doi.org/10.1063/1.1725313))
87. Sasada H, Amano T, Jarman C, Bernath PF. 1991 A new triplet band system of C₃: the $\tilde{b}^3\Pi_g$ – $\tilde{b}^3\Pi_u$ transition. *J. Chem. Phys.* **94**, 2401–2407. ([doi:10.1063/1.460710](https://doi.org/10.1063/1.460710))
88. Sych Y, Bornhauser P, Knopp G, Liu Y, Gerber T, Marquardt R, Radi PP. 2013 Perturbation facilitated two-color four-wave-mixing spectroscopy of C₃. *J. Chem. Phys.* **139**, 154 203–154 209. ([doi:10.1063/1.4825198](https://doi.org/10.1063/1.4825198))
89. Rohlfing EA. 1995 Spectroscopic studies of large-amplitude motion in small clusters. In *Spectroscopy and structure* (ed. MA Duncan). Advances in metal and semiconductor clusters: spectroscopy and structure, vol. 3, ch. 2, pp. 85–111. Greenwich, CT: Jai Press Inc.
90. Oka T, Thorburn JA, McCall BJ, Friedman SD, Hobbs LM, Sonnentrucker P, Welty DE, York DG. 2003 Observations of C₃ in translucent sight lines. *Astrophys. J.* **582**, 823–829. ([doi:10.1086/344726](https://doi.org/10.1086/344726))
91. Ádámkovics M, Blake GA, McCall BJ. 2003 Observations of rotationally resolved C₃ in translucent sight lines. *Astrophys. J.* **595**, 235–246. ([doi:10.1086/377305](https://doi.org/10.1086/377305))
92. Cernicharo J, Goicoechea JR, Caux E. 2000 Far-infrared detection of C₃ in sagittarius B2 and IRC+10216. *Astrophys. J. Lett.* **534**, L199–L202. ([doi:10.1086/312668](https://doi.org/10.1086/312668))
93. Mookerjea B *et al.* 2010 Excitation and abundance of C₃ in star forming cores. *Astron. Astrophys.* **521**, L13–L17. ([doi:10.1051/0004-6361/201015095](https://doi.org/10.1051/0004-6361/201015095))
94. Clegg RES, Lambert DL. 1982 On C₃ molecules in diffuse interstellar clouds. *Mon. Not. R. Astron. Soc.* **201**, 723–733. ([doi:10.1093/mnras/201.3.723](https://doi.org/10.1093/mnras/201.3.723))
95. Maier JP, Lakin NM, Walker GAH, Bohlender DA. 2001 Detection of C₃ in diffuse interstellar clouds. *Astrophys. J.* **553**, 267–273. ([doi:10.1086/320668](https://doi.org/10.1086/320668))
96. Roueff E, Felenbok P, Black JH, Gry C. 2002 Interstellar C₃ toward HD 210121. *Astron. Astrophys.* **384**, 629–637. ([doi:10.1051/0004-6361:20020067](https://doi.org/10.1051/0004-6361:20020067))
97. Nemes L, Keszler AM, Parigger CG, Hornkohl JO, Michelsen HA, Stakhursky V. 2007 Spontaneous emission from the C₃ radical in carbon plasma. *Appl. Opt.* **46**, 4032–4040. ([doi:10.1364/AO.46.004032](https://doi.org/10.1364/AO.46.004032))
98. Lopez-Quintas I, Oujja M, Sanz M, Martín M, Ganeev RA, Castillejo M. 2013 Low-order harmonic generation in nanosecond laser ablation plasmas of carbon containing materials. *Appl. Surf. Sci.* **278**, 33–37. ([doi:10.1016/j.apsusc.2012.10.105](https://doi.org/10.1016/j.apsusc.2012.10.105))
99. Clementi E, McLean AD. 1962 SCF-LCAO-MO wave function for the $^1\Sigma_g^+$ ground state of C₃. *J. Chem. Phys.* **36**, 45–47. ([doi:10.1063/1.1732314](https://doi.org/10.1063/1.1732314))
100. Clementi E, Clementi H. 1962 Electron distributions in small molecules. *J. Chem. Phys.* **36**, 2824–2833. ([doi:10.1063/1.1732385](https://doi.org/10.1063/1.1732385))
101. Hoffmann R. 1966 Extended Hückel theory - V: cumulenes, polyenes, polyacetylenes and C_n. *Tetrahedron* **22**, 521–538. ([doi:10.1016/0040-4020\(66\)80020-0](https://doi.org/10.1016/0040-4020(66)80020-0))
102. Liskow DH, Bender CF, Schaefer HF. 1972 Bending frequency of the C₃ molecule. *J. Chem. Phys.* **56**, 5075–5080. ([doi:10.1063/1.1676990](https://doi.org/10.1063/1.1676990))
103. Perić-Radić J, Römlert J, Peyerimhoff SD, Buenker RJ. 1977 Configuration interaction calculation of the potential curves for the C₃ molecule in its ground and lowest-lying Π_u states. *Chem. Phys. Lett.* **50**, 344–350. ([doi:10.1016/0009-2614\(77\)80197-8](https://doi.org/10.1016/0009-2614(77)80197-8))

104. Römelt J, Peyerimhoff SD, Buenker RJ. 1978 *Ab initio* MRD CI calculations for the electron spectrum of the C₃ radical. *Chem. Phys. Lett.* **58**, 1–7. (doi:10.1016/0009-2614(78)80305-4)
105. Carter S, Mills IM, Murrell JN. 1980 Analytical functions for the ground state potential surfaces of C₃(X, ¹Σ_g⁺) and HCN(X, ¹Σ⁺). *J. Mol. Spectrosc.* **81**, 110–121. (doi:10.1016/0022-2852(80)90332-X)
106. Carter S, Mills IM, Dixon RN. 1984 Potential energy surface intersections for triatomic molecules. *J. Mol. Spectrosc.* **106**, 411–422. (doi:10.1016/0022-2852(84)90171-1)
107. Murrell JN. 1990 The many-body expansion of the potential energy function for elemental clusters. *Int. J. Quantum Chem.* **37**, 95–102. (doi:10.1002/qua.560370108)
108. Kraemer W, Bunker P, Yoshimine M. 1984 A theoretical study of the rotation-vibration energy levels and dipole moment functions of CCN⁺, CNC⁺, and C₃. *J. Mol. Spectrosc.* **107**, 191–207. (doi:10.1016/0022-2852(84)90276-5)
109. Jensen P. 1989 The potential energy surface for the C₃ molecule determined from experimental data. Evidence for a bent equilibrium structure. *Collect. Czech. Chem. Commun.* **54**, 1209–1218. (doi:10.1135/cccc19891209)
110. Jørgensen UG, Almlöf J, Siegbahn PEM. 1989 Complete active space self-consistent field calculations of the vibrational band strengths for C₃. *Astrophys. J.* **343**, 554–561. (doi:10.1086/167729)
111. Jensen P, Rohlfing CM, Almlöf J. 1992 Calculation of the complete-active-space-self-consistent-field potential-energy surface, the dipole moment surfaces, the rotation-vibration energies, and the vibrational transition moments for C₃(X ¹Σ_g⁺). *J. Chem. Phys.* **97**, 3399–3411. (doi:10.1063/1.462976)
112. Xpirko V, Mengel M, Jensen P. 1997 Calculation of rotation-vibration energy levels in ground state C₃ by a Born-Oppenheimer-Type separation of the vibrational motions. *J. Mol. Spectrosc.* **183**, 129–138. (doi:10.1006/jmsp.1996.7257)
113. Mladenović M, Schmatz S, Botschwina P. 1994 Large-scale *ab initio* calculations for C₃. *J. Chem. Phys.* **101**, 5891–5899. (doi:10.1063/1.467305)
114. Saha S, Western CM. 2006 Experimental and *Ab Initio* study of a new d¹δ_g state of the c₃ radical. *J. Chem. Phys.* **125**, 224 307–224 318. (doi:10.1063/1.2399528)
115. Schröder B, Sebald P. 2016 High-level theoretical rovibrational spectroscopy beyond fc-CCSD(T): the C₃ molecule. *J. Chem. Phys.* **144**, 044 307–044 318. (doi:10.1063/1.4940780)
116. Rocha CMR, Varandas AJC. In preparation.
117. Rocha CMR, Varandas AJC. In preparation.
118. Fueno H, Taniguchi Y. 1999 *Ab Initio* molecular orbital study of the isomerization reaction surfaces of C₃ and C₃⁻. *Chem. Phys. Lett.* **312**, 65–70. (doi:10.1016/S0009-2614(99)00861-1)
119. Murrell JN, Carter S, Farantos SC, Huxley P, Varandas AJC. 1984 *Molecular potential energy functions*. Chichester, UK: John Wiley & Sons.
120. Varandas AJC, Murrell JN. 1977 A many-body expansion of polyatomic potential energy surfaces: application to H_n systems. *Faraday Discuss. Chem. Soc.* **62**, 92–109. (doi:10.1039/DC9776200092)
121. Whiteside RA, Krishnan R, Frisch MJ, Pople JA, Schleyer PVR. 1981 Cyclic C₃ structures. *Chem. Phys. Lett.* **80**, 547–551. (doi:10.1016/0009-2614(81)85075-0)
122. Jensen P. 1988 A new Morse Oscillator-Rigid Bender Internal Dynamics (MORBID) hamiltonian for triatomic molecules. *J. Mol. Spectrosc.* **128**, 478–501. (doi:10.1016/0022-2852(88)90164-6)
123. Varandas AJC. 1984 A double many-body expansion of molecular potential energy functions. *Mol. Phys.* **53**, 1303–1325. (doi:10.1080/00268978400103021)
124. Varandas AJC. 1985 A general approach to the potential energy functions of small polyatomic systems: molecules and van der Waals molecules. *J. Mol. Struct.: THEOCHEM* **120**, 401–424. (doi:10.1016/0166-1280(85)85134-4)
125. Varandas AJC. 1988 Intermolecular and intramolecular potentials: topographical aspects, calculation, and functional representation via a double many-body expansion method. *Adv. Chem. Phys.* **74**, 255–338. (doi:10.1002/9780470141236.ch2)
126. Varandas AJC. 1989 A semiempirical method for correcting configuration interaction potential energy surfaces. *J. Chem. Phys.* **90**, 4379–4391. (doi:10.1063/1.456624)
127. Galvão BRL, Mota VC, Varandas AJC. 2015 Modeling cusps in adiabatic potential energy surfaces. *J. Phys. Chem. A* **119**, 1415–1421. (doi:10.1021/jp512671q)

128. Galvão BRL, Mota VC, Varandas AJC. 2016 Modeling cusps in adiabatic potential energy surfaces using a generalized Jahn-Teller coordinate. *Chem. Phys. Lett.* **660**, 55–59. (doi:10.1016/j.cplett.2016.07.029)
129. Whiteside RA, Krishnan R, Defrees DJ, Pople JA, Schleyer PR. 1981 Structures of C₄. *Chem. Phys. Lett.* **78**, 538–540. (doi:10.1016/0009-2614(81)85253-0)
130. Magers DH, Harrison RJ, Bartlett RJ. 1986 Isomers and excitation energies of C₄. *J. Chem. Phys.* **84**, 3284–3290. (doi:10.1063/1.450259)
131. Ritchie JP, King HF, Young WS. 1986 Structures and energies for C₄. *J. Chem. Phys.* **85**, 5175–5182. (doi:10.1063/1.451711)
132. Pacchioni G, Koutecký J. 1988 *Ab Initio* MRD CI investigation of the optical spectra of C₄ and C₅ clusters. *J. Chem. Phys.* **88**, 1066–1073. (doi:10.1063/1.454276)
133. Bernholdt DE, Magers DH, Bartlett RJ. 1988 Stability and properties of C₄ isomers. *J. Chem. Phys.* **89**, 3612–3617. (doi:10.1063/1.454881)
134. Lammertsma K, Güner OF, Sudhakar PV. 1991 Rhombic C₄. Does it contain the shortest nonbonding C–C distance? *J. Chem. Phys.* **94**, 8105–8111. (doi:10.1063/1.460093)
135. Martin JML, François JP, Gijbels R. 1991 A critical comparison of MNDO/3, MNDO, AM1, and PM3 for a model problem: carbon clusters C₂–C₁₀. An *ad hoc* reparametrization of MNDO well suited for the accurate prediction of their spectroscopic constants. *J. Comput. Chem.* **12**, 52–70. (doi:10.1002/jcc.540120107)
136. Martin JML, François JP, Gijbels R. 1991 *Ab Initio* study of the structure, infrared spectra, and heat of formation of C₄. *J. Chem. Phys.* **94**, 3753–3761. (doi:10.1063/1.459747)
137. Watts JD, Gauss J, Stanton JF, Bartlett RJ. 1992 Linear and cyclic isomers of C₄. A theoretical study with coupled-cluster methods and large basis sets. *J. Chem. Phys.* **97**, 8372–8381. (doi:10.1063/1.463407)
138. Blanksby SJ, Schröder D, Dua S, Bowie JH, Schwarz H. 2000 Conversion of linear to rhombic C₄ in the gas phase: a joint experimental and theoretical study. *J. Am. Chem. Soc.* **122**, 7105–7113. (doi:10.1021/ja000951c)
139. Wang T, Buntine MA, Bowie JH. 2009 Study of the isomers of isoelectronic C₄, (C₃B)–, and (C₃N)+: rearrangements through cyclic isomers. *J. Phys. Chem. A* **113**, 12 952–12 960. (doi:10.1021/jp907484z)
140. Senent ML, Massó H, Hochlaf M. 2007 Anharmonic spectroscopic study of the ground electronic state of various C₄ radical isotopomers. *Astrophys. J.* **670**, 1510–1517. (doi:10.1086/522485)
141. Wang X, Huang X, Bowman JM, Lee TJ. 2013 Anharmonic rovibrational calculations of singlet cyclic C₄ using a new *Ab Initio* potential and a quartic force field. *J. Chem. Phys.* **139**, 224 302–224 308. (doi:10.1063/1.4837177)
142. Maier JP, Walker GAH, Bohlender DA. 2002 Limits to interstellar C₄ and C₅ toward ξ Ophiuchi. *Astrophys. J.* **566**, 332–335. (doi:10.1086/337965)
143. Jungen M, Xu R. 2003 The absorption spectrum of C₄. *Z. Phys. Chem.* **217**, 105–114. (doi:10.1524/zpch.217.2.105.22612)
144. Weltner W, Thompson KR, DeKock RL. 1971 Spectroscopy of carbon molecules. IV. C₄, C₅, C₆ (and C₉). *J. Am. Chem. Soc.* **93**, 4688–4695. (doi:10.1021/ja00748a007)
145. Graham WRM, Dismuke KI, Weltner JW. 1976 The C₄ molecule. *Astrophys. J.* **204**, 301–310. (doi:10.1086/154172)
146. Heath JR, Saykally RJ. 1991 The structure of the C₄ cluster radical. *J. Chem. Phys.* **94**, 3271–3273. (doi:10.1063/1.459797)
147. Moazzen-Ahmadi N, Thong JJ, McKellar ARW. 1994 Infrared diode laser spectroscopy of the v₃ fundamental and v₃ + v₅ – v₅ sequence bands of the C₄ radical in a hollow cathode discharge. *J. Chem. Phys.* **100**, 4033–4038. (doi:10.1063/1.466340)
148. Xu C, Burton GR, Taylor TR, Neumark DM. 1997 Photoelectron spectroscopy of C₄[–], C₆[–], and C₈[–]. *J. Chem. Phys.* **107**, 3428–3436. (doi:10.1063/1.474715)
149. Gakwaya S, Abusara Z, Moazzen-Ahmadi N. 2004 Vibrational hot bands of linear C₄ and C₅ arising from a bending vibration with two quanta in the lowest bend: the (v₃+2v₅)-2v₅ band of C₄ and the (v₃+2v₇)-2v₇ band of C₅. *Chem. Phys. Lett.* **398**, 564–571. (doi:10.1016/j.cplett.2004.09.130)
150. Algranati M, Feldman H, Kella D, Malkin E, Miklazky E, Naaman R, Vager Z, Zajfman J. 1989 The structure of C₄ as studied by the Coulomb explosion method. *J. Chem. Phys.* **90**, 4617–4618. (doi:10.1063/1.456597)

151. Vager Z, Feldman H, Kella D, Malkin E, Miklazky E, Zajfman J, Naaman R. 1991 The structure of small carbon clusters. *Z. Phys. D* **19**, 413–418. ([doi:10.1007/BF01448341](https://doi.org/10.1007/BF01448341))
152. Kella D, Zajfman D, Heber O, Majer D, Feldman H, Vager Z, Naaman R. 1993 Observation of laser excitation of rhombic C₄ using the coulomb explosion method. *Z. Phys. D* **26**, 340–342. ([doi:10.1007/BF01429188](https://doi.org/10.1007/BF01429188))
153. Slanina Z, Zahradník R. 1977 Calculations of absolute values of equilibrium and rate constants. 9. MINDO/2 Study of equilibrium carbon vapor. *J. Phys. Chem.* **81**, 2252–2257. ([doi:10.1021/j100539a011](https://doi.org/10.1021/j100539a011))
154. Cheung HM, Graham WRM. 1989 Electron-spin-resonance characterization of nonlinear C₄ trapped in solid Argon. *J. Chem. Phys.* **91**, 6664–6670. ([doi:10.1063/1.457385](https://doi.org/10.1063/1.457385))
155. Martin JML, Schwenke DW, Lee TJ, Taylor PR. 1996 Is there evidence for detection of cyclic C₄ in IR spectra? an accurate *Ab Initio* computed quartic force field. *J. Chem. Phys.* **104**, 4657–4663. ([doi:10.1063/1.471212](https://doi.org/10.1063/1.471212))
156. Wigner E, Witmer EE. 1928 Über Die Struktur Der Zweiatomigen Molekelspektren Nach Der Quantenmechanik. *Z. Phys.* **51**, 859–886. ([doi:10.1007/BF01400247](https://doi.org/10.1007/BF01400247))
157. Herzberg G. 1966 *Molecular spectra and molecular structure III. Electronic spectra and electronic structure of polyatomic molecules*, vol. III. New York, NY: Van Nostrand.
158. Bersuker IB. 2006 *The Jahn-Teller effect*. Cambridge, UK: Cambridge University Press.
159. Zwanziger JW, Grant ER. 1987 Topological phase in molecular bound states: application to the E ⊗ e system. *J. Chem. Phys.* **87**, 2954–2964. ([doi:10.1063/1.453083](https://doi.org/10.1063/1.453083))
160. Bersuker IB. 2013 Pseudo-Jahn-Teller effect—a two-state paradigm in formation, deformation, and transformation of molecular systems and solids. *Chem. Rev.* **113**, 1351–1390. ([doi:10.1021/cr300279n](https://doi.org/10.1021/cr300279n))
161. Griffith JS. 1962 *The irreducible tensor method for molecular symmetry groups*. New Jersey, NJ: Prentice-Hall.
162. Garcia-Fernandez P, Bersuker IB, Boggs JE. 2006 Orbital disproportionation and spin crossover as a pseudo Jahn-Teller effect. *J. Chem. Phys.* **125**, 104102–104112. ([doi:10.1063/1.2346682](https://doi.org/10.1063/1.2346682))
163. Dillon JJ, Yarkony DR. 2007 Seams near seams: the Jahn-Teller effect in the ¹E'' State of N₃⁺. *J. Chem. Phys.* **126**, 124113–124119. ([doi:10.1063/1.2710255](https://doi.org/10.1063/1.2710255))
164. Longuet-Higgins HC. 1975 The intersection of potential energy surfaces in polyatomic molecules. *Proc. R. Soc. Lond. A* **344**, 147–156. ([doi:10.1098/rspa.1975.0095](https://doi.org/10.1098/rspa.1975.0095))
165. Herzberg G, Longuet-Higgins HC. 1963 Intersection of potential energy surfaces in polyatomic molecules. *Discuss. Faraday Soc.* **35**, 77–82. ([doi:10.1039/DF9633500077](https://doi.org/10.1039/DF9633500077))
166. Berry MV. 1984 Quantal phase factors accompanying adiabatic changes. *Proc. R. Soc. Lond. A* **392**, 45–57. ([doi:10.1098/rspa.1984.0023](https://doi.org/10.1098/rspa.1984.0023))
167. Varandas AJC, Tennyson J, Murrell JN. 1979 Chercher le croisement. *Chem. Phys. Lett.* **61**, 431–434. ([doi:10.1016/0009-2614\(79\)87143-2](https://doi.org/10.1016/0009-2614(79)87143-2))
168. Kramida A, Ralchenko Y, Reader J, Team NA. 2015 *NIST atomic spectra database*. Gaithersburg, MD: National Institute of Standards and Technology. <http://physics.nist.gov/asd>.
169. Varandas AJC, Murrell JN. 1981 Choosing points in potential energy surfaces for fitting polynomial functions: application of permutational symmetry. *Chem. Phys. Lett.* **84**, 440–445. ([doi:10.1016/0009-2614\(81\)80381-8](https://doi.org/10.1016/0009-2614(81)80381-8))
170. Porter RN, Stevens RM, Karplus M. 1968 Symmetric H₃: a semiempirical and *Ab Initio* study of a simple Jahn-Teller system. *J. Chem. Phys.* **49**, 5163–5178. ([doi:10.1063/1.1670017](https://doi.org/10.1063/1.1670017))
171. Varandas AJC. 1987 A useful triangular plot of triatomic potential energy surfaces. *Chem. Phys. Lett.* **138**, 455–461. ([doi:10.1016/0009-2614\(87\)80540-7](https://doi.org/10.1016/0009-2614(87)80540-7))
172. Zhang G, Chen K, Merer AJ, Hsu Y, Chen W, Shaji S, Liao Y. 2005 The 4051-Å Band of C₃ ($\tilde{\Lambda}^1 \Pi_u - \tilde{X}^1 \Sigma_g^+$, 000-000): perturbed low-J lines and lifetime measurements. *J. Chem. Phys.* **122**, 244308–244315. ([doi:10.1063/1.1928827](https://doi.org/10.1063/1.1928827))
173. Varandas AJC. 2003 A realistic multi-sheeted potential energy surface for NO₂(²A') from the double many-body expansion method and a novel multiple energy-switching scheme. *J. Chem. Phys.* **119**, 2596–2613. ([doi:10.1063/1.1586911](https://doi.org/10.1063/1.1586911))
174. Werner HJ *et al.* 2010 MOLPRO, a package of *ab initio* programs, version 2010.1. See <http://www.molpro.net>, Cardiff, U.K.
175. Szalay PG, Müller T, Gidofalvi G, Lischka H, Shepard R. 2012 Multiconfiguration self-consistent field and multireference configuration interaction methods and applications. *Chem. Rev.* **112**, 108–181. ([doi:10.1021/cr200137a](https://doi.org/10.1021/cr200137a))

176. Varandas AJC. 2012 *Ab Initio* treatment of bond-breaking reactions: accurate course of HO₃ dissociation and revisit to isomerization. *J. Chem. Theory Comput.* **8**, 428–441. (doi:10.1021/ct200773b)
177. Varandas AJC. 2013 Accurate determination of the reaction course in HY₂ ⇌ Y + YH (Y=O,S): detailed analysis of the covalent- to hydrogen-bonding transition. *J. Phys. Chem. A* **117**, 7393–7407. (doi:10.1021/jp401384d)
178. Varandas AJC. 2014 On carbon dioxide capture: an accurate *Ab Initio* study of the Li₃N + CO₂ insertion reaction. *Comput. Theor. Chem.* **1036**, 61–71. (doi:10.1016/j.comptc.2014.02.022)
179. Pansini FNN, Neto AC, Varandas AJC. 2016 Extrapolation of Hartree-Fock and multiconfiguration self-consistent-field energies to the complete basis set limit. *Theo. Chem. Acc.* **135**, 261–267. (doi:10.1007/s00214-016-2016-4)
180. Varandas AJC. 2007 Extrapolating to the one-electron basis-set limit in electronic structure calculations. *J. Chem. Phys.* **126**, 244 105–244 119. (doi:10.1063/1.2741259)
181. Varandas AJC, Pansini FNN. 2014 Narrowing the error in electron correlation calculations by basis set re-hierarchization and use of the unified singlet and triplet electron-pair extrapolation scheme: application to a test set of 106 systems. *J. Chem. Phys.* **141**, 224 113–224 121. (doi:10.1063/1.4903193)
182. Pansini FNN, Neto AC, Varandas AJC. 2015 On the performance of various hierarchized bases in extrapolating the correlation energy to the complete basis set limit. *Chem. Phys. Lett.* **641**, 90–96. (doi:10.1016/j.cplett.2015.10.064)
183. Ngandjong A, Mezei J, Mougenot J, Michau A, Hassouni K, Lombardi G, Seydou M, Maurel F. 2017 Structural stability and growth mechanism of neutral and anionic small carbon clusters: density functional study. *Comp. Theor. Chem.* **1102**, 105–113. (doi:10.1016/j.comptc.2017.01.012)
184. Karton A, Tarnopolsky A, Martin JML. 2009 Atomization energies of the carbon clusters C_n ($n = 2 – 10$) revisited by means of W4 theory as well as density functional, G_n, and CBS methods. *Mol. Phys.* **107**, 977–990. (doi:10.1080/00268970802708959)
185. Murrell JN. 1978 Potential energy surfaces for clusters of main group elements. *Chem. Phys. Lett.* **55**, 1–5. (doi:10.1016/0009-2614(78)85118-5)
186. Varandas AJC, Llanio-Trujillo JL. 2002 On triplet tetraoxygen: *Ab Initio* study along minimum energy path and global modelling. *Chem. Phys. Lett.* **356**, 585–594. (doi:10.1016/S0009-2614(02)00429-3)
187. Ballester MY, Varandas AJC. 2005 Double many-body expansion potential energy surface for ground state HSO₂. *Phys. Chem. Chem. Phys.* **7**, 2305–2317. (doi:10.1039/B500990A)
188. Poveda LA, Biczysko M, Varandas AJC. 2009 Accurate *Ab Initio* based DMBE potential energy surface for the ground electronic state of N₂H₂. *J. Chem. Phys.* **131**, 044309. (doi:10.1063/1.3176512)
189. Martínez-Núñez E, Varandas AJC. 2001 Single-valued DMBE potential energy surface for HSO: a distributed n -body polynomial approach. *J. Phys. Chem. A* **105**, 5923–5932. (doi:10.1021/jp0101460)

Glossary

- ABW: Potential energy surface of Ahmed, Balint-Kurti and Western [34]
- ANO: Atomic natural orbital basis set [37]
- AVXZ: Dunning's type augmented correlation-consistent polarized-valence basis [60,61]
- CASSCF: The complete active space self-consistent field method [175]
- CAS: Simplified notation to imply CASSCF
- CAS(x,y): CASSCF specifying x -active orbitals and y -active electrons
- CASDC: CASSCF energy plus dynamical correlation energy [177]
- c -: Cyclic molecular structure
- CBS: The complete basis set limit [179,180]
- CC: The coupled-cluster method [59,130,133,136,137]
- CCSD: CC with single and double excitations
- CCSD(T): CCSD including triple excitations non-iteratively
- CI: The configuration interaction [56–58,131]

CISD:	CI with single and double excitations
CISD(Q):	CISD including the Davidson correction [175]
Ci:	Conical intersection
CSF:	The configuration state function
<i>d</i> :	Distorted molecular structure
dc:	Dynamical correlation
DFT:	Density functional theory [138,183]
DMBE:	The double many-body expansion method [123–125]
DMBE-SEC:	The DMBE scaled external correlation approach [126]
EHF:	The extended Hartree-Fock energy
ES:	The energy-switching method [173]
fc:	The frozen core approximation
FVCAS:	The full-valence CAS method [175]
GP:	Geometric phase [164–166]
HF:	The Hartree-Fock method [175]
HOMO:	The highest occupied molecular orbital
IR:	Infrared
IRC:	Intrinsic reaction coordinate [176,177]
irrep:	Irreducible representation
JT:	Jahn-Teller [158]
<i>l</i> :	Linear molecular structure
LUMO:	The lowest unoccupied molecular orbital
MBE:	The many-body expansion method [119,120]
MO:	Molecular orbital
MPn:	Møller-Plesset perturbation theory [121,129]
MR:	Multi-reference electronic structure methods
MRCI:	The MR-CI method [175]
MRCI(Q):	The MRCI method including the Davidson correction [175]
ndc:	Non-dynamical correlation
ORC:	Optimized reaction coordinate [176,177]
PEC:	Potential energy curve
PES:	Potential energy surface
PJT:	Pseudo-Jahn-Teller [158]
QFF:	The quartic force field local PES
<i>r</i> :	Rhombic molecular structure
RMSD:	Root mean square deviation
RKR:	The Rydberg–Klein–Rees method [55]
RT:	Renner–Teller [158]
SCF:	The self-consistent field method [175]
SLP:	Small linear parameter
SR:	Single-reference electronic structure methods
SS:	Potential energy surface of Schröder & Sebald [115]
VB:	The valence bond theory [18]
ve:	valence electron approximation
USTE:	The uniform singlet- and triplet-pair extrapolation method [180]
ZPE:	Zero-point energy